

AD-A196 966

NAVAL POSTGRADUATE SCHOOL Monterey, California



THESIS

IONS GENERATED ON OR NEAR
SATELLITE SURFACES

by

Christopher William Norwood
June 1988

Thesis Advisor:

Richard C Olsen

Approved for public release; distribution is unlimited

DTIC
ELECTE
AUG 16 1988
H

REPORT DOCUMENTATION PAGE

1a REPORT SECURITY CLASSIFICATION UNCLASSIFIED			1b RESTRICTIVE MARKINGS		
2a SECURITY CLASSIFICATION AUTHORITY			3 DISTRIBUTION AVAILABILITY OF REPORT Approved for public release; distribution is unlimited		
2b DECLASSIFICATION/DOWNGRADING SCHEDULE					
4 PERFORMING ORGANIZATION REPORT NUMBER(S)			5 MONITORING ORGANIZATION REPORT NUMBER(S)		
6a NAME OF PERFORMING ORGANIZATION Naval Postgraduate School		6b OFFICE SYMBOL (If applicable) Code 61		7a NAME OF MONITORING ORGANIZATION Naval Postgraduate School	
6c ADDRESS (City, State, and ZIP Code) Monterey, California, 93943-5000			7b ADDRESS (City, State, and ZIP Code) Monterey, California, 93943-5000		
8a NAME OF FUNDING SPONSORING ORGANIZATION		8b OFFICE SYMBOL (If applicable)		9 PROCUREMENT INSTRUMENT IDENTIFICATION NUMBER	
8c ADDRESS (City, State, and ZIP Code)			10 SOURCE OF FUNDING NUMBERS		
			PROGRAM ELEMENT NO	PROJECT NO	TASK NO
			WORK UNIT ACCESSION NO		
11 TITLE (Include Security Classification) IONS GENERATED ON OR NEAR SATELLITE SURFACES					
12 PERSONAL AUTHOR(S) Norwood, Christopher W.					
13a TYPE OF REPORT Master's Thesis		13b TIME COVERED FROM TO		14 DATE OF REPORT (Year, Month, Day) 1988, June	
				15 PAGE COUNT 131	
16 SUPPLEMENTARY NOTATION The views expressed in this Thesis are those of the author and do not reflect the official policy or position of the Department of Defense or the U.S. Government					
17 COSATI CODES			18 SUBJECT TERMS (Continue on reverse if necessary and identify by block number)		
FIELD	GROUP	SUB-GROUP	Ions, SCATHA, Sputtering, Ion Emission,		
19 ABSTRACT (Continue on reverse if necessary and identify by block number) Observations of positively charged particles that are generated on or near satellite surfaces have been made on several spacecraft. This thesis postulates sputtering of the satellite surface due to ambient ion impact as the generating mechanism. Calculations are made using the Sigmund-Thompson sputtering theory to determine the response at the satellite particle detectors. These calculations indicate that surface sputtering creates a sufficient flux to account for the observed phenomena. The NASA Charging Analyzer program was run to determine the trajectories for measured particles. The calculated trajectories were determined to lead to the spacecraft surface, again indicating that surface emission was the source. The sputtering flux as calculated was insufficient to cause any significant short-term damage to the spacecraft, beyond thin coating erosion.					
20 DISTRIBUTION/AVAILABILITY OF ABSTRACT <input checked="" type="checkbox"/> UNCLASSIFIED/UNLIMITED <input type="checkbox"/> SAME AS RPT <input type="checkbox"/> DTIC USERS			21 ABSTRACT SECURITY CLASSIFICATION UNCLASSIFIED		
22a NAME OF RESPONSIBLE INDIVIDUAL R.C. Olsen			22b TELEPHONE (Include Area Code) (408) 646-2019		22c OFFICE SYMBOL 610s

Approved for public release; distribution is unlimited

Ions Generated on or Near Satellite Surfaces

by

Christopher W. Norwood
Lieutenant, United States Navy
B.S., Villanova University, 1981

Submitted in partial fulfillment of the
requirements for the degree of

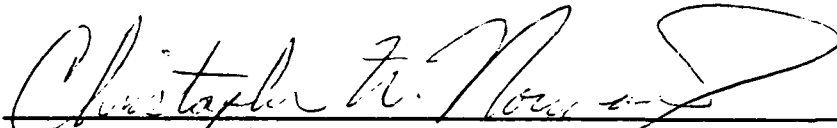
MASTER OF SCIENCE IN PHYSICS

from the

NAVAL POSTGRADUATE SCHOOL

June 1988

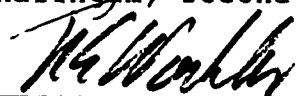
Author:



Christopher W. Norwood

Approved by:


R.C. Olsen, Thesis Advisor


S. Gnanalingam, Second Reader


K.E. Woehler, Chairman,
Department of Physics


Gordon E. Schacher,
Dean of Science and Engineering

ABSTRACT

Observations of positively charged particles that are generated on or near satellite surfaces have been made on several spacecraft. This thesis postulates sputtering of the satellite surface due to ambient ion impact as the generating mechanism. Calculations are made using the Sigmund-Thompson sputtering theory to determine the response at the particle detectors. These calculations indicate that surface sputtering creates a sufficient flux to account for the observed phenomena. The NASA Charging Analyzer Program was run to determine the trajectories for actually observed particles. The calculated trajectories were determined to lead to the spacecraft surface, again indicating that surface emission was the source. The sputtering flux as calculated was insufficient to cause any significant short-term damage to the spacecraft, beyond thin coating erosion.



Accession For		
NTIS GRA&I		<input checked="" type="checkbox"/>
NTIS TAB		<input type="checkbox"/>
Unannounced		<input type="checkbox"/>
Justification		
By		
Publication/		
Availability		
Distribution		
Dist		
A-1		

TABLE OF CONTENTS

I.	INTRODUCTION.....	1
A.	OVERVIEW.....	1
B.	SCATHA SPACECRAFT.....	2
1.	Spacecraft Construction.....	2
2.	Spacecraft Orbit and Environment.....	5
3.	Instruments.....	9
4.	Ion Gun.....	13
C.	OTHER SATELLITES.....	13
1.	ATS-6.....	13
2.	ISEE.....	15
D.	SPACECRAFT CHARGING.....	15
E.	SPUTTERING.....	20
1.	The Sigmund Theory.....	22
2.	The Thompson Theory.....	27
3.	Comparison with Experiment.....	29
4.	Limitations of the Sigmund Theory.....	38
F.	NASA CHARGING ANALYZER PROGRAM.....	39
II.	OBSERVATIONS.....	41
A.	PREVIOUS OBSERVATIONS.....	41

1. ATS-5.....	41
2. ATS-6.....	44
3. ISEE.....	46
B. P78-2 (SCATHA).....	48
1. Day 83 of 1979.....	48
2. Day 86 of 1979.....	53
3. Day 94 of 1979.....	58
4. Day 200 of 1979.....	60
5. Day 92 of 1981.....	63
III. DISCUSSION.....	66
A. POSSIBLE ION SOURCES.....	66
1. Outgassing.....	67
2. Sputtering.....	70
B. CALCULATION OF THE SPUTTERING FLUX.....	81
AT THE DETECTOR	
IV. CONCLUSIONS.....	101
APPENDIX.....	104
LIST OF REFERENCES.....	115
INITIAL DISTRIBUTION LIST.....	119

LIST OF TABLES

1.	Magnetospheric Ions and Their Sources.....	104
2.	Storm Time Ring Current Composition.....	105
3.	Storm Time Magnetosphere Composition.....	106
4.	Values of the Reduced Stopping Power.....	107
5.	Calculated and Measured Sputtering Yields for..... Various Materials	108
6.	Calculated Sputtering Yields using a Modified Binding Energy	109
7.	Ratio of Sputtering Yield per Atom for Molecular... and Atomic Ion Bombardment	110
8.	SCATHA Particle Detector Energy Channels.....	111
9.	The Sputtering Yields of 10 keV Ion Beams on..... Silicon and Silicon Dioxide	113
10.	Ambient Plasma Values for Days 83,86, 200..... of 1979 from the Lockheed Ion Mass Spectrometer	114

LIST OF FIGURES

Figure 1.	SCATHA Satellite.....	4
Figure 2.	SCATHA Orbit.....	6
Figure 3.	Regions of Space near Earth.....	7
Figure 4.	SC-9 Detector Arrangement.....	11
Figure 5.	SC-9 Detector Angular Coverage.....	12
Figure 6.	ATS-6 Satellite.....	14
Figure 7.	Charging Current Schematic.....	16
Figure 8.	Sputtering Yield for Aluminum.....	21
Figure 9.	$\alpha(M_2/M_1)$ vs. M_2/M_1	26
Figure 10.	The Function $E/(E + U_0)^3$	30
Figure 11.	Energy Distribution of Sputtered Gold Atoms..	31
Figure 12.	Calculated And Experimental Sputtering.....	33
	Yields for Copper	
Figure 13.	Mass Dependence of the Sputtering.....	34
	Yield for Various Atoms	
Figure 14.	Typical Sputtering Yields for H ⁺ and O ⁺	35
	on a Silicon Target	
Figure 15.	The Dependence of the Sputtering Yield.....	37
	on Angle of Incidence	
Figure 16.	ATS-5, Spectrogram, Day 274 of 1970.....	42
Figure 17.	ATS-6, Spectrogram, Day 248 of 1974.....	45
Figure 18.	ISEE-1, Mass Spectrometer, March 17, 1978.....	47
Figure 19.	SCATHA, Spectrogram, Day 83 of 1979.....	50
Figure 20.	Day 83 of 1979, Ion Distribution Function....	51
Figure 21.	Day 83 of 1979, Vehicle Potential,.....	52
	Triangle Peak Energy, and Look Angle vs. Time	
Figure 22.	SCATHA, Spectrogram, Day 86 of 1979.....	54
Figure 23.	Day 86 of 1979, Ion Distribution Function....	55

Figure 24. Day 86 of 1979, Vehicle Potential.....	57
Triangle Peak Energy, and Look Angle vs. Time	
Figure 25. SCATHA, Spectrogram, Day 94 of 1979.....	59
Figure 26. SCATHA, Spectrogram, Day 200 of 1979.....	61
Figure 27. Day 200 of 1979, Ion Distribution Functions..	62
Figure 28. SCATHA, Spectrogram, Day 92 of 1981.....	64
Figure 29. Day 92 of 1981, Ion Distribution Function....	65
Figure 30. Detector Beam Viewing Geometry.....	73
Figure 31. Oxygen-Silicon Yield Curves.....	75
Figure 32. Lindhard's Universal Function.....	83
Figure 33. Incident, Emitted, and Ion Fluxes.....	84
Day 86 of 1979	
Figure 34. Channel Responses for a 35 V Differential....	86
Charge, O+ Incident, Day 86, 1979	
Figure 35. Channel Response for a 35 eV Differential....	87
Charge, O+ Incident, Day 200, 1979	
Figure 36. Channel Response for Zero Differential.....	90
Charge	
Figure 37. NASCAP Trajectories, Day 86 of 1979.....	91
Figure 38. NASCAP Trajectory, Day 94, Lo Detector.....	93
Figure 39. NASCAP Trajectory, Day 94, Lo Detector.....	94
Figure 40. NASCAP Trajectory, Day 94, Hi Detector.....	96
Figure 41. NASCAP Trajectory, Day 94, Hi Detector.....	97
Figure 42. NASCAP Trajectory, Day 94, Fix Detector.....	98
Figure 43. NASCAP Trajectory, Day 94, Fix Detector.....	99

I. INTRODUCTION

A. OVERVIEW

Spacecraft charging is the development of a potential difference between a space vehicle and its plasma environment. It is of significance for scientific purposes, since the potential may affect measurement of the ambient properties of the environment, and for practical purposes, since it may lead to anomalous command signals and physical damage to the affected spacecraft. Although predictions of spacecraft charging had been made previously, the first reports of high level spacecraft charging were those for Applications Technology Satellite (ATS) 5 (Ref. 1). Similar events were subsequently noted on ATS-6 and P78-2 (SCATHA) by various observers (Ref.2).

Generally, negative charging events are identified by an intense peak in the measured ion spectra at a specific energy, with an absence of ions of lesser energies. This intense peak is most clearly seen on the plot of the distribution function versus energy, as will be displayed later in this work. This peak is known as the charging peak. Such observations result from the acceleration of the ambient plasma ions into the detector by the potential drop between the plasma and the spacecraft. Occasionally, ion fluxes are seen at energies below the peak energy, which

would appear to violate conservation of energy for a collisionless plasma. These ion distributions have been reported previously, and tentatively ascribed to sputtering from spacecraft surfaces (Ref. 3). They have been termed "spacecraft generated ions" (Ref. 2).

Analysis of this particular phenomenon is of practical interest, as these ions may contaminate the charging peak, leading to an underestimation of the satellite potential. The contamination of the charging peak may be particularly important active experiments in low earth orbit, such as SPACELAB. Additionally, since we believe the source to be sputtering, the flux of these particles is an indication of the damage to the satellite surface caused by the vehicle's environment. Also, the life expectancy of precision satellite surfaces, e.g. optical surfaces, and surface coatings may be directly affected by the sputtering rate appropriate to their environment.

B. SCATHA SPACECRAFT

Most of the experimental data and calculations performed in this thesis are based on the P78-2 (SCATHA) spacecraft. The construction, environment, and sensors of this vehicle will be discussed in the next several sections.

1. Spacecraft Construction

The U.S. Air Force P78-2 spacecraft was launched in January 1979 to collect data for a study of Spacecraft Charging AT High Altitudes (SCATHA), in a joint

NASA/Department of Defense Program. The satellite body was cylindrical in shape with a length and diameter of approximately 1.75 meters. Seven booms were deployed in orbit from the spacecraft to provide isolation for experiments from charging effects on the satellite surface. Figure 1 depicts the SCATHA spacecraft. The top of the satellite in the figure is the forward end, and the bottom is aft. The experiments and communications equipment for the satellite are primarily located on equipment decks in the center of the cylinder. The University of California, San Diego, charged particle detector was on the forward end, and the ion gun was on the aft end; both are described below. The outer cylinder surface was divided into three general areas; two solar arrays, one forward and one aft, and a bellyband between them to provide access panels. Additionally, sections of the surface were covered in various materials, such as kevlar and mylar, for use in the experiments. {Ref. 4}

The spacecraft was constructed of special lightweight materials, as its orbit was at the maximum capability of the launch vehicle. The central tube of the spacecraft was magnesium and the equipment decks were aluminum. The solar arrays were aluminum core with a fiberglass (SiO_2) outer face. The bellyband panels were covered with thermal paint and second surface mirrors, and

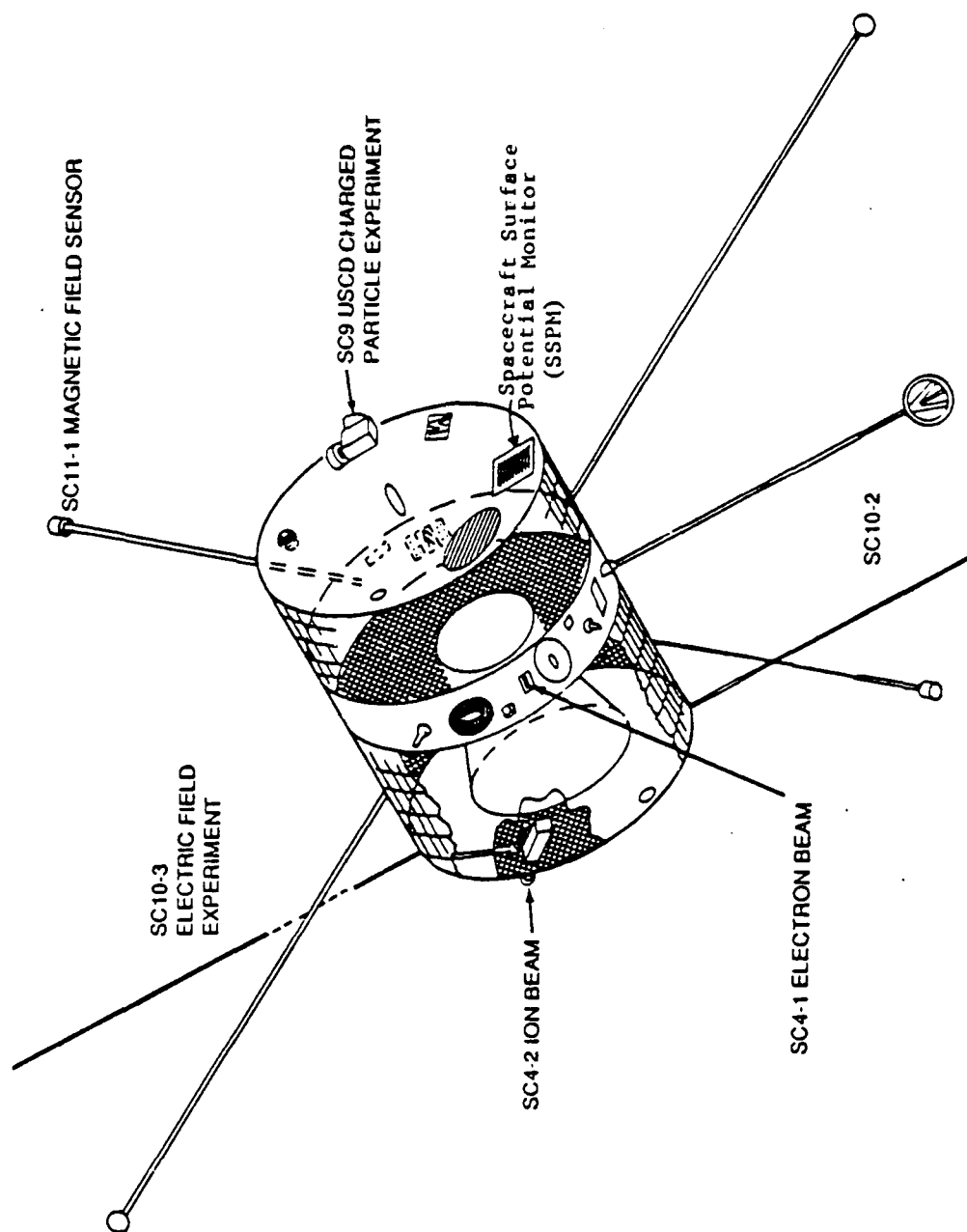


Figure 1. SCATHA Satellite {Ref. 4}

acted as waste heat radiators. The forward cylinder end was coated with gold, except for some sample patches. {Ref. 4}

2. Spacecraft Orbit and Environment

The vehicle was inserted into a near-geosynchronous, elliptical orbit with a perigee of 5.5 R_E and an apogee of 7.7 R_E . The orbit period was 23.5 hours, and the inclination to the equatorial plane was 7.8 degrees. The satellite axis was perpendicular to the earth-sun line, and the vehicle had a spin period of 59 seconds. The satellite encountered 40 day eclipse periods in both the fall and the spring. During these times, the spacecraft was shadowed for approximately 1 hour per day. Figure 2 gives a schematic of the orbit. The view is from above the earth's north pole. {Ref.5}

The environment of the SCATHA spacecraft consisted of two main regimes, the plasmasphere and the plasmasheet. The nature of these regimes, particularly the ion composition, is important in determining the magnitude of the vehicle's interaction with the environment, for example, the sputtering yield. The boundary between these regimes (the plasmopause) is well defined, but varies with solar activity and solar wind parameters. The spatial regions are depicted in Figure 3. The view depicts the northern hemisphere. {Ref. 6}

The innermost region is the plasmasphere. The density is generally greater than 10^6 m^{-3} . and the

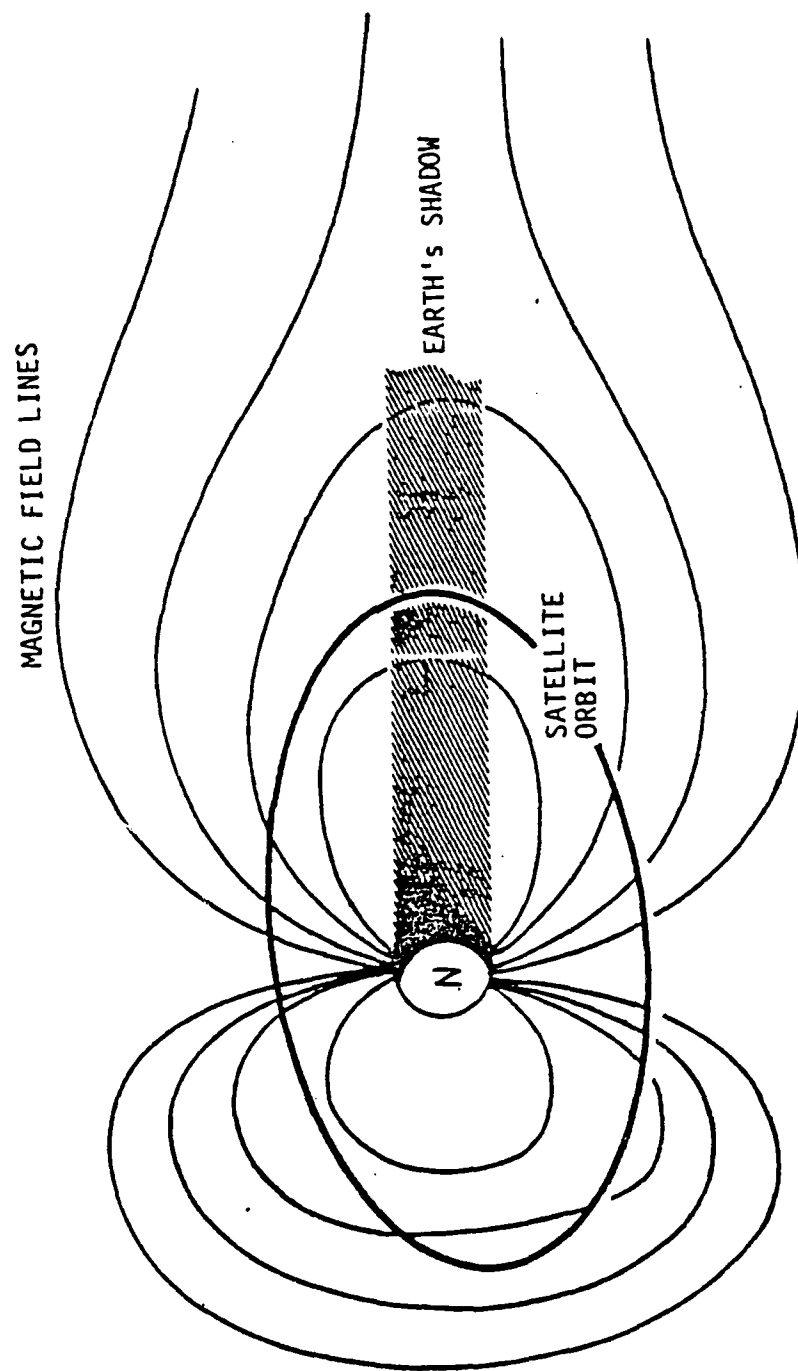


Figure 2. SCATHA Orbit {Ref.4}

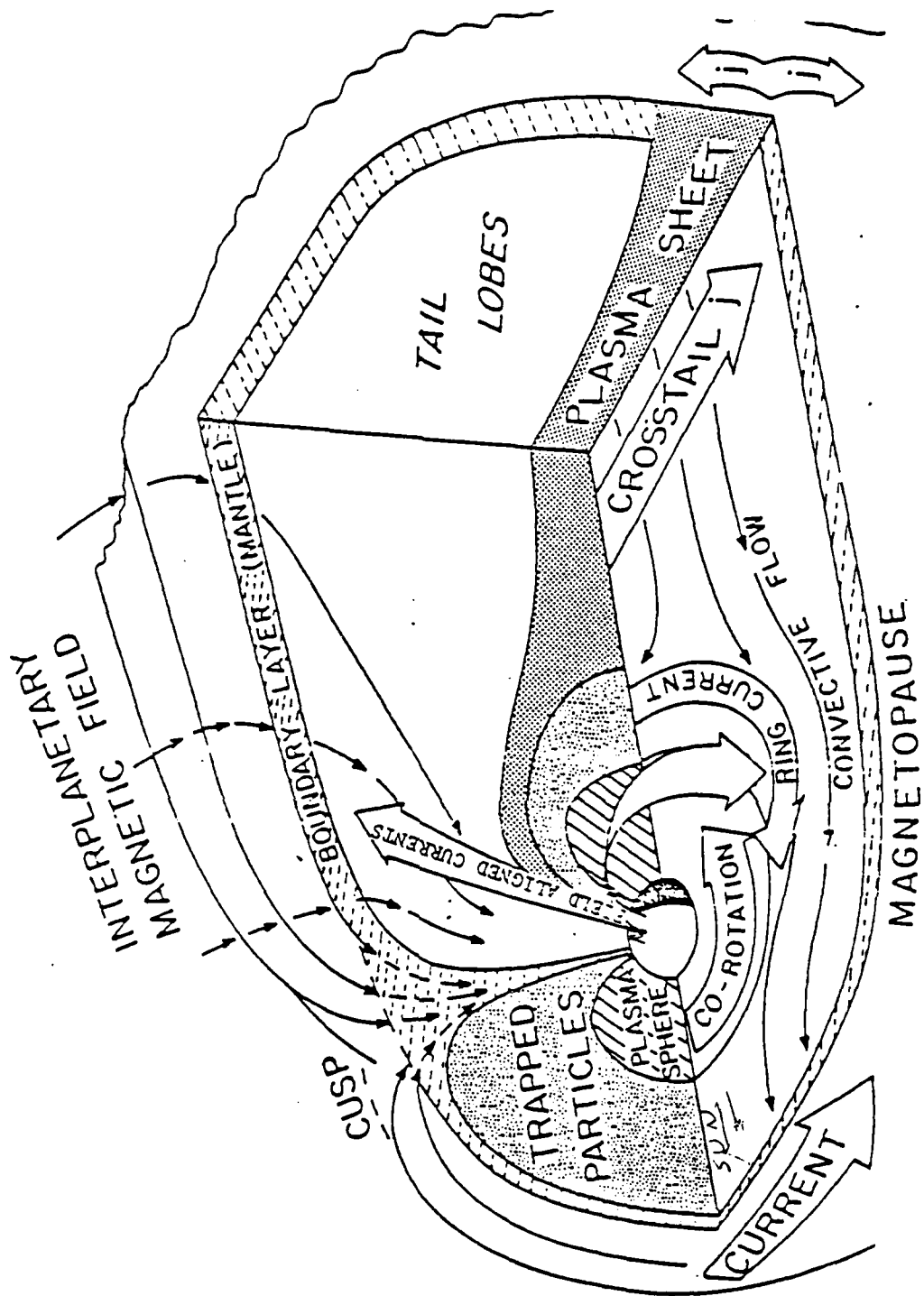


Figure 3. Regions of Space near Earth {Ref. 6}

temperature is less than 1 eV. The dominant ion is H^+ , with O^+ and He^+ contributing approximately 20% of the energy density. The source of these ions is currently considered to be the ionosphere. {Refs. 6,7,8}

Overlapping the plasmasphere is the ring current. It consists of a hot, thin plasma, with densities normally less than 10^6 m^{-3} and temperatures greater than 10 keV. Again, H^+ is the dominant species (93% of the energy density) while O^+ and He^+ are typically minor constituents. During quiet times the principal source of these ions appears to be the solar wind. During active times, a large O^+ constituent indicates ionospheric sources. {Refs. 6,7,8}

The plasmasheet is the region outside the plasmopause, and like the ring current, consists of a hot, diffuse plasma. Densities on the order of $10^5 - 10^6 \text{ m}^{-3}$ and temperatures near 10 keV are common. At quiet times, the composition is 90% H^+ and 10% O^+ and He^+ . At active times, large O^+ ratios (>50%) are observed. This is a mixing zone, containing particles of both terrestrial and solar origin. Large negative potentials are found on spacecraft in the plasmasheet, particularly when the satellite is in eclipse. Table 1 shows the various ions in the magnetosphere, and their sources. {Refs. 6,7,8}

An interesting feature of these areas is the variability of the ion composition of the plasmas observed

during magnetically active periods. In the ring current, for example, it has been observed that O^+ contributes a minimum of 23% of the storm time energy density, and may contribute much more. Also, the He^+ contribution increases, and adiabatic acceleration of these solar wind particles may leave them with energies up to 32 keV. Table 2 gives some typical values for storm time ring current composition. {Refs. 7,8}

The plasmasheet region has a direct source of O^+ , in field aligned beams streaming from the ionosphere. The H^+/O^+ ratio of the beams has been found to be 6/1 {Ref. 8}. Additionally, it has been observed that in the $L = 6 - 8$ region (e.g., the SCATHA orbit), during periods of high magnetic activity ($K_p \approx 5$), the O^+ density becomes comparable to that of H^+ . (The McIlwain 'L' parameter is defined by $R = L \cos^2 \theta$, where R is the distance in earth radii, and θ is the magnetic latitude.) K_p is a measure of the general level of magnetic activity caused by the solar wind. The K_p scale is quasi-logarithmic, and runs from 0-9, with 0 the low end and 9 the high. On several occasions, the O^+ density has been found to reach 70%. Table 3 lists some values for the storm time magnetospheric bulk plasma composition. {Refs. 6,7,8}

3. Instruments

The data for this experiment came primarily from the University of California, San Diego auroral particles

experiment, SC-9. This experiment was composed of five detectors; two pairs of rotating ion and electron detectors, and one fixed ion detector. Figure 4 depicts the detector arrangement. The rotating detectors scanned in orthogonal planes and were designated the Hi set and Lo set. The Lo detector rotated from -20 deg to 200 deg, with 70 deg along the spacecraft spin axis. The Hi detector scanned the same range, but it was more symmetrical, with its midpoint on a line parallel to the spin axis. Thus, it could not depress more than 20 degrees below the forward end plane. The fixed detector looked radially away from the spacecraft, in the same plane as the Lo detector. The detectors had an angular resolution of 5 by 7 deg. The geometry is illustrated in Figure 5. {Ref. 4}

The Hi set covered an energy spectrum from 1 eV to 81 keV. The Lo rotating set, and the fixed detector, scanned from 1 eV to 2 keV. For all detectors, a complete energy scan required 16 seconds and was covered in a series of 64 logarithmic steps. The energy resolution at each step was approximately 20%. Additionally, the detectors could be ordered to dwell at fixed positions and/or energies. {Ref. 4}

The detectors were composed of three parts; an electrostatic analyzer, an electrostatic focussing lens, and a spiraltron particle sensor. The analyzer provided the energy differentiation for the system through curved plates and an applied voltage. The lens focussed the particles on

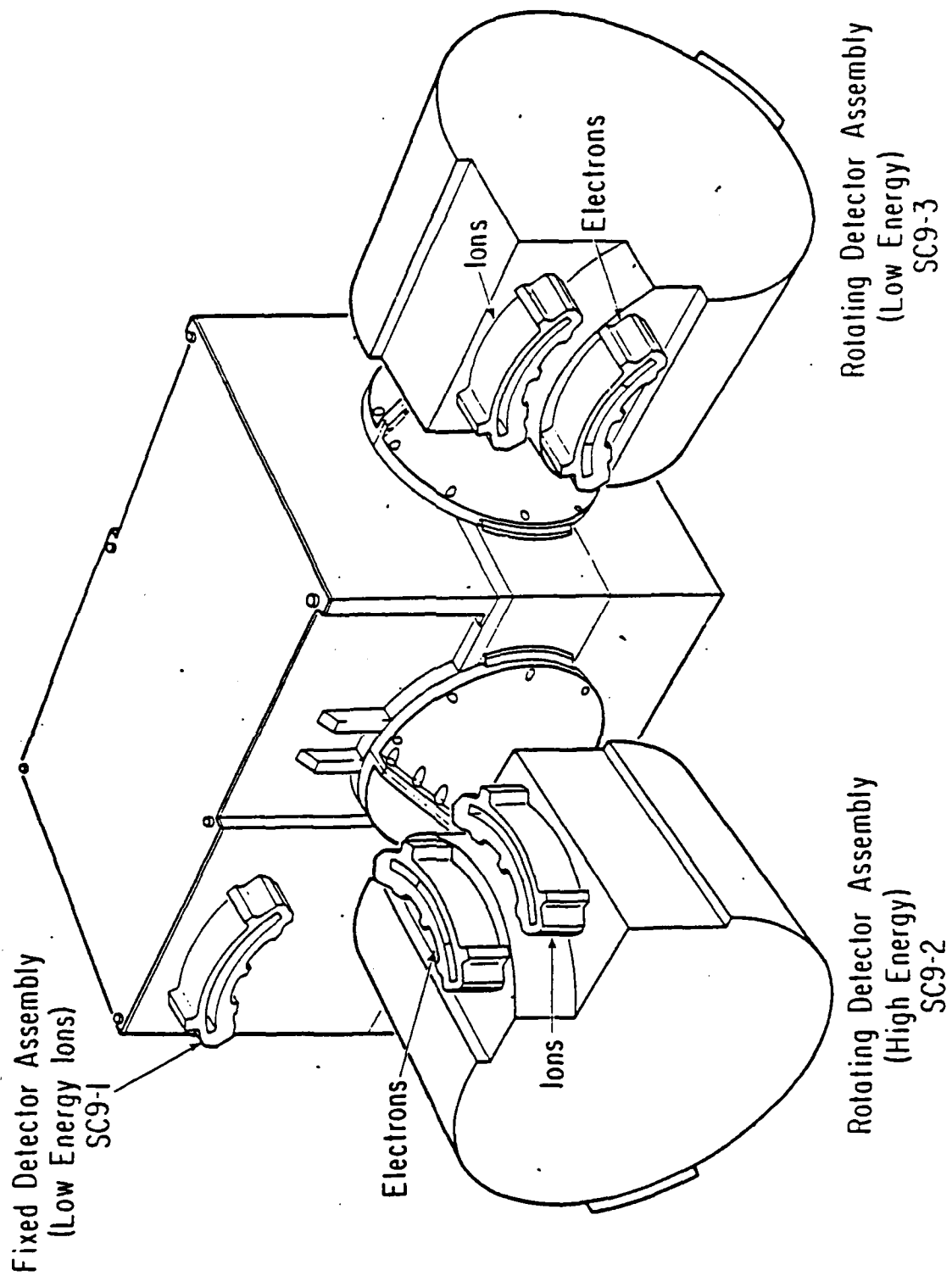


Figure 4. SC-9 Detector Arrangement {Ref. 4}

SCATHA SC-9

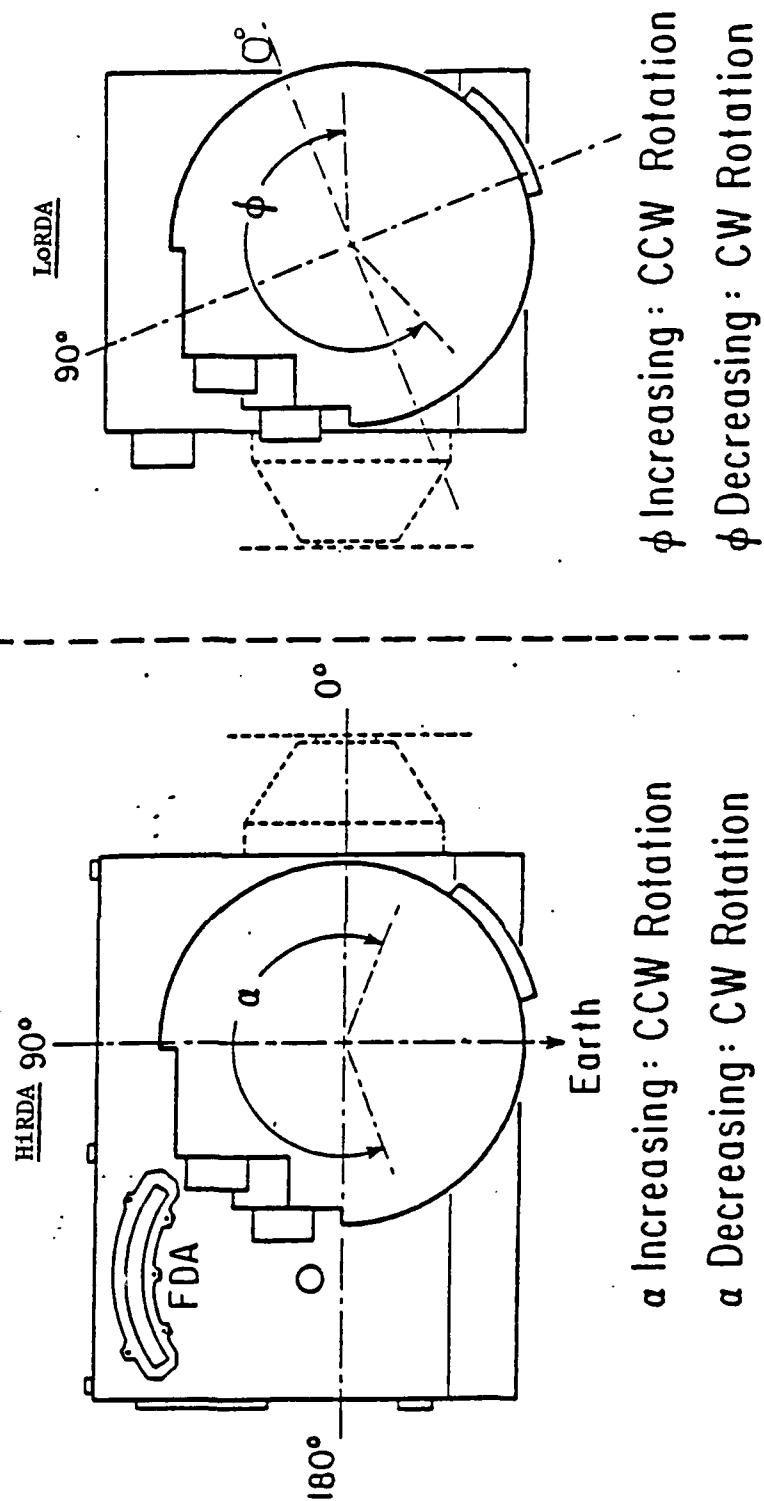


Figure 5. SC-9 Detector Angular Coverage {Ref. 4}

the sensor center by means of two grids, one at ground and the other at the analyzer potential. The sensor was rated to 10^7 counts per second. {Ref. 4}

4. Ion Gun

An ion gun was installed on the SCATHA spacecraft to investigate the efficiency of an ion emission system in modifying satellite potentials. In particular, it could be used to develop negative voltages on the vehicle. The experiment utilized xenon gas ionized by cathode discharge and accelerated by either a 1 or 2 kV potential drop. The beam current could be varied incrementally from 0.3 mA to 2.0 mA. The package also included an electron source that could be configured to neutralize the particle beam or to provide an electron beam. {Ref. 9}

C. OTHER SATELLITES

Although SCATHA was the primary source of data for this thesis, two other satellites provided significant information. These satellites, ATS-6 and ISEE-1, will be briefly discussed in the following paragraphs.

1. ATS-6

ATS-6 was a large three-axis stabilized spacecraft placed in geosynchronous orbit in 1974. Its major features are shown in Figure 6. The large antenna was significant, since it fostered differential charging by shadowing other spacecraft surfaces. The satellite had an environmental measurements package above the spacecraft dish. This

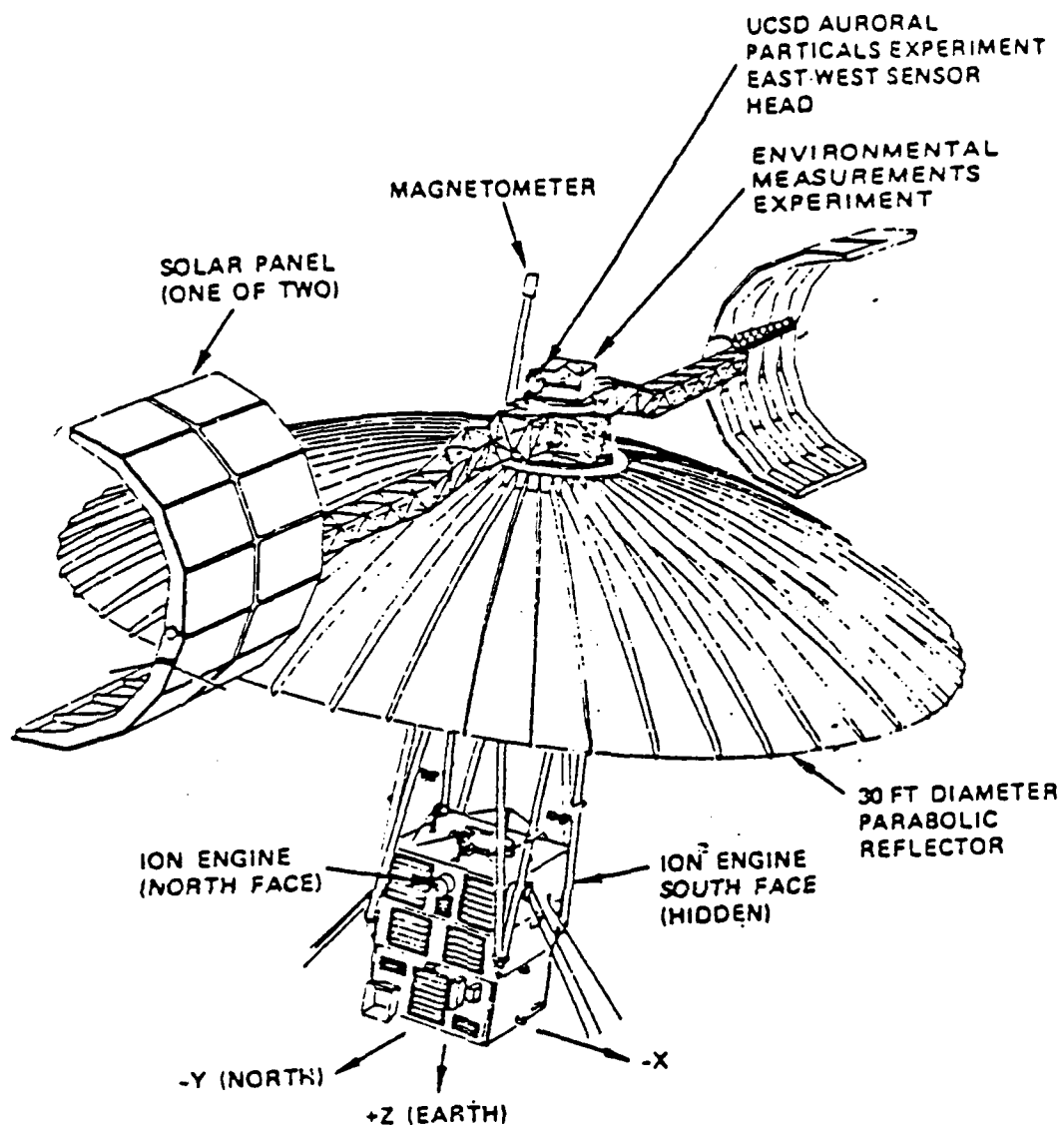


Figure 6. ATS-6 Satellite {Ref. 12}

package contained rotating particle detector sets similar to those found on SCATHA. {Ref.2}

2. ISEE

The ISEE-1 satellite was launched in 1977 as part of a three spacecraft mission to investigate the magnetospheric plasma. With this in mind, the satellite was designed to minimize absolute and differential charging by using conducting materials and low impedance connections to ground. Regardless, the satellite was observed to charge on several occasions. The spacecraft was equipped to measure electric fields, plasma waves, and plasma composition. The most important of these, for our purposes, is the plasma composition experiment which contained an ion mass spectrometer. {Ref. 10}

D. SPACECRAFT CHARGING

The theory of spacecraft charging will now be reviewed, as differential charging will play a significant role in later discussions. In general, a probe immersed in a plasma will develop some potential relative to that medium. This "floating" potential is determined by the balance of the currents incident upon the probe. The primary currents in deciding the potential are; the ambient plasma electron and ion flux, the photoelectron emission due to sunlight, and the fluxes due to secondary and backscattered electrons. These currents are schematically illustrated in Figure 7. The left half of the figure depicts typical eclipse

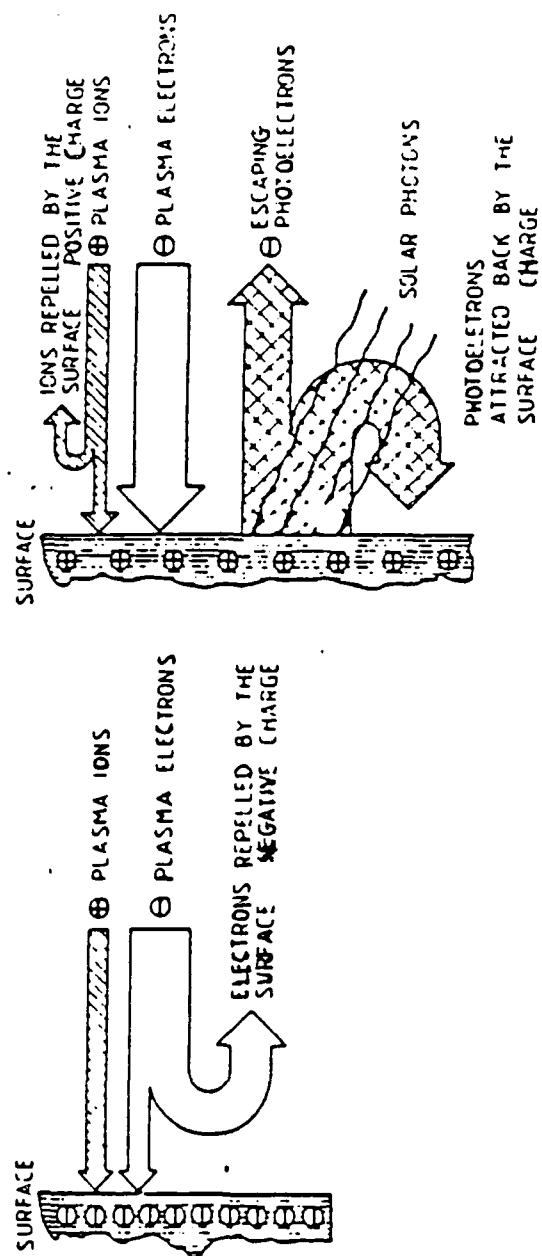


Figure 7. Charging Current Schematic {Ref. 12}

conditions (negative satellite), and the right half the currents present in sunlight. {Refs. 11,12,13}

In daylight, the dominant current is that of the photoelectrons which, although material dependent, has typical saturation current densities in the range 5 - 50 $\mu\text{A}/\text{m}^2$. This current density overshadows that of the ambient plasma, which is generally below 1 $\mu\text{A}/\text{m}^2$ for electrons, and .1 $\mu\text{A}/\text{m}^2$ for ions. The value of the secondary electron emission current is highly dependent on both the material and the electron temperature. It is this material dependence which allows differential charging, even in eclipse. A normal secondary emission curve will have a yield greater than one in some middle energy range (typically 50-500 eV), and yields less than one at higher and lower energies. The point in the high energy range where the yield decreases to one is called the cross-over point and is critical in determining the effect of the secondary emission current. The energy at which this point occurs, and the peak yield, varies with target composition. Low energy ambient distributions ($T \leq 5$ keV) impacting the spacecraft will create large secondary fluxes, in fact greater than the ambient electron flux, and the spacecraft will charge positively. High energy electron distributions ($T \geq 5$ keV) will produce lower secondary emission yields, and the vehicle will gain negative charge. Thus, the potential of the satellite is determined by the high energy electron

flux. The threshold electron temperature for which charging may occur is typically in the 5-10 keV region. There is an additional criteria, the critical energy, which also must be met. This is an upper energy bound on the distribution function resulting from magnetospheric convection processes. It is also termed the Alfvén boundary, and must exceed 15-20 keV for charging to occur. {Refs. 11,12,13,14,15,16}

A simplistic equation to represent the situation may be given by:

$$(1-1) \quad I_{net} = I_{amb} + I_{sec} + I_{photo}$$

Thus, during daylight, when the photoelectron current dominates, the net current is positive (toward the spacecraft), and the spacecraft will start to charge positively. As this happens, the flow of ions to, and electrons from, the spacecraft will be inhibited, and the value of I_{net} will decrease. When the value reaches zero, the currents are balanced and the spacecraft will remain at that potential until the balance is disturbed. For eclipse events, I_{photo} is zero, and the balance is effectively between the ambient and secondary electrons. For a low energy electron distribution, the potential is restricted to low values (+2 to +5 V), while for high energies, the potential may reach -1 to -20 kV. {Refs. 2,11}

In addition to absolute charging, a spacecraft may charge differentially. That is, separate insulated portions of the spacecraft surface may charge to different

potentials. If two insulators are exposed to the same environment, but have different secondary emission characteristics, then their ability to shed the excess charge in the form of a current will differ, and a potential will develop between them. Also, if two portions are exposed to differing environments, they will each charge to different potentials. The environment may differ over the range of a spacecraft in a number of ways. Frequently, pitch angle anisotropies in the ambient plasma may cause different fluxes to impact separate spacecraft regions. Additionally, if one portion of the spacecraft shadows another continually (see ATS-6), the shadowed area will not emit photoelectrons and will charge negatively compared to the rest of the satellite. Also, in lower orbits, an electric field induced in the satellite frame of reference ($E=v \times B$) may cause variations in the ambient particle distributions. {Refs. 2,12,13}

Differential charging is believed to be the cause of numerous control logic upsets on various spacecraft. As the differential potential increases, there will be a tendency for it to discharge in the form of an arc. This arc creates an electromagnetic pulse which is read by the control circuits as a command signal. For large discharges there may even be physical damage or destruction to the arcing areas. {Refs. 17,18}

Spacecraft charging may be controlled by active and passive measures. Active trials using ion and electron guns were carried out on ATS-6 and SCATHA with some success. Passive attempts, such as those on the ISEE satellites, using low impedance connections and conducting surfaces were also moderately successful. {Refs. 10,19,20}

E. SPUTTERING

The general theory of sputtering is very significant to this thesis, as it is postulated to be the source of the observed spacecraft generated ions. Sputtering is defined as the ejection of material from solid surfaces under ion bombardment. The observed features of the sputtering yield (number of target atoms sputtered per incident ion) are; a) its dependence on atomic number, b) its correlation with the periodic table, c) its correlation with the heat of sublimation of solids, d) its relation to the efficiency of momentum transfer, e) and its dependence on incident ion energy, such that it increased to a maximum and then decreased. Figure 8 is a plot of the sputtering yield for aluminum as a function of incident ion energy and mass {Ref. 21}. We see that the yield maximum increases with ion mass, and shifts to higher energies. These observations led to theories based on atomic collision cascades. Such cascades are created by one incident ion impinging on the lattice and transferring energy to other atoms, which in turn participate in collisions. These theories are based on the

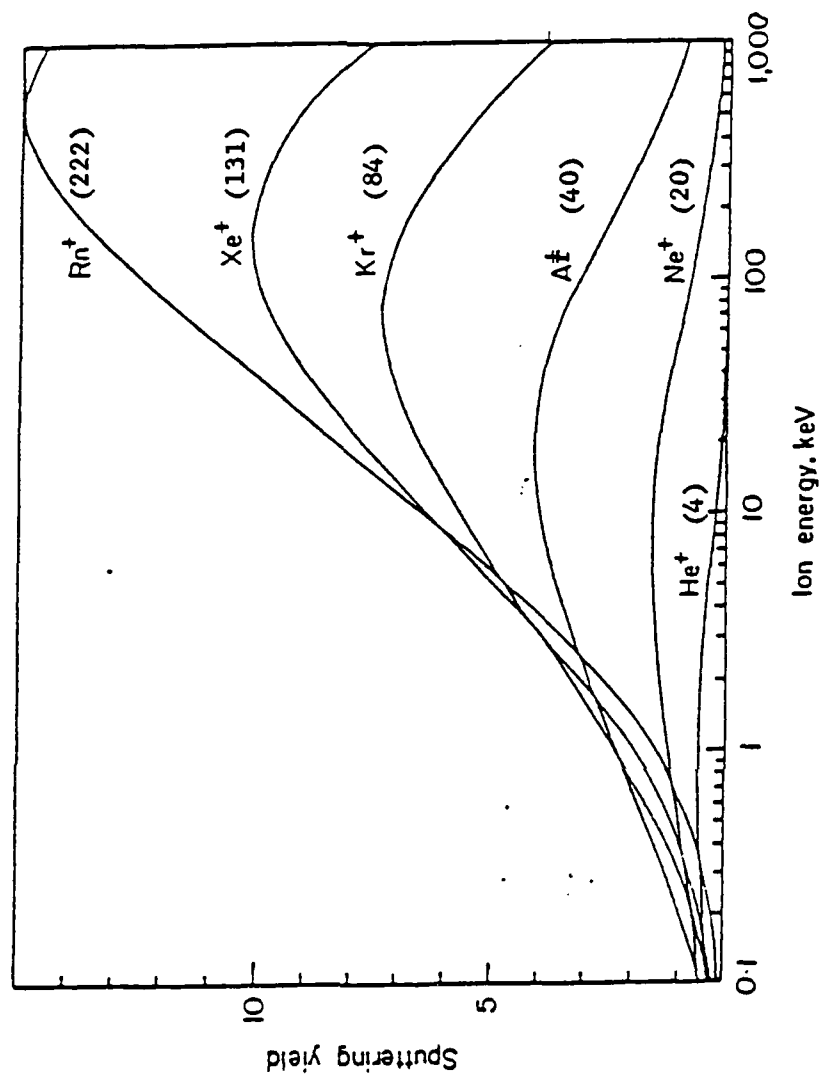


Figure 8. Sputtering Yield for Aluminum {Ref. 21}

simple elastic collisions of classical mechanics, and therefore satisfy the observed dependence on atomic number and momentum transfer. The correlation to the heat of sublimation is explained by assuming the effect of some surface binding energy. The maximum in the energy dependence occurs by postulating some optimum energy deposition depth, beyond which the ability of the cascade particles to reach the surface decreases. {Refs. 21,22,23}

The most comprehensive, detailed, and successful of the collision cascade theories is the Sigmund - Thompson theory. This theory is actually two theories developed separately, but they complement one another by explaining different facets of sputtering. The portion developed by Sigmund treats the sputtering yield of an amorphous target. Thompson's theory explains the energy distribution of the sputtered atoms. The development of both these theories will be briefly discussed, followed by a comparison with experimental results. {Refs. 22,23,24,25}

1. The Sigmund Theory

The Sigmund theory focusses on the amount of energy deposited in the surface layers of the solid as the driving factor for the yield. The basic expression for the sputtering yield is then $S=rF$, where r is a constant depending only on the properties and state of the target, and F is a function describing the interaction of the two particles. In order to evaluate this expression, Sigmund

chose as his starting point the sputtering of an amorphous target, and used transport theory to describe the collision cascade in random media. {Refs. 23,24}

The theory assumes a planar surface and an atom starting its motion at time $t = 0$ and position $x = 0$. The initial quantity of interest is $G(x, \vec{v}_0, \vec{v}, t) d^3v_0 dx$. This is the average number of atoms moving at time t in a layer (x, dx) with a velocity (\vec{v}_0, d^3v_0) due to an impact by a single atom at velocity \vec{v} . This quantity is then used in a Boltzmann transport equation that equates the initial number G with a later G which is dependent on the probability of collision. The equation is then integrated to eliminate some of the variables. Two functions are defined to simplify the integration.

$$(1-2) \quad F(x, \vec{v}_0, \vec{v}) = \int G(x, \vec{v}_0, \vec{v}, t) dt$$

$$(1-3) \quad H(x, \vec{v}) = \int F(x, \vec{v}_0, \vec{v}) |v_{0x}| d^3v_0$$

The function F is the total number of atoms which penetrate the plane x with a velocity (\vec{v}_0, d^3v_0) during the collision cascade development. $H(x, \vec{v})$ is the sputtering yield at the plane x for a source of sputtered particles at $x = 0$. This function may be defined for either forward or backward sputtering. For our purposes, we will choose backward sputtering. Backward sputtering is emission directed opposite to the initial direction of incidence. {Refs. 23,24}

The remaining expression in H is expanded in terms of Legendre polynomials and then transformed into a moment equation by multiplying each term by x^n and integrating over x . With the assumption that the electronic losses to electrons are small and isolated from nuclear collisions, the electronic and collisional cross sections may be separated {Ref.26}. This yields a final expression which includes the electronic stopping cross section, and the differential cross section for elastic scattering. {Refs. 23,24}

The next step is to determine the functions describing the electronic and elastic cross sections. The electronic cross section used is $S_e = K E^*$, where the constant K is determined using Thomas-Fermi arguments {Ref.27}. The elastic cross section is derived from classical mechanics, and a power approximation of the Thomas-Fermi interatomic potential. The equation is then given by;

$$(1-4) \quad d\sigma(T) = C E^{-m} T^{-1-m} dT$$

where C is a constant, T is the transferred energy, and E the initial energy. The variable m comes from the power approximation. $m=1$ corresponds to Rutherford scattering, and $m=0$ approximates scattering from a Born-Mayer potential. If these values are substituted in the expression from the previous paragraph, the following is achieved;

$$(1-5) \quad H(x, E, \beta) = \frac{3}{4\pi^2} \frac{F(x, E, \beta)}{N C_0 U_0}$$

where β is the direction cosine of the ejection vector, and $F(x, E, \beta)$ is a function describing the distribution of the energy deposited in the solid. C_0 is a constant, and U_0 is the binding energy. In general, the function $F(x, E, \beta)$ is found to obey the following relation;

$$(1-6) \quad F(x, E, \beta) = \alpha N S_n(E)$$

where α is a dimensionless constant dependent on the ratio M_2/M_1 , N is the atom density, and $S_n(E)$ is the nuclear stopping power, given by $S_n(E) = \int T d\sigma$. Additionally, we now restrict ourselves to sputtering in the unit normal direction. The function α is illustrated in Figure 9. {Refs. 23, 24}

Using all of the previous relations, we can then define some general expressions for the sputtering yield. For low energies ($E \leq 1 \text{ keV}$), we have

$$(1-7) \quad S(E, \beta) = \frac{3}{4\pi^2} \alpha \frac{4M_1 M_2}{(M_1 + M_2)^2} \frac{E}{U_0}$$

$S_n(E)$ in this equation was evaluated by integrating $d\sigma$ with a value of $m=0$. The Born-Mayer potential is more accurate at lower energies than the Thomas-Fermi approximation. The expression for higher energies is;

$$(1-8) \quad S(E, \beta) = 3.56 \alpha \frac{Z^u}{(Z_1^{2/3} + Z_2^{2/3})^u} \frac{M_1}{(M_1 + M_2)} \frac{S_n(E)}{U_0}$$

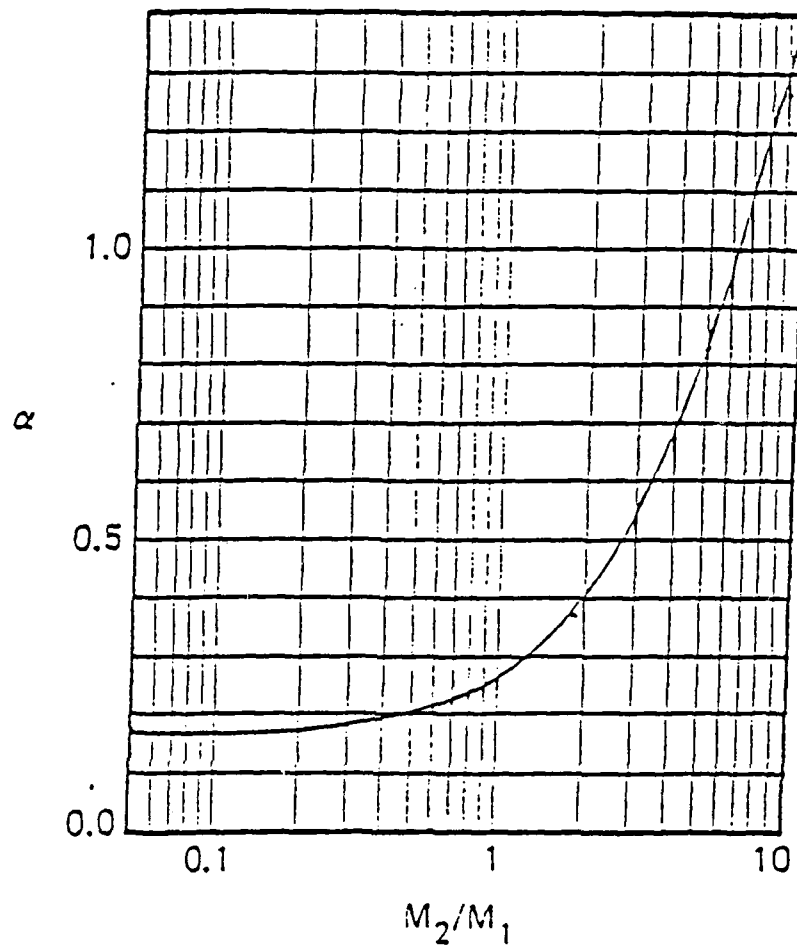


Figure 9. $\alpha(M_2/M_1)$ vs. M_2/M_1 {Ref. 23}

The function $s_n(\epsilon)$ is the reduced stopping power. This is a universal function for Thomas-Fermi interactions {Refs. 24,27}. The variable ϵ is the reduced energy, defined by $\epsilon = \frac{aM_2E}{(Z_1Z_2e^2(M_1+M_2))}$, where Z_1 and Z_2 are the atomic number, and a is the Lindhard screening radius. Tabulated values for $s_n(\epsilon)$ are shown in Table 4. The sputtering yield dependence on β was roughly determined to be $(\cos(\theta))^{-1}$. This dependence was derived empirically by Sigmund. {Refs.22,23,24,27}

2. The Thompson Theory

The Thompson Theory was a complete theory of sputtering published in 1968. The portion involving the determination of the sputtering yield was overshadowed by the Sigmund Theory, but the energy spectrum determination has endured. Thompson started his derivation by assuming an infinite solid with recoils at energy E_2 from some primary event. Then, with a density of recoil atoms $q(E_2)dE_2$ per unit time, each generating their own collision cascade, the total number of atoms slowing down through some energy range E' is

$$(1-9) \quad n(E') = \int_{E'}^{\infty} q(E_2) \mu(E_2, E') dE_2$$

The mean rate of energy loss is given by $\vec{v}dE'/dx$, where \vec{v} is the velocity. Assuming an isotropic distribution, one may define

$$(1-10) \quad n(E', \vec{r}) dE' d\Omega' = \int_{E'}^{\infty} \frac{q(E_2) \mu(E_2, E')}{\vec{v} \cdot \frac{dE'}{dx}} dE_2 \frac{dE'}{4\pi}$$

From this, the flux may be determined,

$$(1-11) \quad \phi(E', \vec{r}) dE' d\Omega' = \vec{v} \cdot \vec{n}(E', \vec{r}) \cos\theta dE' d\Omega'$$

The theory now assumes that the infinite solid is cut in half and the flux is observed. Also, some expressions are needed for the functions above. $\mu(E_2; E')$ is the number of displaced atoms and may be approximated by $\beta E_2/E'$, where β is a constant of order unity. Similarly, dE'/dx may be replaced with E'/D , where D is the interatomic spacing. Using these relations we obtain

$$(1-12) \quad \phi(E', \vec{r}) dE' d\Omega' = \frac{\beta D}{E'^2} \int_{\infty}^{\infty} q(E_2) E_2 dE_2 \frac{\cos\theta d\Omega'}{4\pi} dE'$$

This function ϕ is the flux inside the surface, and must be transformed to that observed outside. This is accomplished by assuming a binding force normal to the surface which will decrease the normal kinetic energy, but leave the parallel component unaffected. Thus, the effect will be a bending of the particles trajectory. With the energy equations, and the relationship between the inner and outer angles in hand, we come to the final expression

$$(1-13) \quad \phi(E, \phi) dE d\Omega = \frac{\beta D \cos\phi}{4\pi(1+U_0/E)^3 E^2} \int_{\infty}^{\infty} q(E_2) E_2 dE_2 dE d\Omega$$

In this equation, U_0 is the binding energy, E is the emitted particle energy, and ϕ is the angle of the trajectory from the surface normal. The chief features are the proportionality to $E/(E+U_0)^3$ and the $\cos\phi$ dependence.

Figure 10 is a plot of this function versus energy. For high energies, the spectrum will fall off as $1/E^2$, and for low energies, the binding energy will have an impact. The maximum of this curve occurs at $U_0/2$. Figure 11 is a plot of the measured energy distribution, with the model overlaid. It can be seen that up to approximately 1000 eV, the model matches the observed spectrum quite closely. Since the majority of the sputtered particles are in the energy region that follows the $1/E^2$ curve, this theory is quite effective in describing the data. {Refs. 22,24}

3. Comparison of Theory with Experiment

To evaluate the applicability of these theories, we must determine how closely they recreate experimental results. Therefore, we will look at the sputtering yield as a function of ion energy, angle of incidence, incident and target masses, and surface binding energy. The energy dependence of the sputtering yield is contained in the energy dependence of the stopping power. Calculated yields using equations 1-7 and 1-8 are compared with experimental values in Figure 12 for copper {Ref. 23}. The solid line is the high energy result, and the dotted line is the plot for the low energy equation. The experimental results are marked by the various geometric shapes. In addition, calculated and measured yields for various materials are listed in Table 5 {Ref. 23}. It can be seen that the correlation is reasonable, normally within a factor of two.

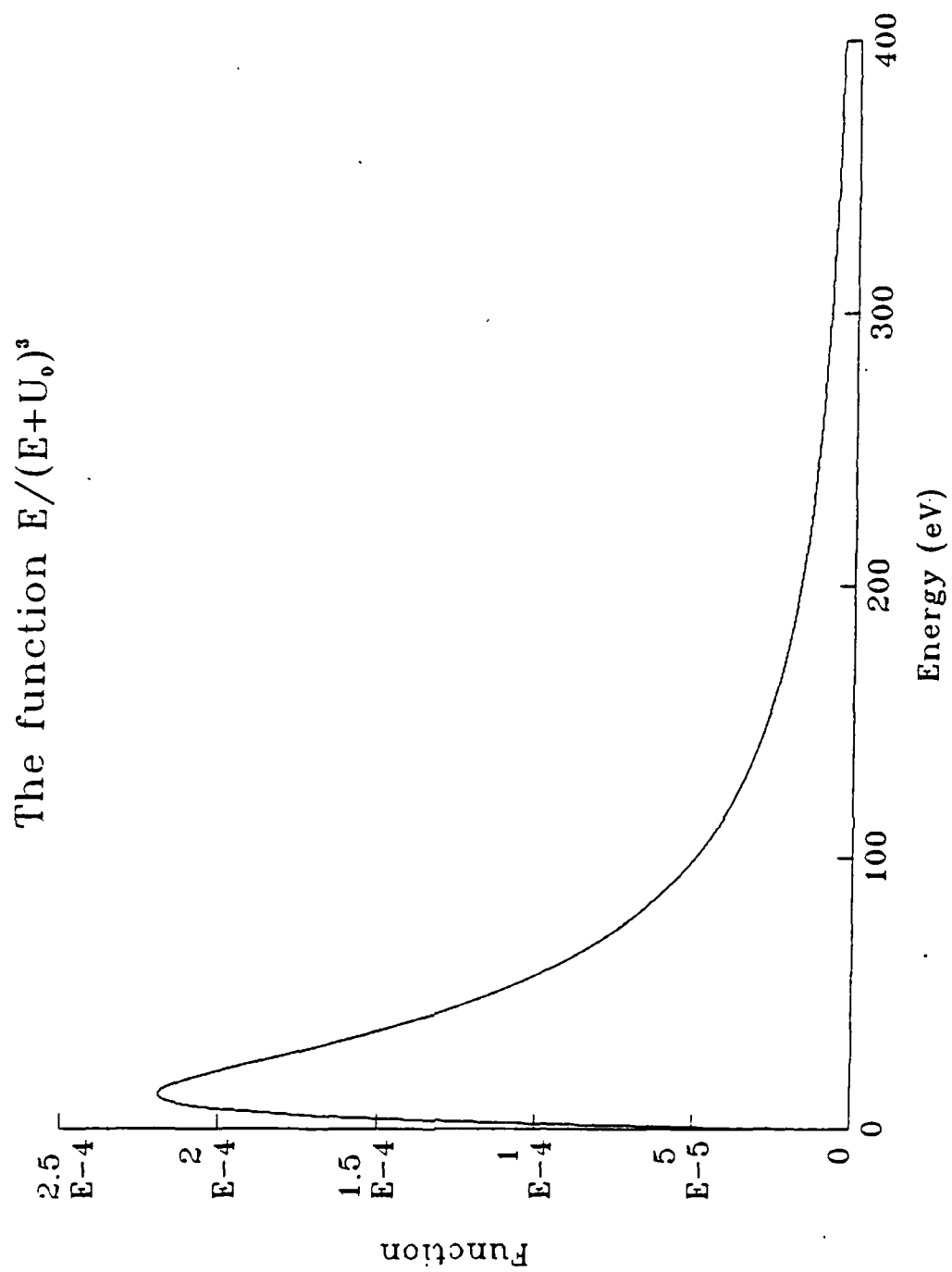


Figure 10. The Function $E/(E + U_0)^3$

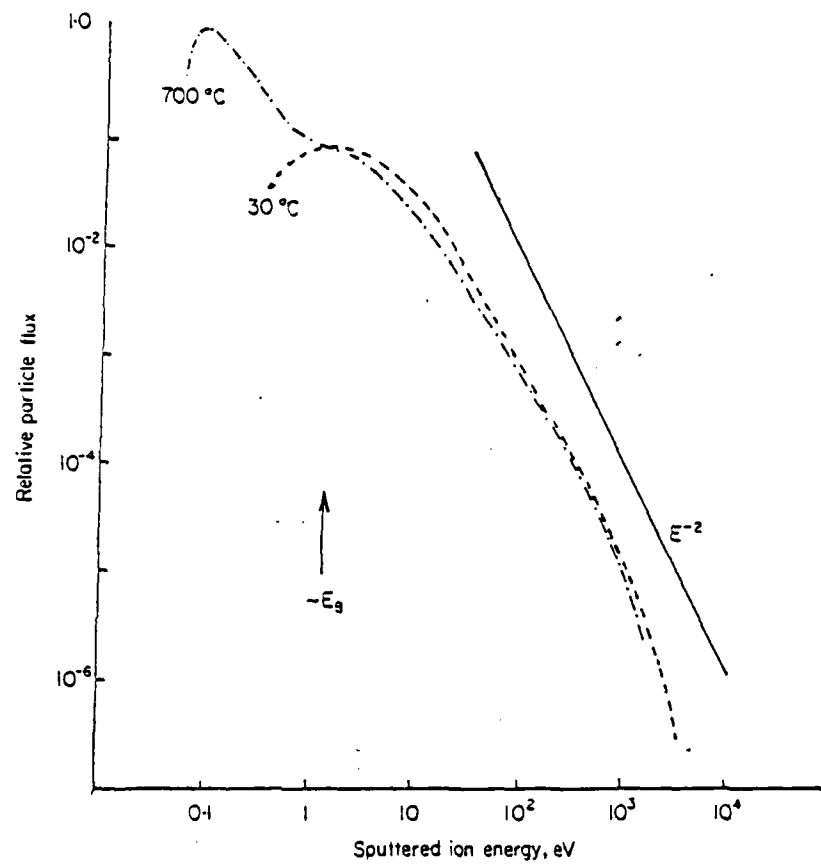


Figure 11. Energy Distribution of Sputtered Gold Atoms
{Ref. 23}

Some of the experimental yields are questionable, as the sputtering yield is known to have a dose dependence. The Sigmund Theory also tends to overestimate sputtering at very low energies (<100 eV). In most cases, experimental data indicates that the yield goes to zero in the 50-100 eV region. {Refs. 22,23,24}

The sputtering yield is a function of M_1 directly and in the factor $\alpha(M_2/M_1)$. Due to the above mentioned dose effects, yield data for masses are generally normalized to the self sputtering yield or the argon sputtering yield. Data for various targets are presented in Figure 13 {Ref. 23}. The top plot displays results for impacts on silicon. The mass of the sputtering ion in AMU is along the horizontal axis and the yield of the ions normalized to the argon sputtering yield on the vertical axis. The other plots are similar for copper and gold. The agreement with theory for silicon is quite good, but decreases for the heavier targets. Sputtering yields for H^+ and O^+ on silicon are illustrated in Figure 14. Since in general we will be discussing silicon or silicon dioxide as a target, we will disregard the lack of agreement for heavier targets in the model which we develop. {Refs. 22,23,24}

The angular dependence of the sputtering yield is considered to be proportional to $(1/\cos\theta)^n$. The exponent, n , is a variable quantity ranging from a little less than 1 to 1.7. For the situations we will be discussing, with

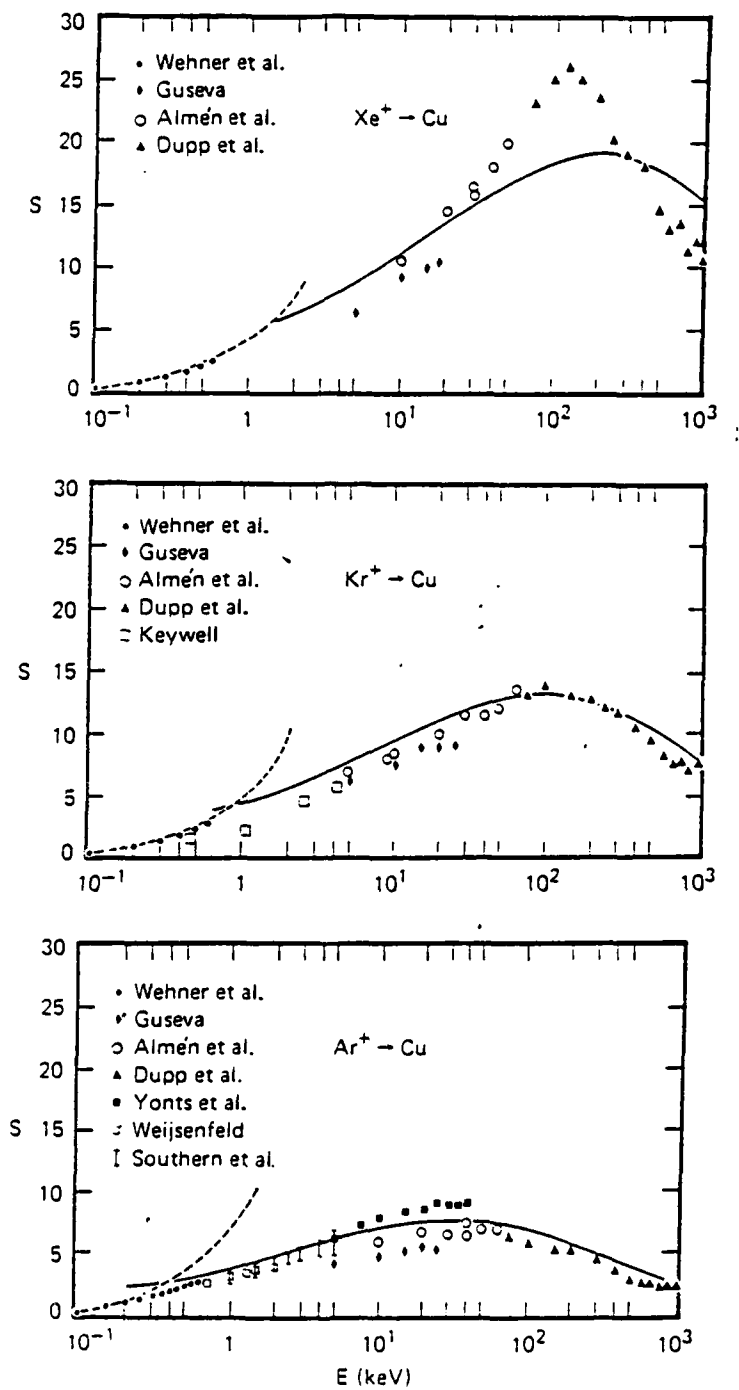


Figure 12. Calculated and Experimental Sputtering Yields for Copper {Ref. 23}

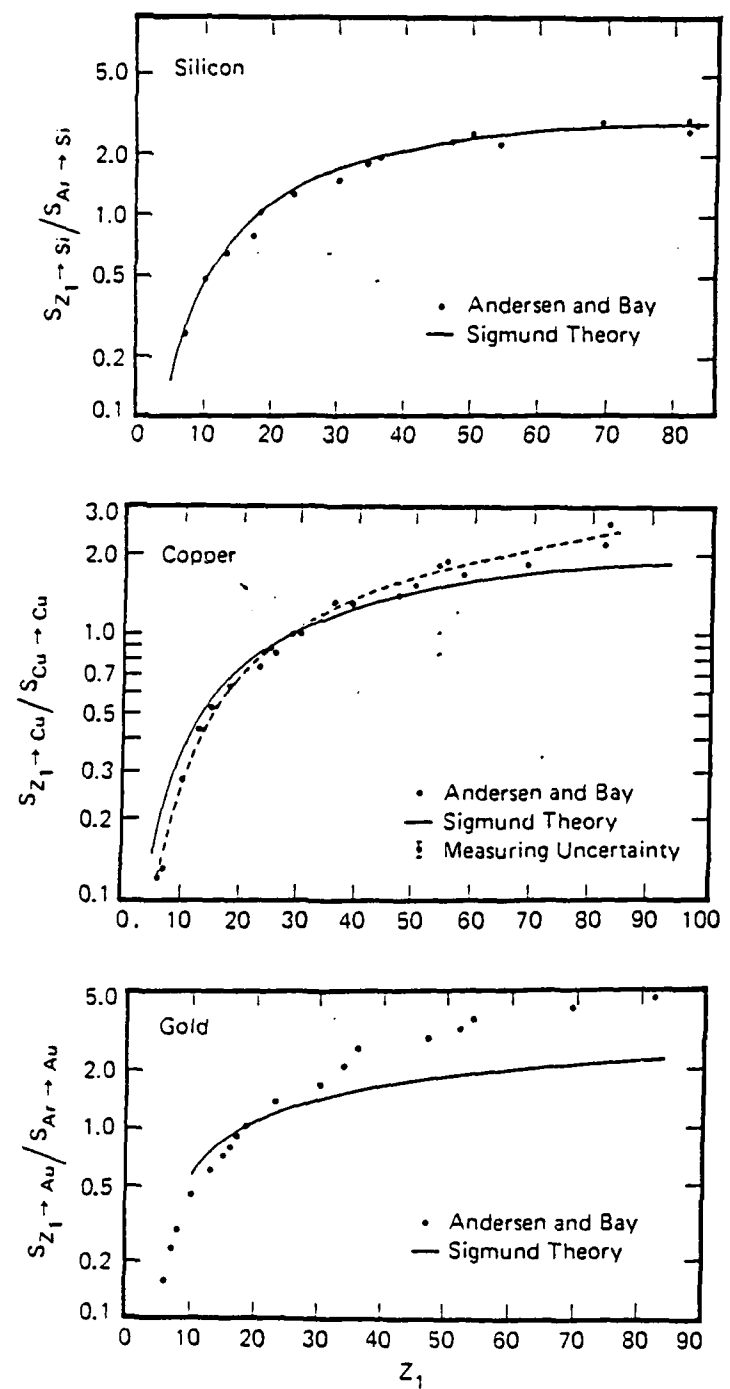


Figure 13. Mass Dependence of the Sputtering Yield for Various Atoms {Ref. 23}

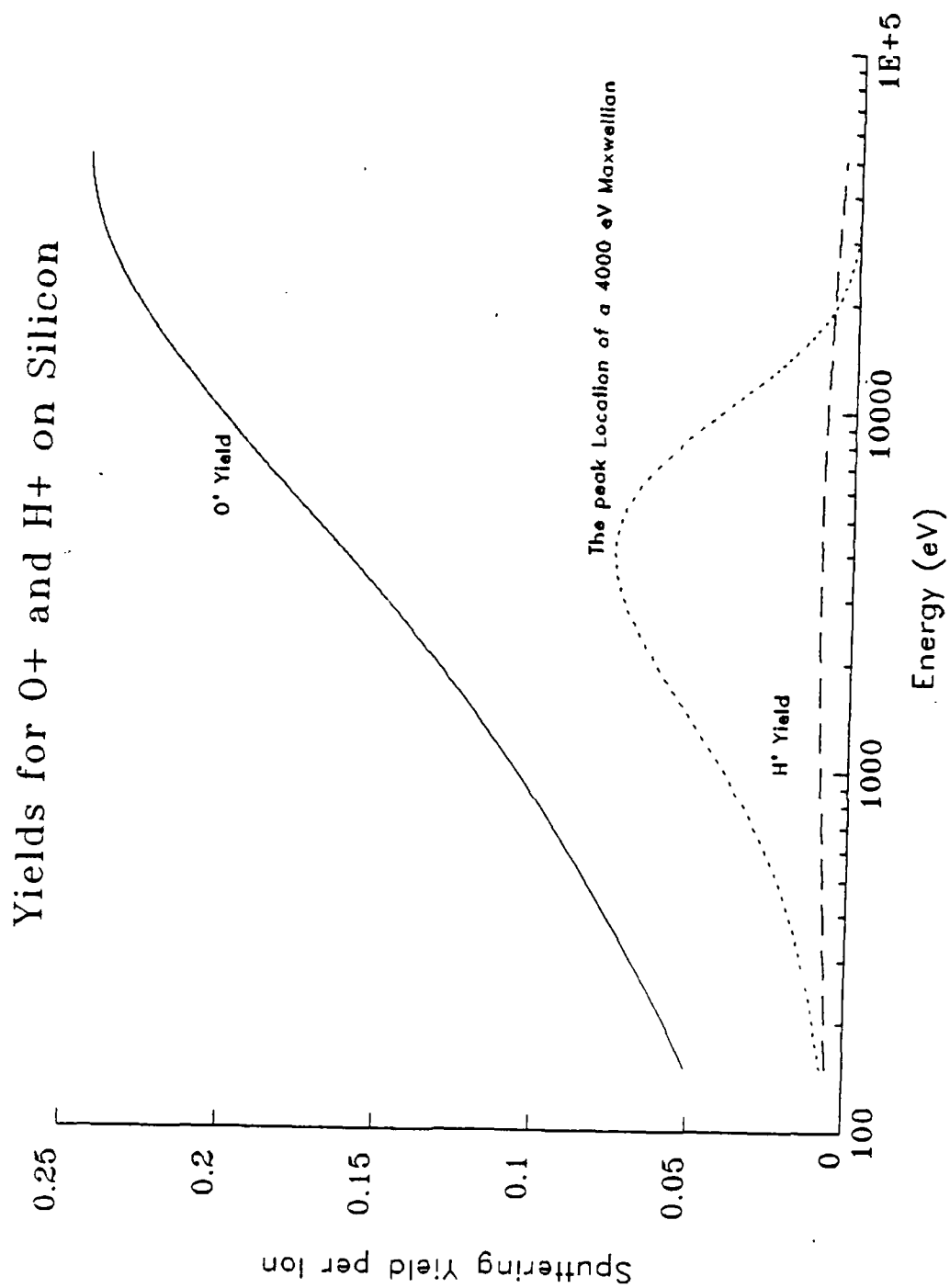


Figure 14. Typical Sputtering Yields for H⁺ and O⁺ on a Silicon Target

$M_2/M_1 > 1$, the value of n is generally taken to be 1.7. Figure 15 is a plot of the dependence on angular incidence from experimental data {Ref. 23}. The dependence ranges up to an incident angle of 70 degrees. Beyond this point, the sputtering yield decreases rapidly to 0. If we attempt to model using only the 0-70 degree range, we will probably be underestimating the yield by approximately 20%. {Refs. 22,23,24}

The yield depends directly on the binding energy, thus the determination of this energy is quite important. Sigmund suggested that the appropriate value for the binding energy would be the sublimation energy of the material. This generally leads to sputtering yield values that are slightly high. Recent work has given theoretical backing for a higher value, but no definite numerical quantity was put forward {Ref. 28}. It has been suggested that the value providing the best results is 17/10 of the sublimation energy {Ref. 29}. If this value is used to recalculate the numbers in Table 5, we get the results in Table 6. It is obvious that in general, the calculated yields in Table 6 are much closer to the experimental yields, than those calculated for Table 5. For calculations in this thesis, we will use the larger value of the binding energy. {Refs. 22,23,24}

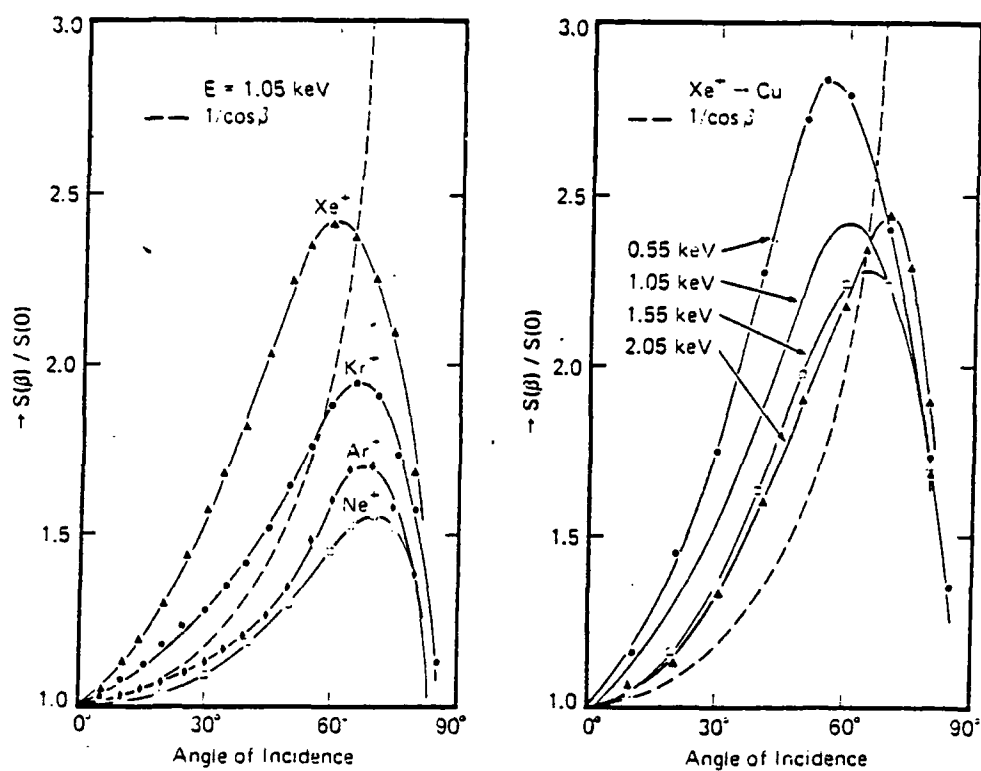


Figure 15. The Dependence of the Sputtering Yield on Angle of Incidence {Ref.23}

4. Limitations of the Sigmund Theory

The theory was devised for amorphous monatomic targets bombarded by atomic ions. It is not so readily applicable to the bombardment of molecular solids, as will be necessary in later calculations. Since several of the reference data points are concerned with bombardment with molecular oxygen, it will be relevant to discuss this type of impact. The case of molecular ions on molecular targets may be treated through computer simulation, but it is an extensive, complicated project, as the probabilities for each collision combination must be calculated. In most cases, it is more appropriate to utilize experimental data if it is available. Such data is often difficult to obtain. Only recently has an effort begun to systematically tabulate the known experimental results and compare them with the theory. The presently tabulated data concerns atomic ions on monatomic targets {Ref. 30}. A great deal of data is also distributed randomly through the literature on other ion-target combinations.

An additional bit of information is available for the yields of monatomic molecules. It has been found for several atoms that the sputtering yield per atom for molecular ions is slightly higher than that for atomic ions {Ref. 31}. The results are listed in Table 7. The yields are greater by approximately a factor of two, while for silicon they range from 1.15 to 1.30. There is a

difference, but it is not drastic. While it is difficult to accurately model the more complicated situations, it should be possible to obtain some approximate results for monatomic molecules that are within a factor of two of the actual results.

F. NASA CHARGING ANALYZER PROGRAM

The NASA Charging Analyzer Program (NASCAP) was developed to accurately model the dynamics of spacecraft response to realistic plasma environments. NASCAP can effectively simulate the charging, in both laboratory and magnetosphere environments of objects that are geometrically, materially, and electrically complex. The program utilizes a timestep procedure, calculating quasi-static steps. The dynamics are driven by charge accumulation from external sources, charge depletion, and conduction in dielectrics. Each timestep includes a full three dimensional electrostatic potential calculation. The calculation of Poisson's equation over a grid is time-staggered with a procedure in which incident charged particle fluxes, leakage currents, emission currents, and induced spacecharge effects are computed based on the current quasistatic conditions. NASCAP is limited to situations where the Debye length is long compared to the dimensions of the examined object. This condition is met for the SCATHA spacecraft. NASCAP can output a time history

of spacecraft charging, potential contours, charge contours, current contours, and particle trajectories.

II. OBSERVATIONS

A. PREVIOUS OBSERVATIONS

Data taken from three satellites, ATS-5, ATS-6, and ISEE-1, will be discussed, prior to presenting P78-2 (SCATHA) results. Observations of the three primary phenomena (triangle peak, shadow peak, diffuse background) on satellites prior to SCATHA will be illustrated.

1. ATS-5

The presence of ions below the charging peak was first reported for ATS-5 {Ref.1}. ATS-5 data taken in eclipse in 1969 and 1970 showed ion fluxes in a broad range of energies below the charging peak. A typical example of such data is shown in Figure 16. The data is presented in grey scale spectrogram format, a common method of displaying the data concisely. The figure is vertically separated into three components. The top primarily displays magnetic field information, unnecessary for our purposes. The remaining two sections indicate the count rates of electrons and ions in the detector versus time and energy. The horizontal axis defines increasing time, and in this case is labelled with the hours of day 274 of 1970. The vertical axis is associated with the energy of the particles. The minimum (≈ 50 eV) of the energy axis is located between the two sections, and energy increases upward for electrons, and

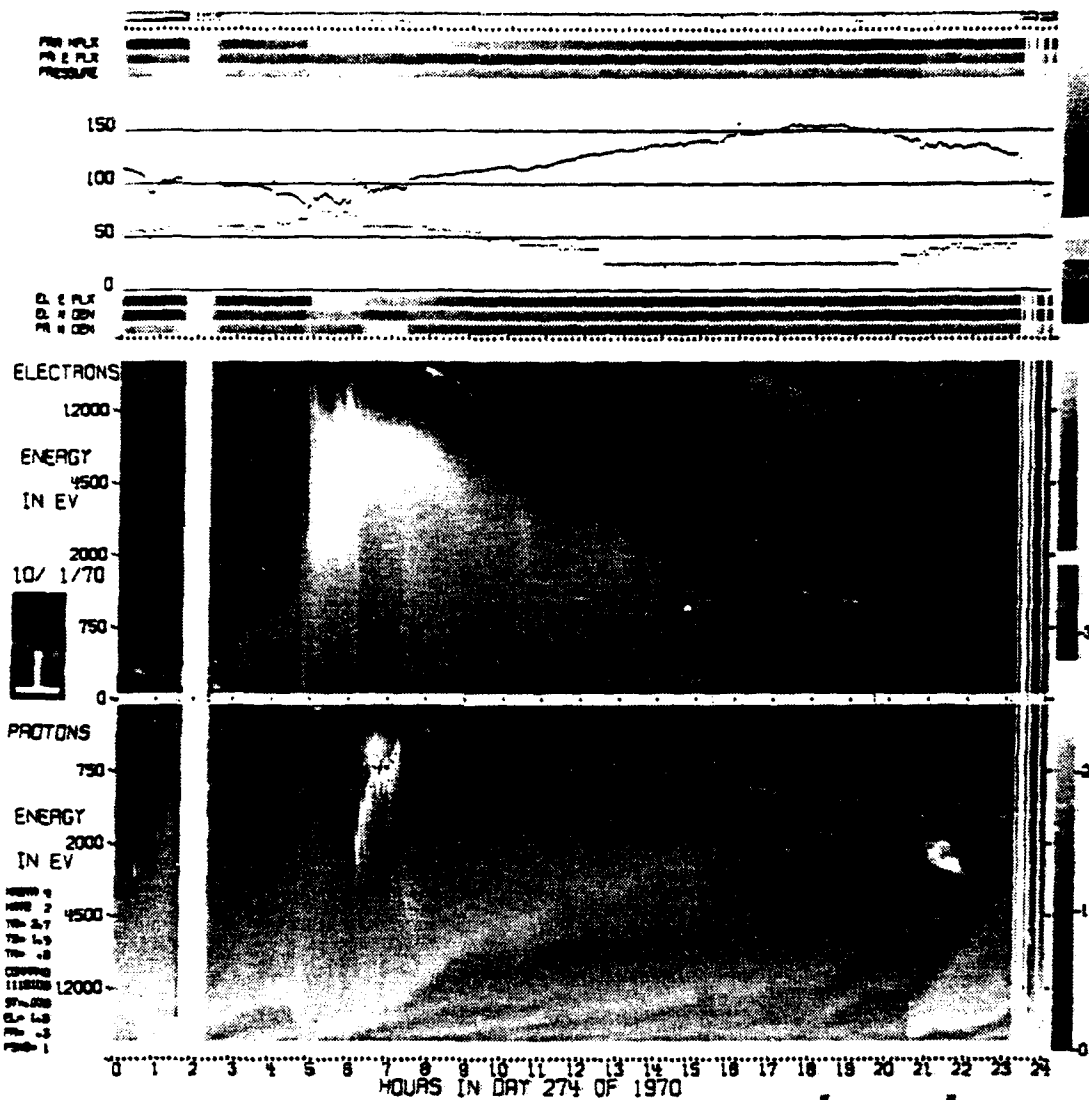


Figure 16. ATS-5, Spectrogram, Day 274 of 1970

downward for ions to a maximum of 50 keV. The magnitude of the detected countrates is indicated by the shading of the figure from black to white, with black corresponding to zero counts, and white with maximum. If the detector is saturated at a certain time in an energy channel, the spectrogram will contain a black spot at that time and energy. A feature such as this can usually be distinguished from a zero count rate because saturation points are normally surrounded by intense count regions, revealed as bright white areas.

The data displayed in Figure 16 are from day 274 of 1970. The satellite enters a region of hot plasma at 0450, as indicated by the increased intensity of high energy (>4500 eV) electrons. The satellite charging peak may be seen as the intense white region in the proton spectrum between 0620 and 0720. From the energy of this region, we can infer a satellite potential of approximately .75-2 kV. The black spots on the peaks are an example of how detector saturation is displayed. The broad spectrum of ions is evident in the energy bands below the charging peak as the grey area that clearly extends from 1 kV to about 300 V, and may even continue to lesser energies. These particles did not appear during every charging event, so the source was difficult to determine and no complete explanation was put forward.

2. ATS-6

ATS-6 also showed evidence of non-ambient source contamination of the ion data. Secondary or shadow peaks were observed at energies below the inferred satellite potential. An example of such data is illustrated in Figure 17. This figure is a grey scale spectrogram similar to the one shown in Figure 16. The data presented are from the North-South detector on ATS-6 on day 243 of 1974.

This plot displays two phenomena. The first is the ion peaks, which are clearly presented elsewhere {Ref. 2}. These ions were denoted "spacecraft generated ions". The second is an apparently analagous phenomenon in the electron spectrum. These observations are the so-called "Minnesota spots". In addition to the electron and ion spectra, this figure displays the detector pitch angle in the top section, which is related to the rotation angle.

The spots are seen in the electron spectrum between 100 and 300 eV as intense white points that appear to form triangle shapes. If one compares the periodicity of the electron triangles with the detector look angle periodicity, a direct correspondence is evident. As the top of the spacecraft, where the detectors are located, was in shadow at this time, the source electrons were determined to be secondaries from the surface of the vehicle. These electrons had been emitted from a surface differentially charged with respect to the detectors, and thus the

200-38E-2.5 DBP=1.2 DBS=0.080 S1PE= 3 PSN= 2 NS= 1.0 PPI=360 3600 CCM= 124373210 SR= -20 LNG=265 - 90

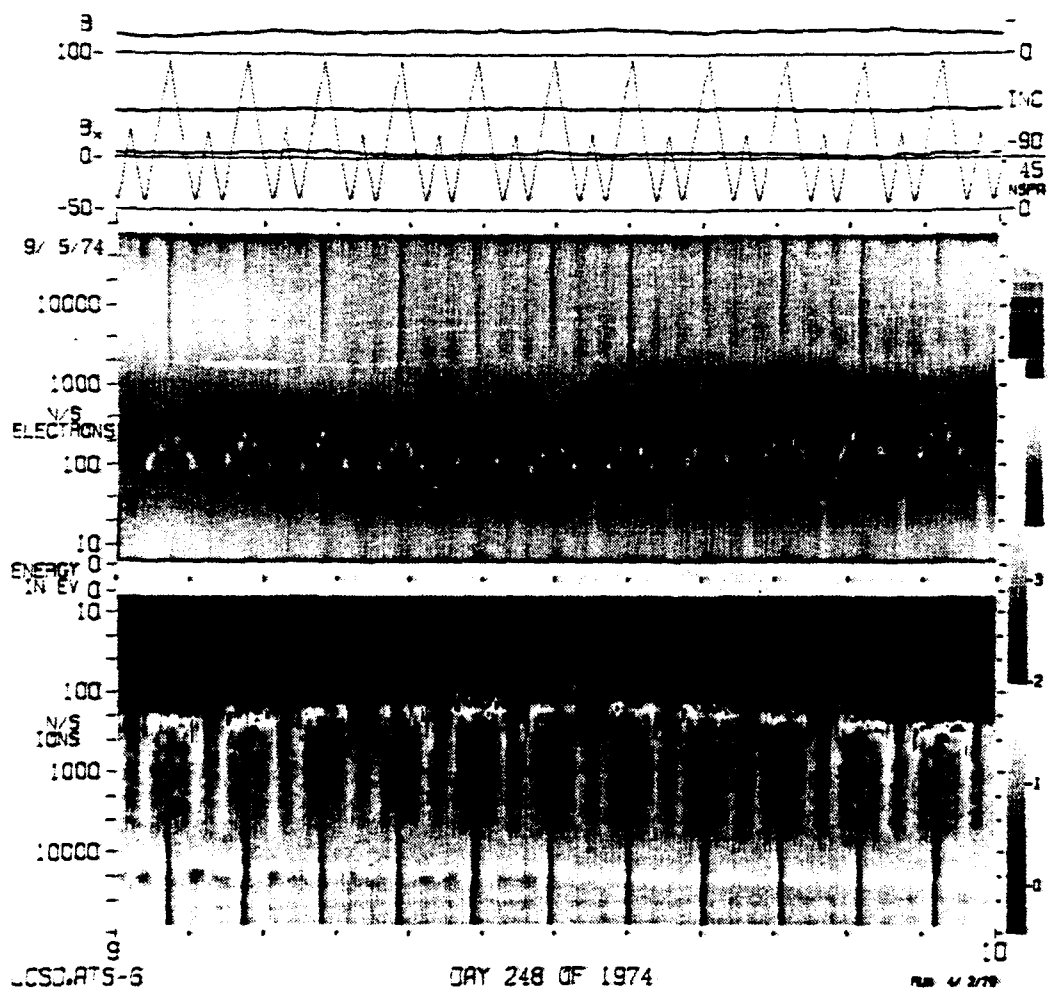


Figure 17. ATS-6, Spectrogram, Day 248 of 1974 {Ref.2}

charged with respect to the detectors, and thus the distribution had been accelerated by a potential drop ϕ . The source of the flux was eventually determined to be secondary emissions from the University of Minnesota detectors also located on the satellite measurements box. {Ref. 2}

3. ISEE

Negative charging events on the ISEE satellites were relatively rare, as the satellites were specifically designed to avoid the problem of spacecraft charging. ISEE-1 did, however, charge to significant negative levels on a few occasions. During one such event, analysis of the ion mass composition revealed some interesting features. Figure 18 is a presentation of the ISEE-1 mass spectrometer reading from March 17, 1973. The vertical axis is a count rate, and the horizontal axis is the applicable mass channel. The mass channel is related to the atomic mass by,

$$(2-1) \quad \text{AMU} = \frac{3615}{\text{Mass Channel}^{2.0539}}$$

Thus, mass channel 54 corresponds to H^+ , 15 to N^+ , and 14 to O^+ . {Ref. 10}

At 0633 UT (Universal Time), the instrument responded with a broad peak in the high Atomic Mass Unit (AMU=30-100) channels. This peak had a maximum in channel 10 corresponding to 32 AMU. There was also a peak at channel 54, H^+ . The normal value of the ambient atomic

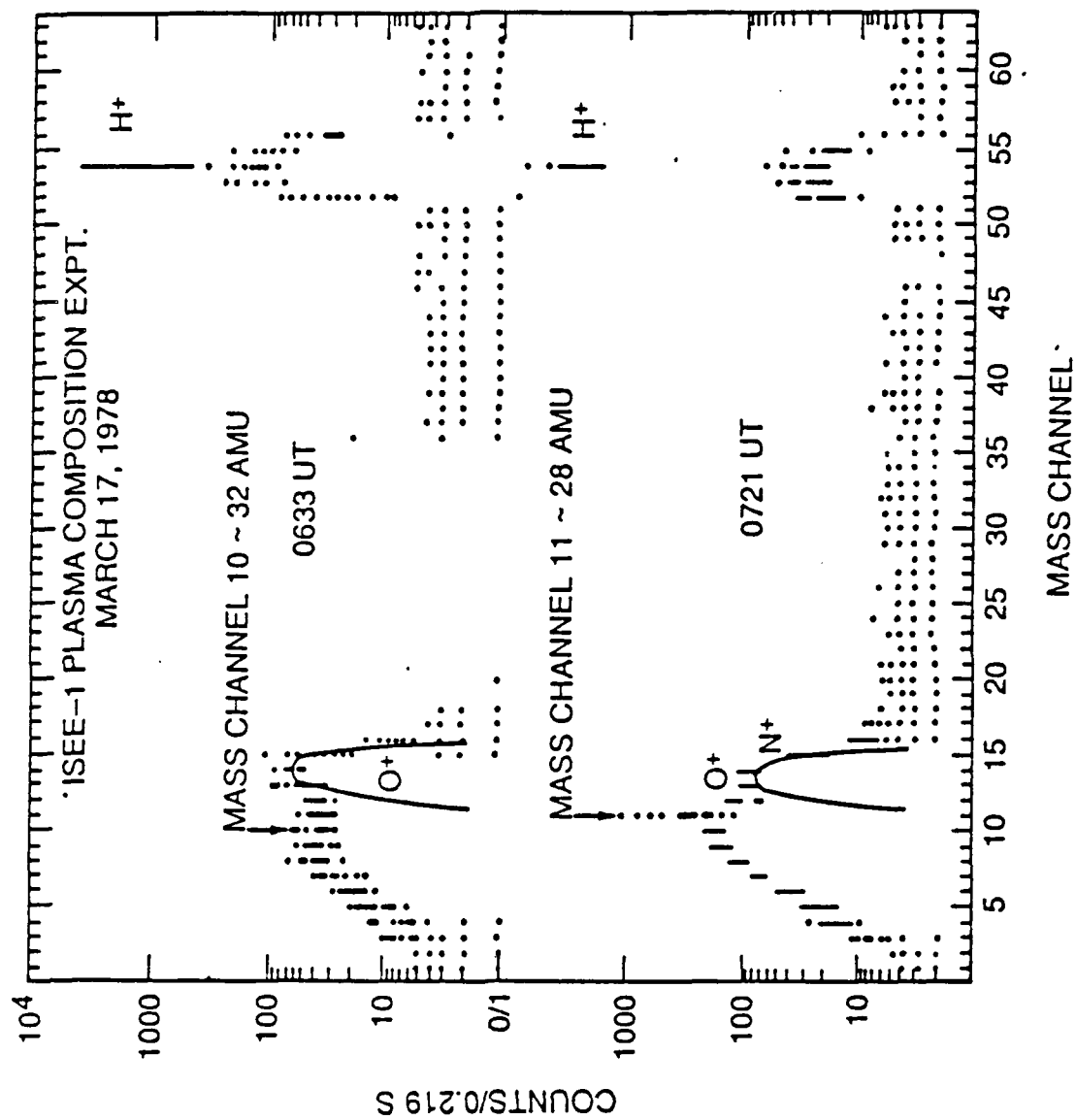


Figure 18. ISEE-1, Mass Spectrometer, March 17, 1978
{Ref. 10}

oxygen is indicated by the solid black line under the peak. The data from 0721 UT are quite similar, except that at this point the maximum has shifted to channel 11, 28 AMU. Again, this is larger than the indicated ambient oxygen. At the time these observations were first made it was concluded that these molecules were probably hydrocarbons and other outgassing products. In light of spacecraft surface sputtering, however, one may postulate a different flux source. That is, these particles are ions emitted from the spacecraft surface. Since the surface is primarily silicon dioxide (SiO_2), the ejected particles would largely be Si, O, and O_2 . The masses of these are 28, 16, and 32 AMU respectively, numbers which would fit nicely into the observed data. {Ref.10}

B. P78-2 (SCATHA)

Observations of spacecraft generated ions are presented for five days. The first two are for eclipse charging events in 1979, the second pair are for ion gun induced charging, and the last is for eclipse charging in 1981.

1. Day 83 of 1979

This first eclipse event illustrates the triangle peak and its associated angular dependence. Figure 19 is the grey scale spectrogram for a one hour period of day 83 of 1979. This is a composite of the electrons from the H1 detector, and the ions from all three detectors. Each of the ion displays has zero energy at the top and increases

energy downward. The electron presentation is reversed, with low energies at the bottom, increasing upward. Between 1740 and 1820, the triangle structures can be seen in the Lo detector data. From the Hi detector data, it can be seen that the spacecraft charges negatively to about 200 V at 1750, decreases to 100 V at 1815, and increases rapidly to 300 V at 1825. Multiple shadow peaks are visible during this period in both the Hi and Fix detector data.

Figure 20 is a plot of the log ion distribution function (phase space density) versus energy for the Hi detector. The spacecraft is charged to -250 V, in eclipse, as indicated by the peak in phase space density (f) at 250 eV. The shadow peak is the secondary peak at 78 eV. At this time, the detector is parked at 92 degrees, approximately parallel to the spacecraft spin axis.

Figure 21 is a diagram of the spacecraft potential, triangle peak energy, and Lo detector look angle versus time. The energy of the peak varies directly with the look angle, with the energy minimum occurring at the angle maximum, that is, looking down and away from the spacecraft (where it approaches closest to the spacecraft surface). The shadow peak energy maintains a relatively constant ratio with satellite potential. In this case, E_p/E_t is between 6 and 7, where E_p is the satellite potential, and E_t is the triangle peak minimum energy. This is significant, as we

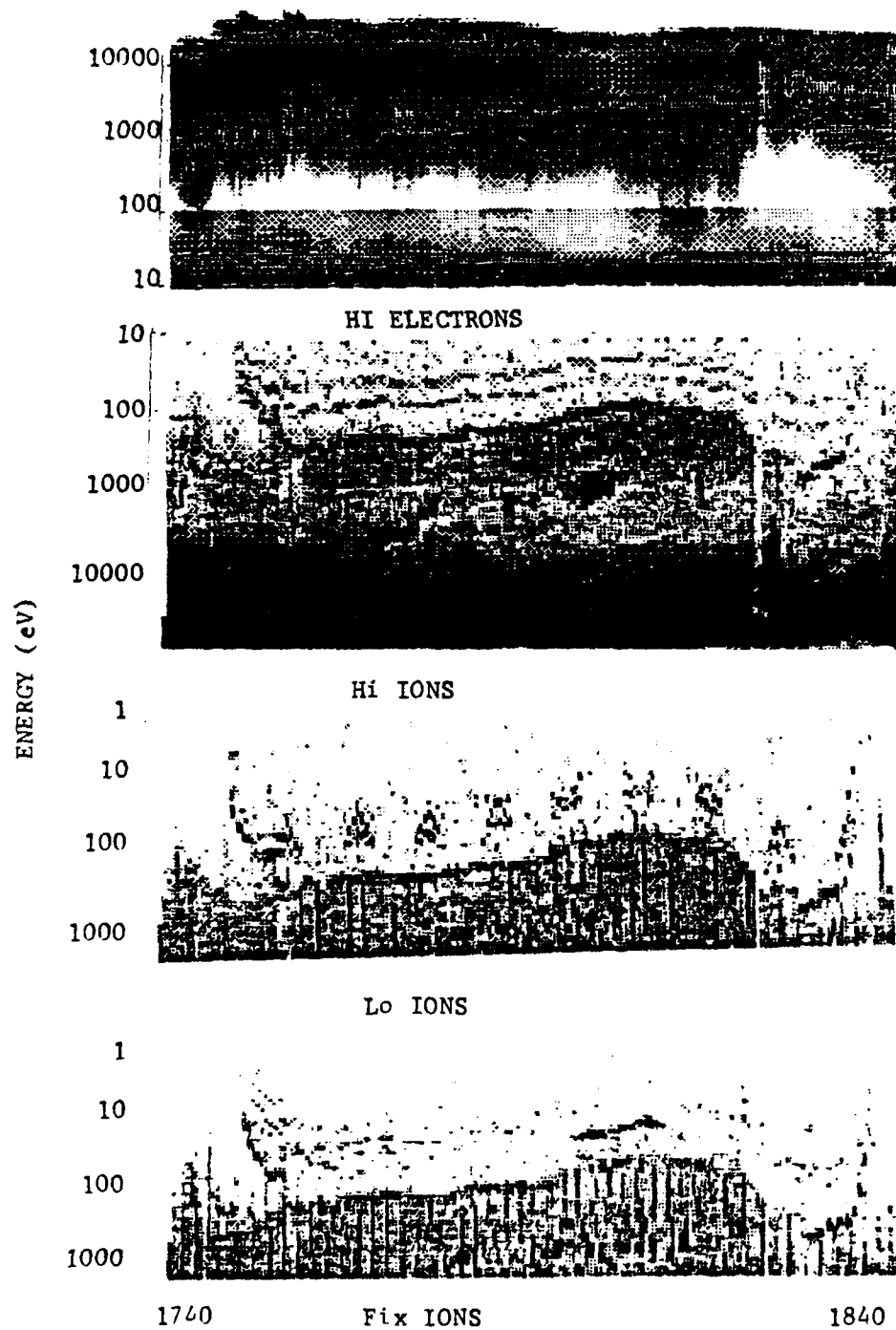


Figure 19. SCATHA, Spectrogram, Day 83 of 1979

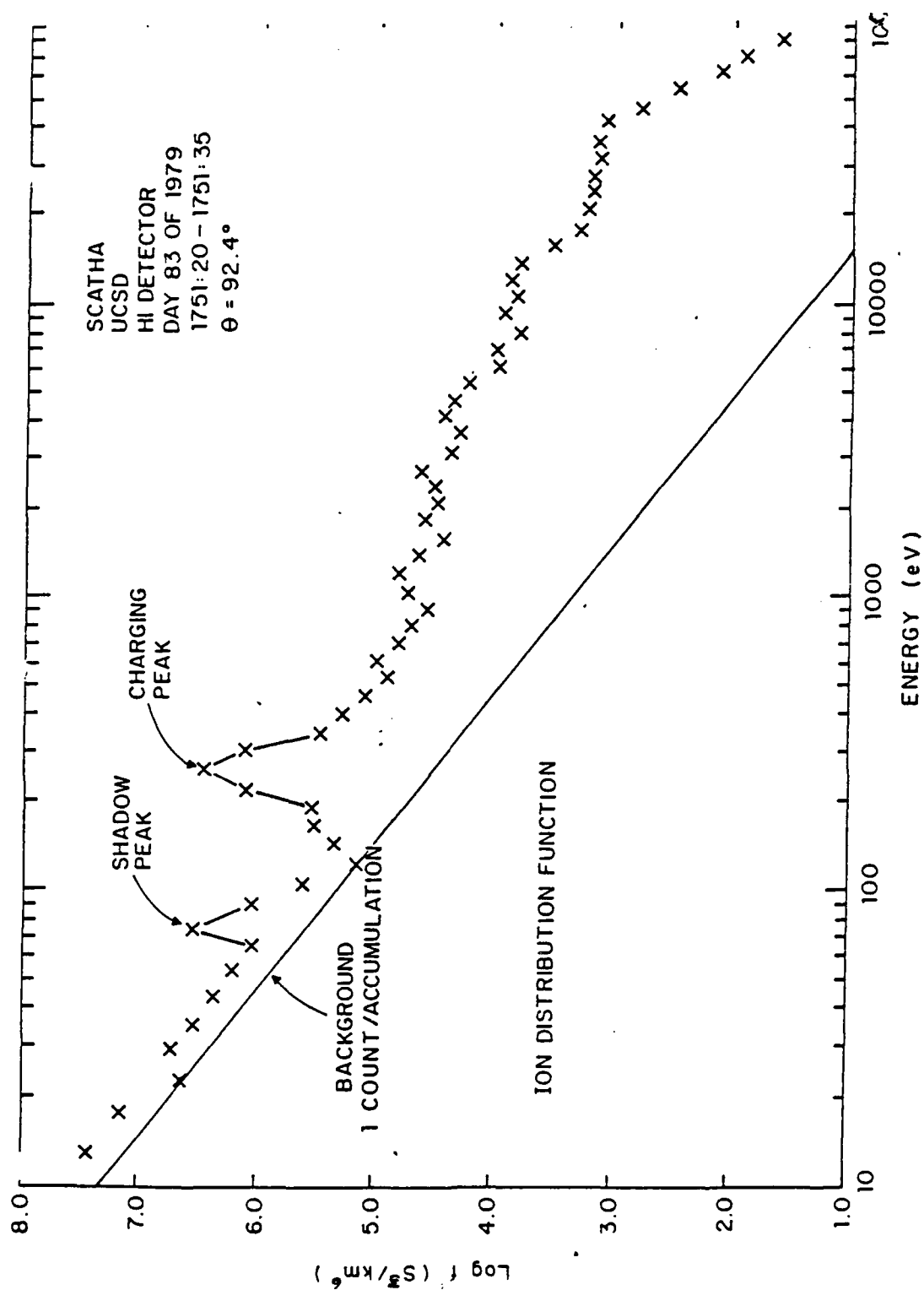


Figure 20. Day 83 of 1979, Ion Distribution Function

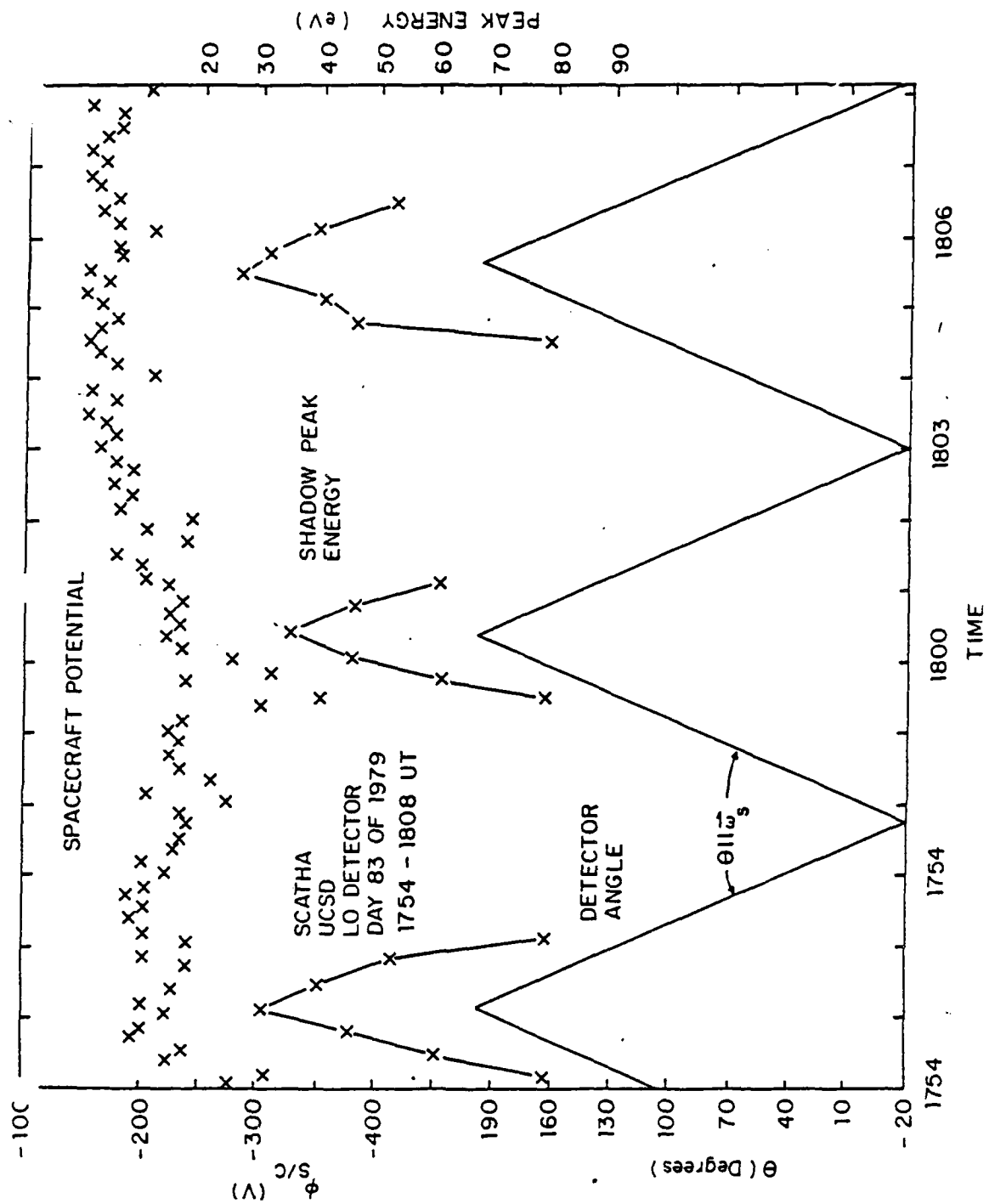


Figure 21. Day 83 of 1979, Vehicle Potential, Triangle Peak Energy, and Look Angle vs. Time

would expect a differentially charged surface to maintain a constant ratio over time with the satellite mainframe.

2. Day 86 of 1979

The second eclipse charging event, day 86, is similar to that of day 83. Figure 22 is a grey scale spectrogram of the ion data for a one hour period on day 86 of 1979. The triangle structures are again visible from 1645 to 1740 in the Lo detector display. From the Hi data we see that charging begins at approximately 1640, and the potential varies widely throughout the period. A fluctuation in the satellite potential due to a change in the electron Alfvén boundary is seen at 1705. The spacecraft achieves a maximum potential of -600 V at 1725. During the period, a shadow peak is clearly visible at energies lower than the charging peak in both the Hi and Fik detector data.

Figure 23 plots the ion distribution from the Hi detector. The satellite potential is -340 V as indicated by the charging peak. There is a well defined shadow peak at 100 eV. In addition, there are various other small peaks below the charging peak that may indicate other shadow peaks. Frequently, other shadow peaks appear in the spectrograms, maintaining a constant separation ratio between each other, and varying as the main peak varies. The detector is again parked parallel to the spacecraft spin axis.

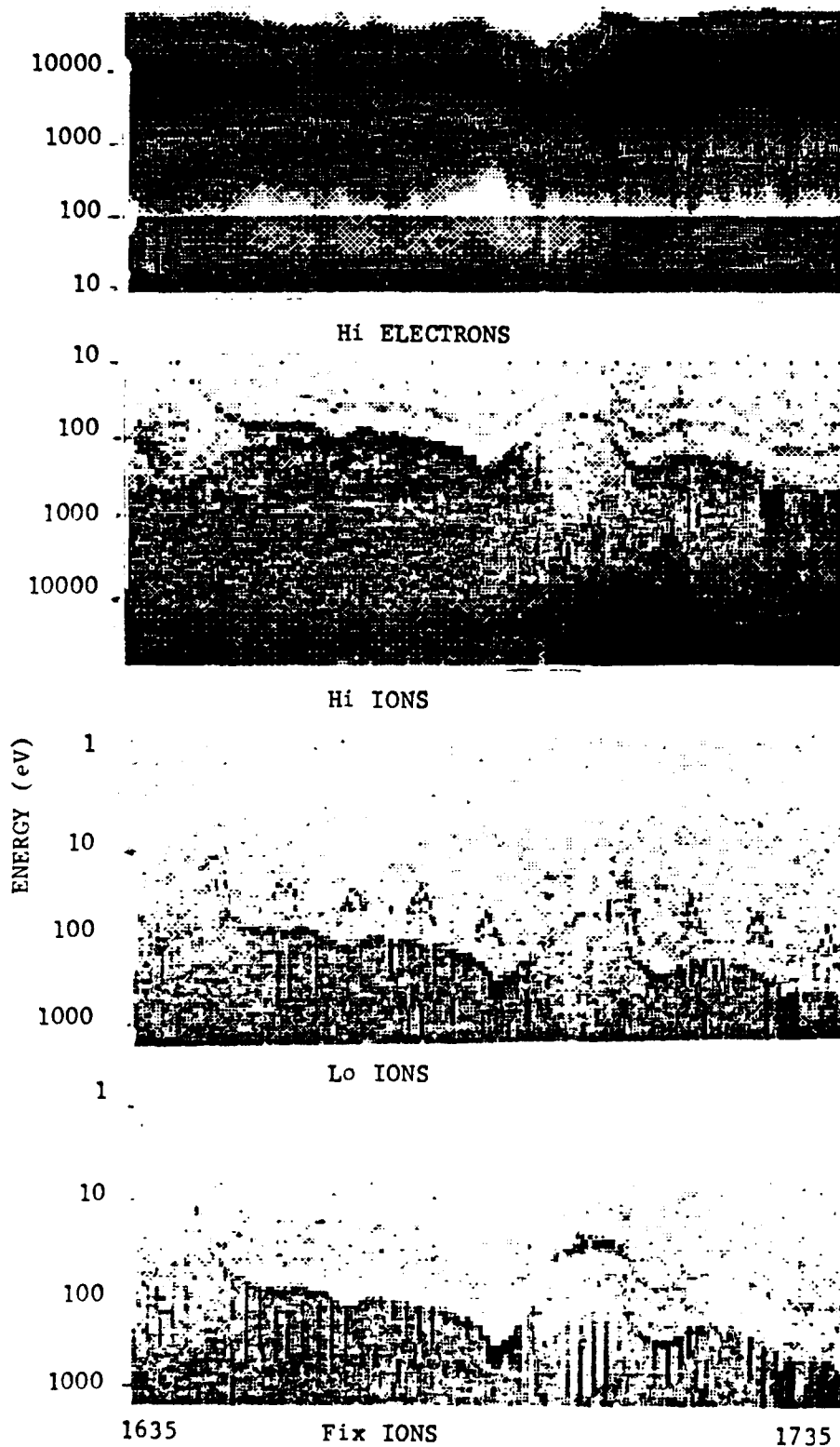


Figure 22. SCATHA, Spectrogram, Day 86 of 1979

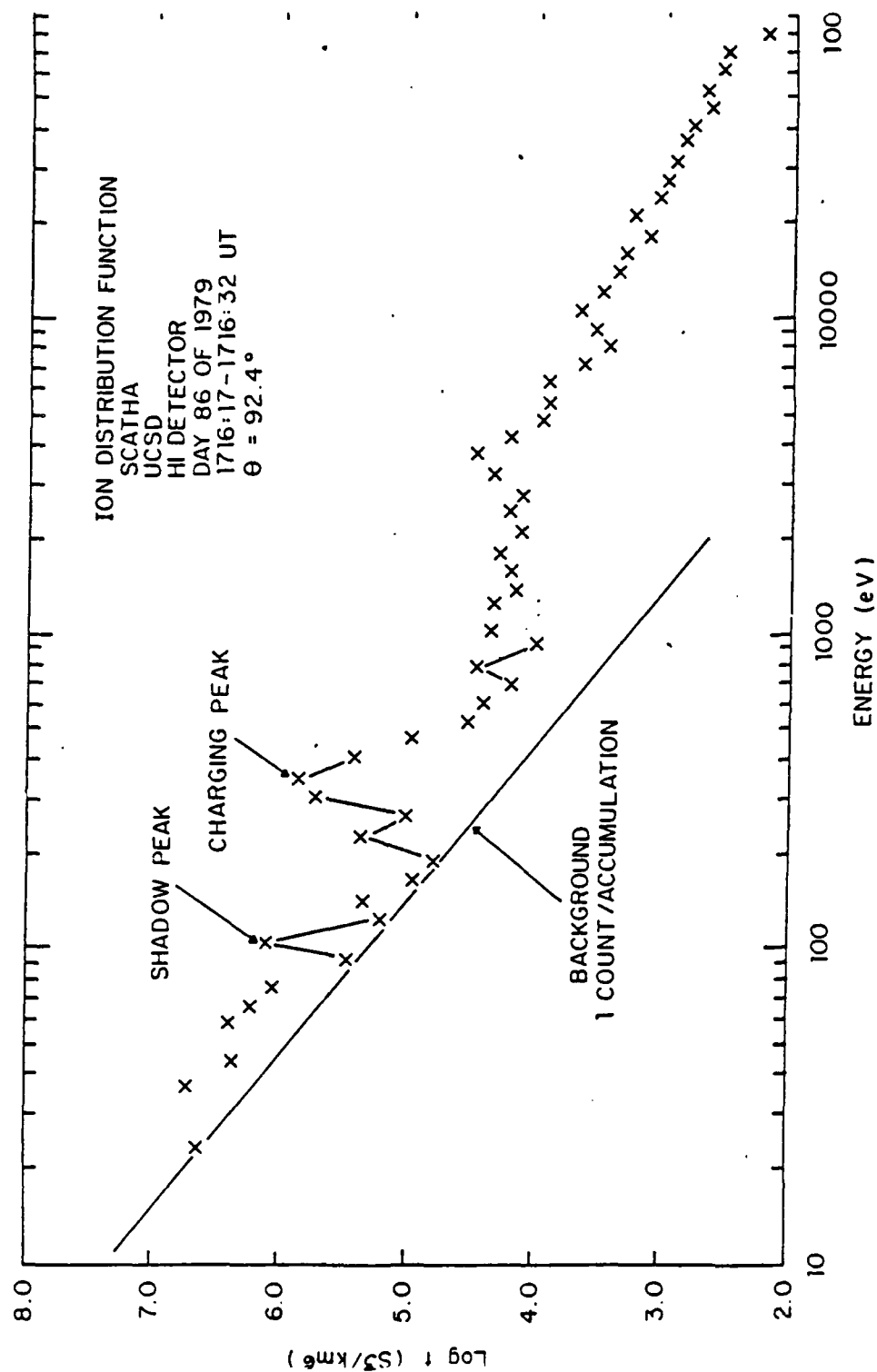


Figure 23. Day 86 of 1979, Ion Distribution Function

The strong dependence between the triangle peak minimum energy and spacecraft potential is illustrated by Figure 24 for this more variable day. It is clear that the minimum energy of the triangle peak increases with the increasingly negative vehicle potential. The ratio, E_p/E_t , is maintained between 6 and 6.5. Again, the energy of the shadow peak varies directly with the detector angle, achieving minimum energy at the detectors maximum angular extent. The shadow peaks usually lose their definition below 110 degrees.

These two examples illustrate typical observations during eclipse passages for which negative charging occurred. By comparison with ATS-6, we would expect similar observations during daylight negative charging events. ATS-6, however, was stabilized and had its large solar array to provide a shadowed area which would simulate an eclipse. SCATHA had no such array, and in addition was spinning so that no area was shadowed long enough to charge to a high level. Observations of daylight charging showed that the spacecraft potential was highly spin modulated, making it difficult to use these data for this project. However, induced charging events with the ion gun provide an additional range of daylight data. Two examples of such experiments are presented.

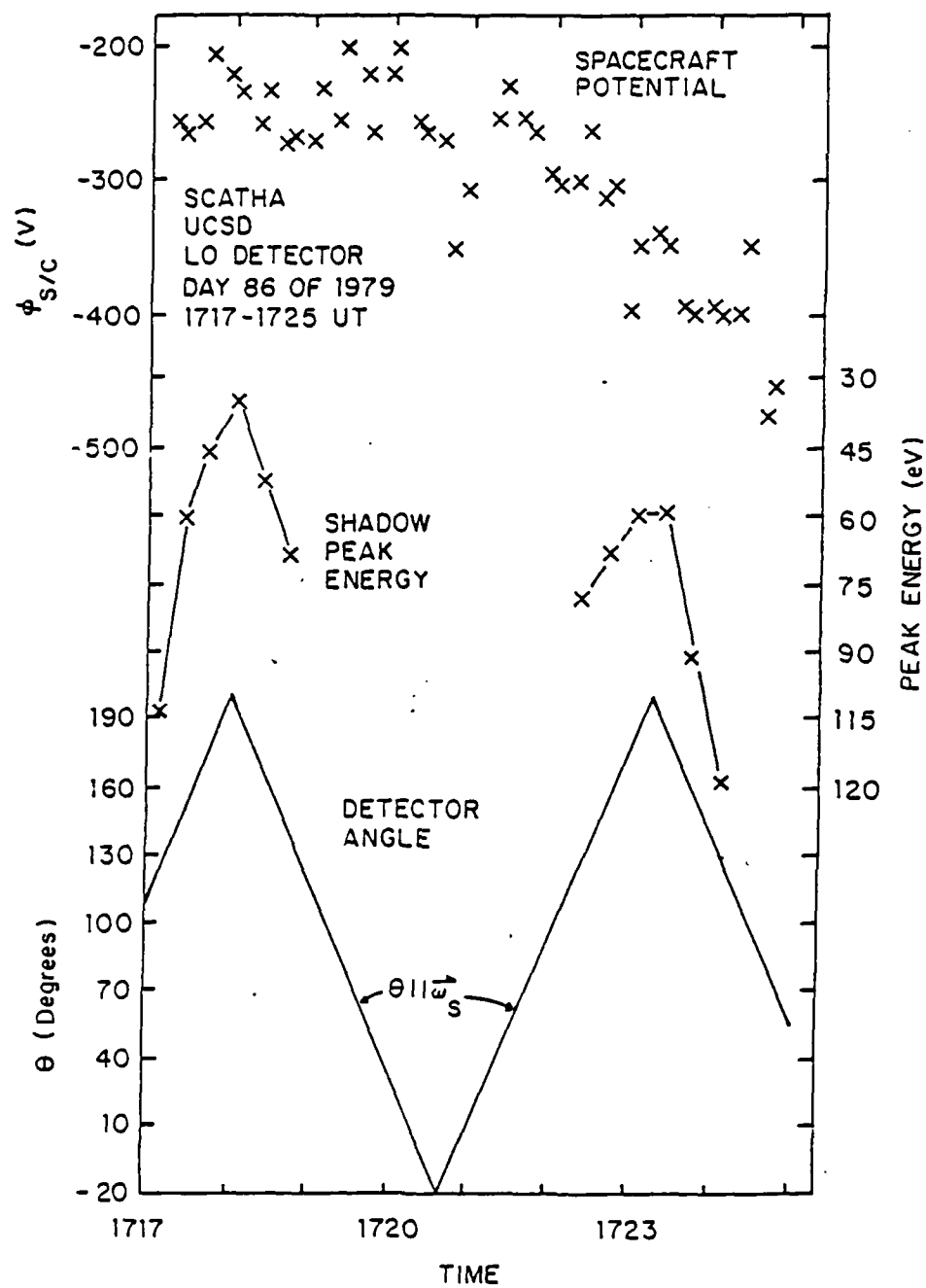


Figure 24. Day 86 of 1979, Vehicle Potential, Triangle Peak Energy, and Look Angle vs. Time

3. Day 94 of 1979

The first example of ion gun induced charging is day 94 of 1979. The ion gun was in operation at 1 kV and 1 mA. Figure 25 is the grey scale spectrogram for a 1 hour period from that day. The data presented are from two ion detectors, with the Lo detector in the upper diagram, and the Fix in the lower. The ion gun is turned on at approximately 1405 and the spacecraft charges promptly to a final value of -60 V. Shadow peaks occur at 11 and 20 eV in the Lo detector between 1420 and 1430, and between 1440 and 1455.

A curious feature is the appearance of twin shadow peaks in the Lo data at 1440, with bands between in which no ions were detected. When this phenomena began, the detector had just been parked at an angle of 20 degrees to the spacecraft spin axis, away from the satellite body. The detector had previously been scanning. When the data printouts are examined, three bands clearly emerge; one at 11 eV, another at 22 eV, and the last at 30 eV. We may infer that certain energies, or trajectories, do not reach the detector at that angle. These events indicate something about the location of the emitting surfaces. From the striations in the Lo data, we would expect non-emitting or non-differentially charged surfaces to be sandwiched between emitting regions, thus giving the dark regions where no ions are detected. Importantly, the Hi detector is viewing in a

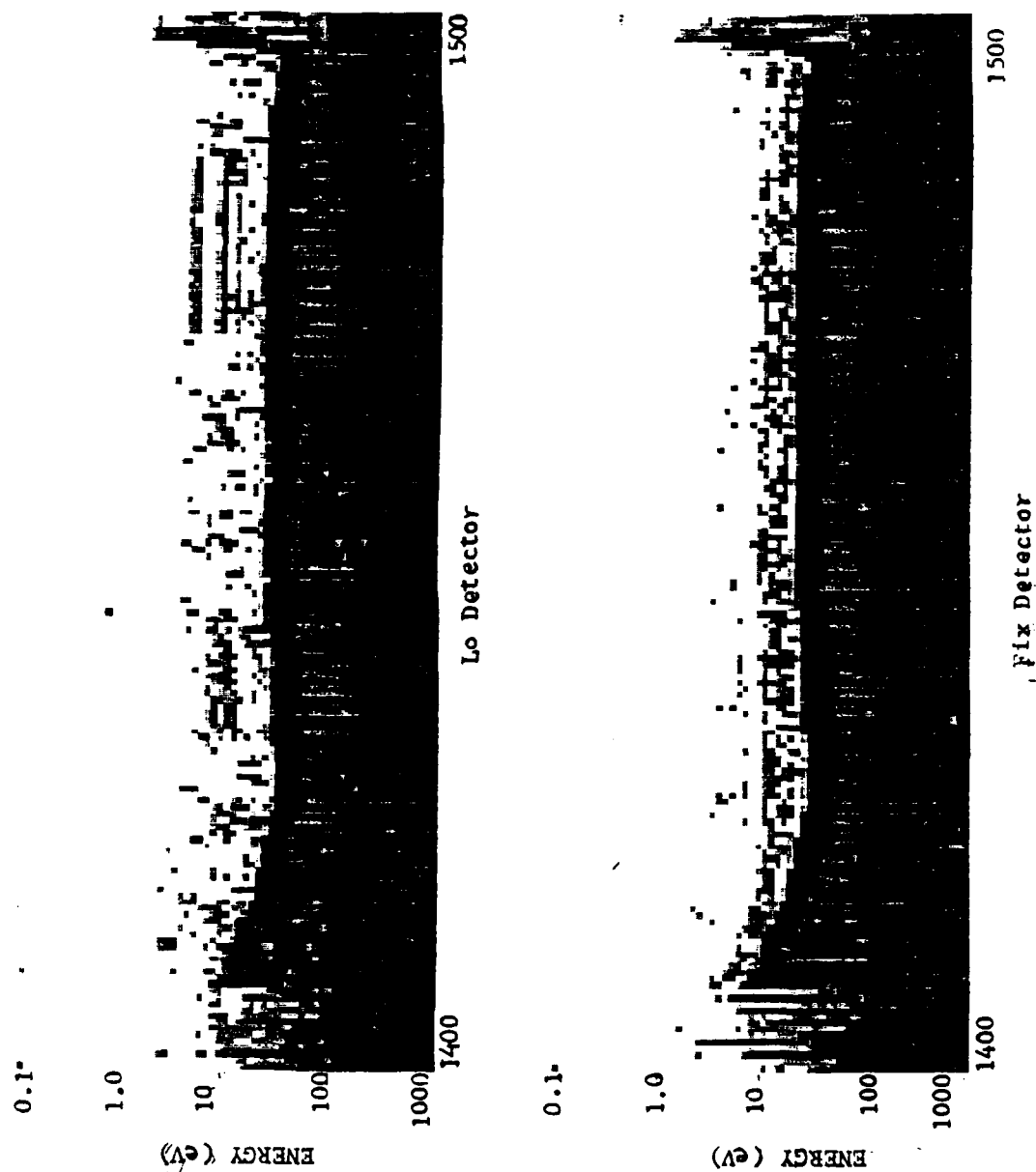


Figure 25. SCATHA, Spectrogram, Day 94 of 1979

similar direction at this time, and gives a similar response. The Fix detector, viewing 70 degrees from the Lo and Hi, reports a completely different environment. It does, however, show a similarity in that a large energy gap exists. This indicates mixed differentially and non-differentially charged surfaces as above.

4. Day 200 of 1979

Our fourth example is during an ion gun operation at 1 kV, 1 mA. Figure 26 is a grey scale spectrogram for a two hour timeframe. The data are taken from the Hi detector. In this figure, the spacecraft is charged to approximately -700 V, except during the two five minute periods when the ion gun was in "trickle" mode. Trickle mode is defined as the gun in operation with the accelerating voltage off, but current still applied to the diode. Thus, the generated ions leak out at low energies. Triangle peaks are clearly visible in the ion display. This day is one of the few in which these peaks become evident in the Hi detector. The ratio, E_p/E_e , for these figures is in the 9-10 range, indicating that the Hi detector is looking at an emission point different from that seen by the Lo detector on days 83 and 86 (or different processes are at work).

Figure 27 shows the distribution functions when the Lo and Fixed detectors are looking approximately parallel, radially away from the spacecraft. The Hi detector is near its maximum rotational angle. The satellite potential is

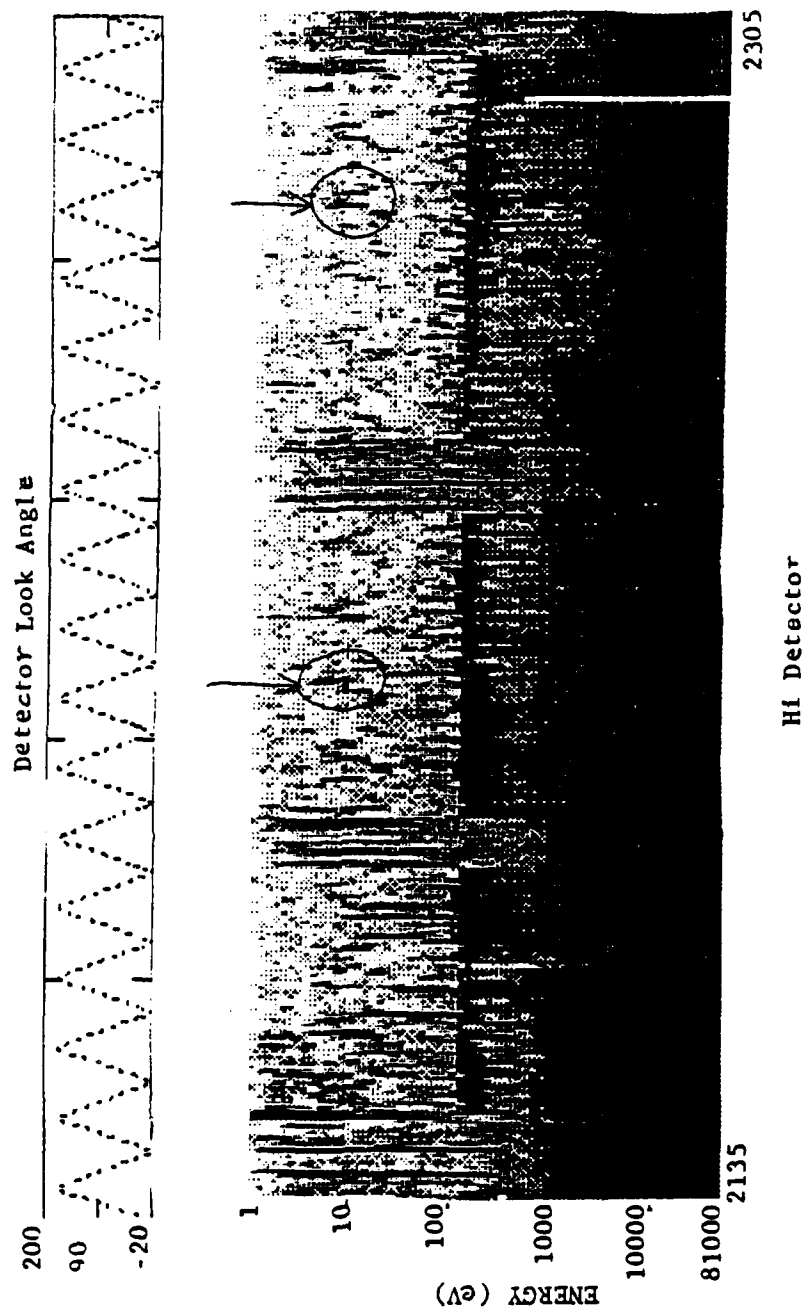


Figure 26. SCATHA, Spectrogram, Day 200 of 1979

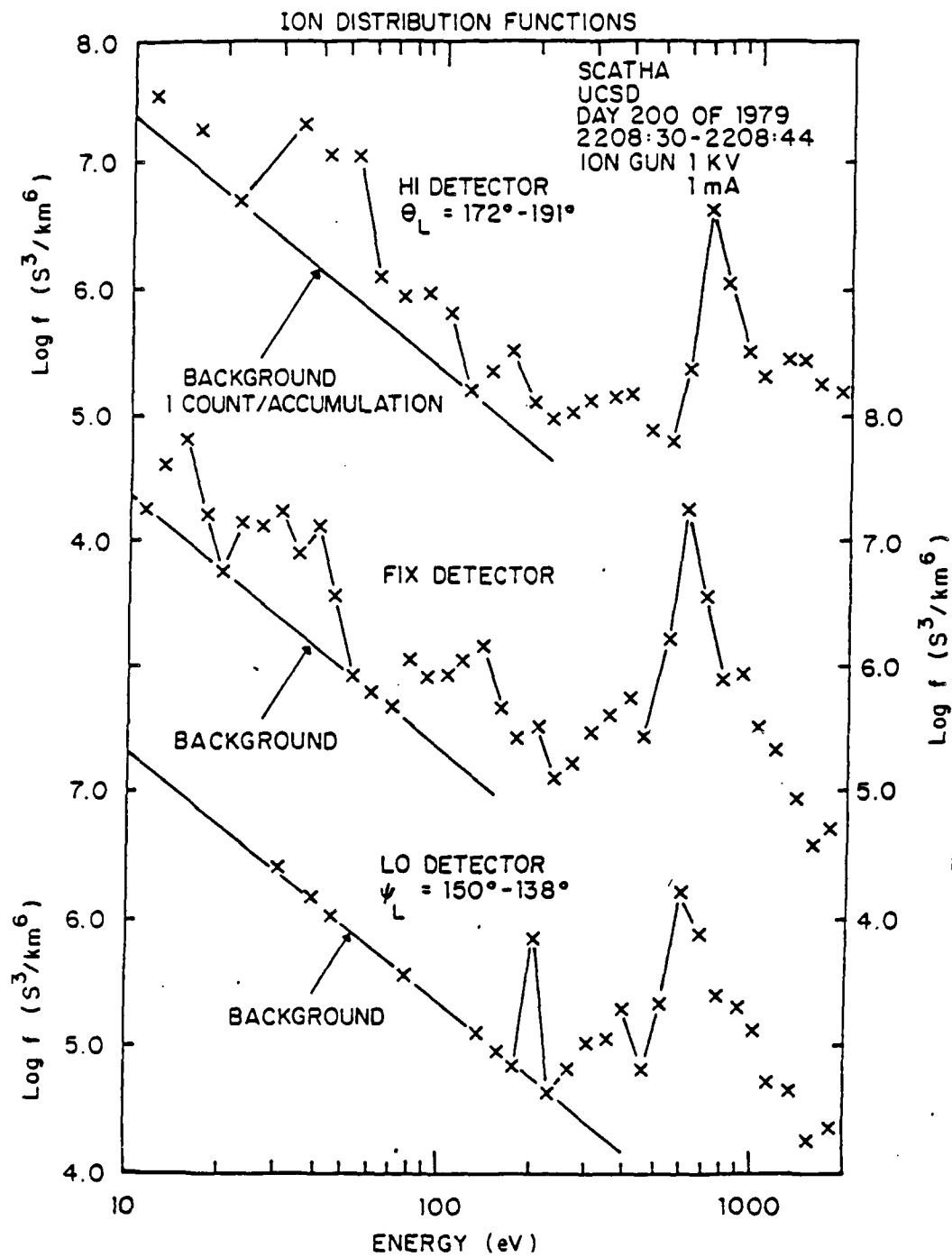


Figure 27. Day 200 of 1979, Ion Distribution Functions

approximately -700 V. The Hi and Fix detectors exhibit a broad array of low energy ions, but such a spectrum is not evident in the Lo detector. The Lo detector does show a sharply defined shadow peak. The data have a similar form throughout this period, with subtle variations in the amplitude and energy of the diffuse spectrum, particularly with angle.

5. Day 92 of 1981

Figure 28 is the grey scale spectrogram from a 1981 eclipse charging event. The figure displays 4 hours of data from the Hi detector for both ions and electrons. The eclipse charging event is visible in the illustration between 0810 and 0945 UT, with potentials varying from -100 to -400 V. During this period, a definite shadow peak is also evident, in the -60 to -150 V region.

Figure 29 is a plot of the ion distribution functions for day 92. The log distribution function has a charging peak at 0820 at 90 eV with a value of 6.07. This value is comparable to those on days 83 and 86 of 1979. Thus the detected countrates are as high as those encountered early in the mission. This indicates that the source of the detected particles is not dependent on satellite lifetime, and hence that outgassing is not a major contributor to the observed satellite generated ion phenomena.

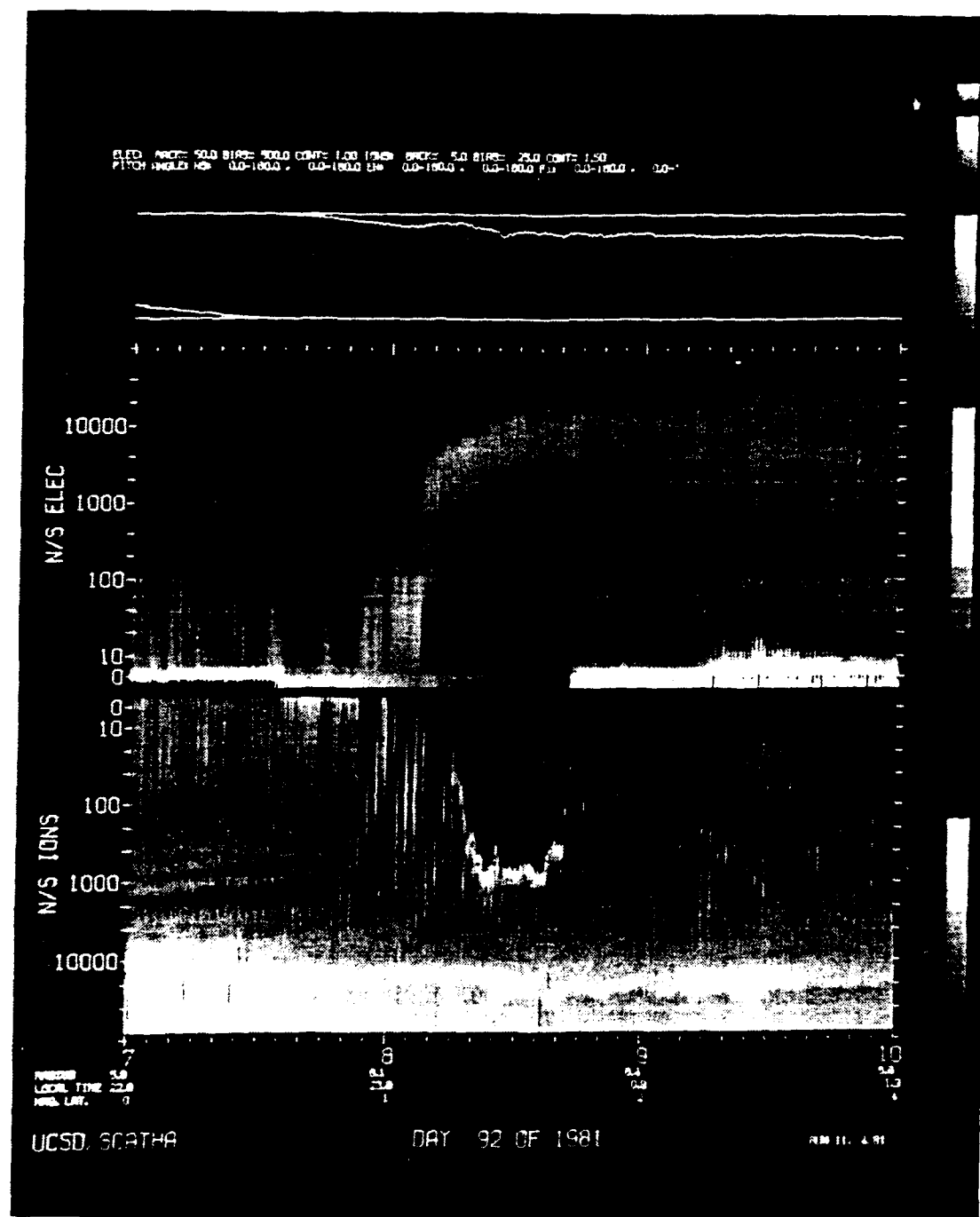


Figure 28. SCATHA, Spectrogram, Day 92 of 1981

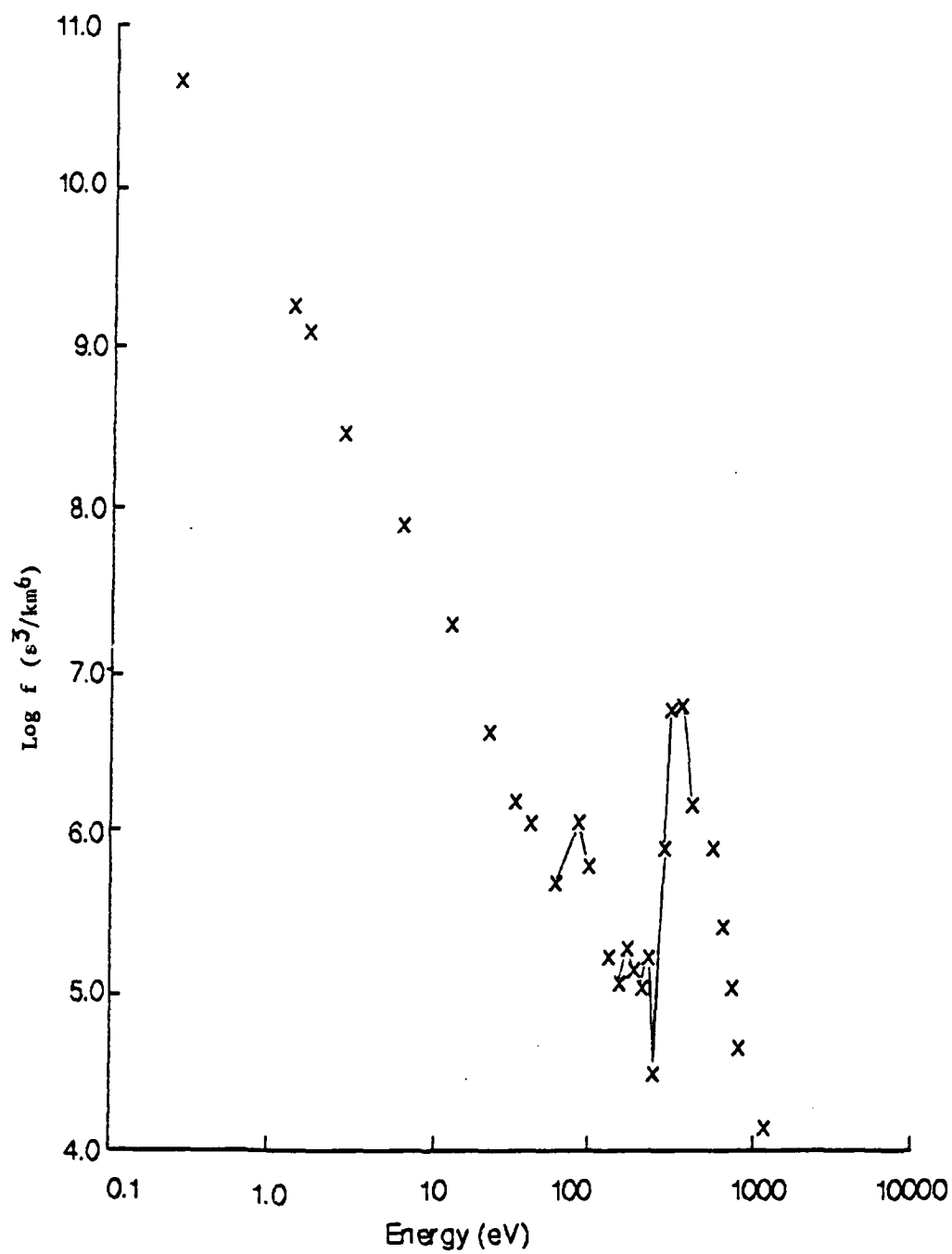


Figure 29. Day 92 of 1981, Ion Distribution Function

III. DISCUSSION

A. POSSIBLE ION SOURCES

The ion source must be able to explain three different phenomena, the triangle peaks, the shadow or mirror peak, and the diffuse spectrum. The prime feature that the observations have in common is the appearance of the subject ions at energies below that provided by the spacecraft potential. Thus, they must be generated in regions near the spacecraft where they do not experience the full plasma-satellite potential. There are two prime candidates for the source, outgassing and sputtering. Outgassing is the emission from the satellite of contaminant molecules and atoms with energies near the temperature of the satellite. These are primarily trapped hydrocarbons and other atmospheric molecules. The outgassing rate may be increased by the inclusion of efflux from the attitude control jets, and the ion beam system. Sputtering is the emission of charged and neutral atoms from the satellite surface due to ion bombardment, and its theory has been described previously. A qualitative discussion of both possibilities follows, followed by a numerical calculation of the number of ions that would reach the detectors due to Sigmund-Thompson sputtering from differentially charged surfaces.

1. Outgassing

As the contaminant particles leave the spacecraft they are subject to ionization from photons, and collisions with ambient ions and electrons. As the molecules are ionized at various distances from the spacecraft they will return in a broad range of energies. This is a possible explanation of the observed diffuse spectrum. The question is then, how many particles outgas, and what percentage of these are ionized? The problem of outgassing and the outgassing yield has been studied previously {Refs. 32,33}. The dominant mechanism for the ionization of the outgassing molecules has been determined in sunlight to be photoionization, and in eclipse to be collision with electrons. The electron ionization rate is approximately two orders of magnitude less than the photoionization rate. In eclipse, however, the photoionization rate goes to zero and the electron collisions become dominant. In all probability, the electron ionization rate will increase slightly in eclipse, as the electron density will increase due to space charge effects. The ionization rate, however, will not exceed that of the photoionization. {Refs. 2,32}

The distance within which the ions may be returned to the spacecraft will be the width of the surrounding plasma sheath. The sheath distance at geosynchronous orbit is approximately 100 m. With this information and the ionization rates above, it may be shown that, at a maximum,

approximately .02% of outgassing silicon atoms will be ionized. In a central force field, with conservation of angular momentum and energy, calculations reveal that all the particles ionized in the sheath will be returned to the spacecraft. The final result then, is that .02% of the outgassing molecules will be reattracted to the satellite. {Ref. 32}

When the spacecraft is first launched, the ionized outgassing flux may be sufficient to provide a significant number of particles at the detectors. Outgassing, however, is an extremely time dependent phenomenon. Once the particles leave there is no way to replenish them, so the outgassing rate must decrease with time. Various experimental data have placed the outgassing as proportional to t^{-n} , where n varies from 0.8 to 1.6, or as proportional to $\exp(-t/41.6)$, with t in days {Refs. 32,33}. The longest e-folding time then would be 41.6 days. Even this would lead to a decrease in the outgassing flux by three orders of magnitude over the period of a year. As noted in day 92 of 1981 above, however, the shadow peaks have not diminished over time in any significant way. This leads to the conclusion that the outgassing flux may be a contributor, but is not the prime source of the ions.

What effect do the thrusters and ion gun have on this conclusion? An experiment was performed aboard the SCATHA spacecraft to measure the contamination (impurities

mixed with the hydrazine fuel) on the satellite due to the thruster operation. Two sensors were placed on the satellite, one in the bellyband, and one on the forward end. The sensors were capable of detecting 5 ng/cm² particle deposition and a current as low as 10^{-12} A. The thrusters were located on the aft end of the vehicle, and were fired once per week during the bulk of the flight time to correct for precession. The results of the experiment indicated that no measurable flux of thruster contaminants was returned to the spacecraft. {Ref.34}

The ion gun is also an unlikely source of contaminants to the detectors. As noted above, it is located on the aft end of the spacecraft and directed away from it. During most normal modes of operation, the energy and angular momentum of the exiting particles would prohibit them from reaching the detectors. There is evidence that some ions are returned to the detectors, but they are observed at energies greater than the satellite potential {Ref. 35}. There is a possibility that ions emitted during trickle mode, at low energies, may be reattracted, and contribute to the flux observed at the detectors. This is probably only a small intermittent component, as the operation of the ion gun in the above mode was not continuous or frequent. Thus, the outgassing flux is primarily composed of the emitted contaminants.

With just the emissions of the contaminant flux, it is still numerically conceivable that the outgassing flux could produce sufficient particles to account for the observations. However, it is certain that the outgassing flux does decrease over time, and this is not observed in the data. Additionally, it is hard to conceive that the satellite potentials are such that the randomly ionized flux is focussed into a beam one energy channel wide at the detector. Moreover, it is unreasonable that the focussing should be such that a small change in the detector look angle yields such a definite change in the observed energy, as in the phenomena of the triangle peaks. In sum then, it does not appear likely that ionization of outgas products is the source of the observed flux.

2. Sputtering

When this work began, it was initially assumed that the ion source was outgassing. As the work progressed, it became apparent that there were serious drawbacks in this assumption, as noted above. While searching for alternatives, the advantages of sputtering as a source became clear. First, besides a small dose dependence, there is no reason for the sputtering yield to decay over time. This attribute was very important in light of the significant shadow peaks observed in 1981. Second, the emission of sputtered particles from a differentially charged surface would lead to observed beams at the

detectors. As the particles left the surface with their various initial angles and energies, they would be accelerated by the existing electric field into an almost parabolic orbit. Thus, for each energy, only particles following specific trajectories would reach the detector, limiting observation angles. Since the detector energy channels have a resolution of 20 %, the bandwidth of the channels increases with energy. Therefore, a peak which would appear broad when distributed over the lower energy channels, can be compressed into a narrow peak in the high channels. The low and high energy channels of the SCATHA detectors are listed in Table 8. The similarity between the observed data and the data from the Minnesota spots also became evident. It seemed reasonable that if such a process could occur for secondary electrons, it could occur for what were essentially "secondary" ions. Additionally, the sputtering theory could explain the diffuse spectrum as the receipt of particles sputtered from a non differentially charged surface. Without the charging, the ions are not focussed into the higher channels, and can appear as a broad low energy distribution. The third phenomena, the shadow peak, can be described by two mechanisms. The first is a motionless detector, not scanning in angle, and observing one trajectory, i.e., one energy. Alternatively, the detector could be scanning laterally across an emitted beam,

as opposed to vertically, and thus be picking up the same energy at each angle. Figure 30 illustrates the geometry.

The problem with sputtering as a source, was that it had never seemed to be able to provide an adequate flux of ions. However, the only previous mention of sputtering had been prior to the advent of the Sigmund theory, and before it was acknowledged that the magnetospheric regions contained large numbers of oxygen ions {Ref.1}. Preliminary calculations at this point indicated that the flux due to oxygen sputtering was sufficient to account for the observed phenomena. It then remained to model the situation and determine more accurately the flux at the detectors due to sputtering.

It was now necessary to evaluate the physical characteristics of the environmental interaction with the spacecraft. As the bulk of the vehicle surface was covered with solar panels, the most likely target of the incident ions would be amorphous silicon dioxide. For a magnetically disturbed time period, the ion flux would be composed primarily of oxygen and hydrogen. The Sigmund theory has a strong dependence on the mass of the incident ions, and it is reasonable to expect a much larger sputtering yield for the heavier ion. See, for example, Figure 14 for H^+ and O^+ on amorphous silicon.

The next step was to use the equations (1-7) and (1-8) to calculate the yield. One roadblock to this was the

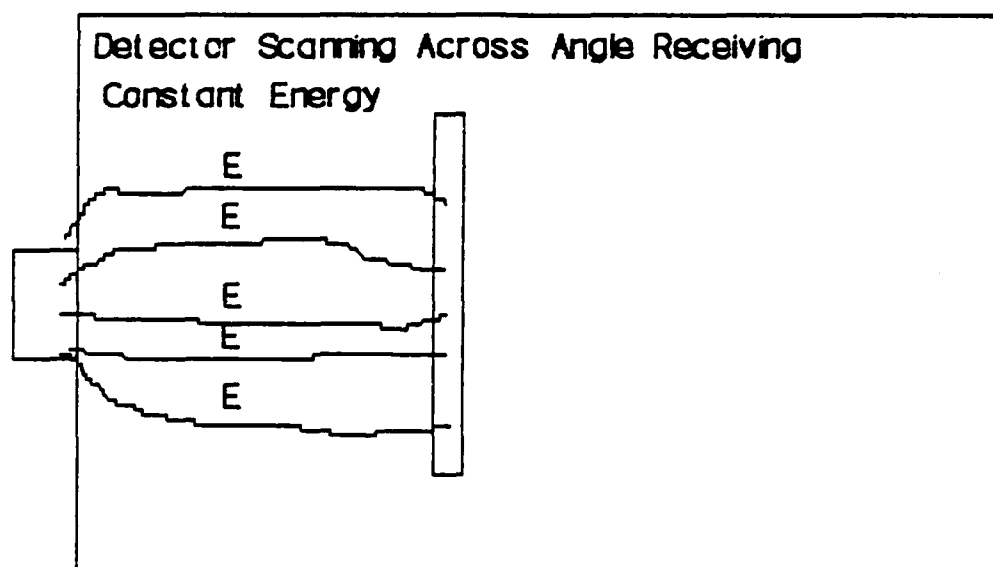
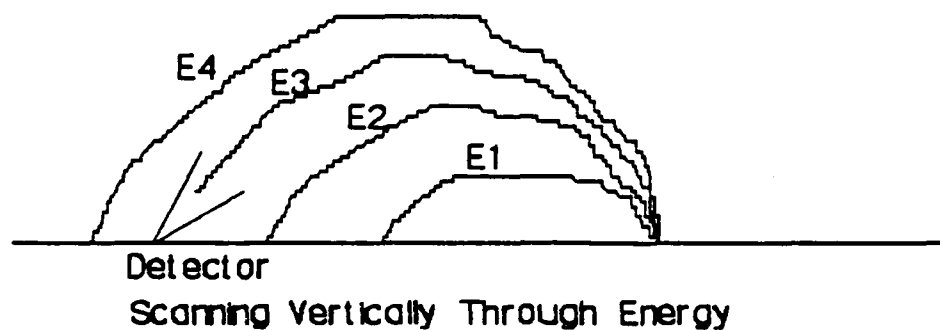


Figure 30. Detector Beam Viewing Geometry

inability of the Sigmund theory to adequately treat sputtering from multi-atomic targets. There are some data points available for impacting molecular oxygen on silicon and silicon dioxide, and they are listed in Table 9 {Ref.36}. If the data from Table 7 are applied to Table 9, we see that the sputtering yield for O^+ on silicon will range from .1 to .18 at 10 keV. Similarly, the yield on silicon dioxide will range from .23 to .44 atoms per ion at 10 keV. The sputtering yield calculated from the Sigmund theory for atomic oxygen on silicon is too high, and more accurately approximates the yield from SiO_2 . We will, however, take the worst case approach, and calculate the yield for silicon. To do this, we will increase the binding energy, to give us values more in line with those from the experiment. The two yield curves are displayed in Figure 31. The new binding energy is 26.0 eV.

Given that this new curve now reasonably describes the sputtering yield, the problem is to calculate how many particles emitted from a surface will reach a differentially charged detector for a realistic incident flux. The total yield of sputtered particles will be described by

$$(3-1) \quad Y = \int_0^r S(v, \theta) v f(v) d^3v$$

In this expression, r is the maximum energy a sputtered particle can have, that is, the maximum amount of energy transferred. This maximum is calculated by

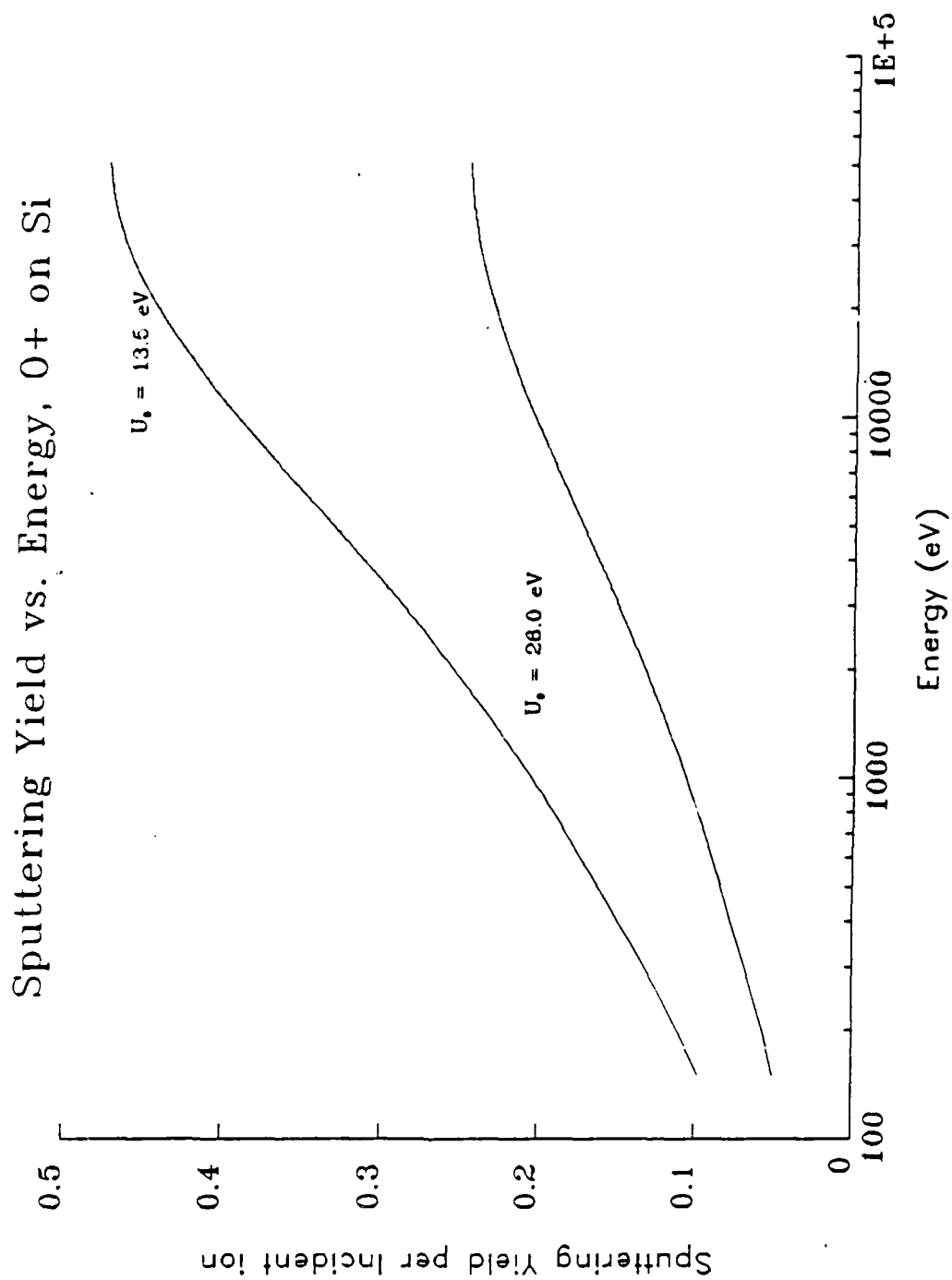


Figure 31. Oxygen-Silicon Yield Curves

$$\Gamma = \frac{4 M_1 M_2}{(M_1 + M_2)^2} E_m,$$

and is equivalent to the maximum energy transferred in a binary collision. The function $f(v)$ is the distribution function of the incident ions, and $S(v, \theta)$ is the sputtering yield.

With the total yield in hand, we may now attempt to calculate the countrate at the detector. The total number of counts the detector receives may be described by the following equation,

$$(3-2) \quad \text{Counts} = \int dt \int dA \int f(v) (\vec{v} \cdot \hat{n}) d^3v$$

This assumes that the detector is differential in time, area, solid angle, and energy. If we integrate over the area increment and time, we get,

$$(3-3) \quad \text{Counts} = T \delta A \int d\Omega \int v^2 f(v) (\vec{v} \cdot \hat{n}) dv$$

Thus, the countrate is

$$(3-4) \quad \text{Countrate} = \text{Counts} / \text{Time} = \delta A \int \int v^2 f(v) (\vec{v} \cdot \hat{n}) dv d\Omega$$

To continue, we must assume that limits of integration on $d\Omega$ are not a function of energy, and that the value of the integral may be given by a simple number, characteristic of the detector. This is not actually true, as the limits on integration depend strongly on energy, since $f(v)$ may not fill the entire 5 by 7 degree aperture of the detector. The

inaccuracy of this assumption will surface later. With the assumption, we derive,

$$(3-5) \quad \text{Count rate} = CR = \delta A \delta \Omega \int v^2 f(v) (\hat{v} \cdot \hat{n}) dv$$

The two constants, δA and $\delta \Omega$, are combined into the geometric factor G , a constant for the detector. For our detectors, $G = 1.6 \times 10^{-3} \text{ m}^2 \text{ ster}$. Due to the differential aperture of the detector, the value of the dot product $\hat{v} \cdot \hat{n}$ is approximately v (i.e. $\cos \theta \approx 1$).

We must now determine the distribution function of the emitted particles. From the earlier discussion of the Thompson Theory, it is evident that the energy distribution of the yield flux is proportional to $E/(E+U_0)^3$. That is, we have the function

$$(3-6) \quad \frac{dY}{dE} = A \frac{E}{(E+U_0)^3}$$

The flux Y , is also given by

$$(3-7) \quad Y = B \int_0^\infty E f(E) dE$$

where $f(E)$ is the distribution function as a function of energy of the emitted particles, and B is a constant that involves the integral over the solid angle. If we combine these two relationships, it is evident (disregarding constants) that

$$(3-8) \quad f(E) = \frac{1}{E} \frac{dY}{dE} = \frac{1}{(E + U_0)^3}$$

We will now determine the appropriate normalization constants. From the definition of the distribution function,

$$(3-9) \quad n = \int_{-\infty}^{\infty} f(v) d^3v$$

Continuing the calculation, we assume that the yield flux and the distribution function have similar angular dependencies. Thus, $f(v, \theta) = f(v) \cos \theta$. If we break down d^3v , and substitute for energy, we get

$$(3-10) \quad n = A \int d\phi \int \sin \theta \cos \theta d\theta \int f(E) \frac{(2E)^{3/2}}{(m^3)^{3/2}} dE$$

In the case of emission from a surface, ϕ will range from 0 to 2π , and θ will vary from 0 to $\pi/2$. Integrating over these limits, the equation reduces to

$$(3-11) \quad n = A\pi(2/m^3)^{3/2} \int \frac{E^{3/2}}{(E + U_0)^3} dE$$

This integral will extend the full energy range of the emitted particles, that is, from 0 energy to r , the maximum energy transferred in the collisions. If one then substitutes a dummy variable, x^2 , for E the integral has a standard form {Ref. 37}. Solving, we then get

$$n = A\pi(2/m^3)^{3/2} \int_0^r \frac{E^{3/2}}{(E + U_0)^3} dE$$

$$n = A\pi(8/m^3)^{3/2} \int_0^s \frac{x^2}{(x^2 + U_0)^3} dx \quad s = r^{1/2}$$

$$n = A\pi(8/m^3)^{1/2} \left\{ \frac{-x}{4(x^2 + U_0)^2} + \frac{x}{8U_0(x^2 + U_0)^2} + \frac{1}{8(U_0^3)^{1/2}} \tan^{-1} \left(\frac{x}{U_0} \right) \right\} = 0$$

$$n = A\pi(8/m^3)^{1/2} \left\{ \left(\frac{r}{8(U_0 + r)} \right) \left(\frac{1}{U_0} - \frac{2}{(U_0 + r)} \right) + \frac{1}{(8U_0^3)^{1/2}} \tan^{-1} \left(\frac{r}{U_0} \right) \right\}$$

Defining β as the large constant on the right side, we get

$$n = A\pi(8/m^3)^{1/2} \beta$$

or

$$(3-12) \quad A = n m^{3/2} / \pi \beta 8^{1/2}$$

Using this normalization constant, the distribution function becomes

$$(3-13) \quad f(E, \theta) = (n m^{3/2} / \pi \beta 8^{1/2}) \cos \theta \frac{1}{(E + U_0)^3}$$

If we then calculate the yield flux, Y , we obtain

$$Y = (1/2m)^{1/2} (n/\beta) \int_0^r \frac{E}{(E + U_0)^3} dE$$

$$(3-14) \quad Y = (1/2m)^{1/2} (n/\beta) \left\{ -(r + U_0/2)/(r + U_0)^2 + (1/2U_0) \right\}$$

$$Y = (1/2m)^{1/2} (n/\beta) \delta$$

or

$$(3-15) \quad n = (2m)^{1/2} \beta Y / \delta$$

Therefore, substituting in the distribution function,

$$(3-16) \quad f(E, \theta) = \frac{m^2}{2\pi} \frac{Y}{\delta} \frac{1}{(E + U_0)^3} \cos \theta$$

We now have an expression for the distribution function of the emitted particles. This expression can then be inserted with one modification into eqn. (3-5) to determine the countrate at the detectors. The necessary modification accounts for the differential charge between the emitting surface and the detectors. For the particles to be accelerated to the detector, the surface must be charged positively relative to the detectors, therefore ϕ will be negative. Since E will map to $E + q\phi$ (Liouville's Theorem), we will obtain

$$(3-17) \quad f(E, \theta, \phi) = \frac{m^2}{2\pi} \frac{Y}{\delta} \frac{1}{((E-\phi) + U_0)^3} \cos\theta$$

Here, we have assumed that the ions are singly charged, and ϕ will be converted to eV from V on this basis. The countrate expression is then,

$$(3-18) \quad CR = G(2/m^2) \int f(E, \theta, \phi) E dE$$

$$(3-19) \quad CR = \frac{2GY}{\pi\delta} \cos\theta \int \frac{E}{((E-\phi) + U_0)^3} dE$$

To find the countrate, we must now integrate for each of the detector energy channels over its energy range. As this resolution is 20%, the upper and lower limits are $1.1E_c$ and $0.9E_c$, where E_c is the central energy of the energy channel. The integral in eqn. (3-19) is a standard form, and the countrate may finally be written as,

$$(3-20) \quad CR = \frac{2GY}{\pi\delta} \cos\theta \left\{ -\frac{(2.2E_e + U_e - \phi)}{2(1.1E_e + U_e - \phi)^2} + \frac{(1.8E_e + U_e - \phi)}{2(.9E_e + U_e - \phi)^2} \right\}$$

If the energy channel limits are both less than ϕ , then the countrate over that channel is zero. If the lower limit is below ϕ , then the integral is taken between the upper limit and ϕ .

B. CALCULATION OF THE SPUTTERING FLUX AT THE DETECTOR

Using the Sigmund Theory developed above, and the derived expression for the countrate at the detector, we developed a program to calculate the sputtering yield, incident and emitted flux, and the response of the detector to changes in both the energy channel and differential charge, ϕ . Data for the ambient plasma compositions was available from the Lockheed Ion Mass Spectrometer for days 83, 86, and 200 of 1979. The values utilized are listed in Table 10.

The first portion of the program was the calculation of the total yield or emitted flux. This value is calculated from the following expression;

$$(3-21) \quad Y = \int_0^\infty v f(v) S(v, \theta) dv$$

In this relation, $v f(v)$ is the flux of the ambient ions as a function of velocity, and $S(v, \theta)$ is the sputtering yield as a function of velocity and angle. The factor $S_n(\epsilon)$ in $S(v, \theta)$ exists in tabulated form, and is not described by a simple continuous function. If the points are fitted to a

curve, we arrive at the equation;

$$(3-22) \quad S_n(\epsilon) = .35874 - (.17885)\log\epsilon - (.14359)(\log\epsilon)^2 \\ + (.06193)(\log\epsilon)^3 + (.04228)(\log\epsilon)^4 \\ - (.00541)(\log\epsilon)^5 - (.00630)(\log\epsilon)^6 \\ - (.00092)(\log\epsilon)^7$$

This equation and the available tabulated points are displayed in Figure 32. Since $S_n(\epsilon)$ is a complicated function, the integral was evaluated numerically. The function was calculated at a thousand points over an energy range that depended on the temperature of the ambient Maxwellian distribution. For a 4000 eV distribution, the high energy was 50000 eV and the low energy was 100 eV. 100 eV was chosen as the lower limit, as most sputtering yields are approximately zero by that point. At the 50000 eV point, the value of the distribution function has reduced by a factor of 10^{-20} from the peak value.

The yield obtained in this method was then multiplied by .02, as approximately 2%-4% of the emitted flux is ionized {Ref. 29}. This ion yield is substituted in the countrate integral to obtain the detector responses. The values of the integrals were varied over energy channel and differential charge to determine if the responses were very narrow as observed. Figures 33 shows the values of the incident, emitted, and ion fluxes for oxygen as a function of energy for day 86 of 1979. The figures for days 83 and 200 are similar. From this it is very clear that the incident flux is much greater than the emitted ion flux.

The Lindhard Universal Function

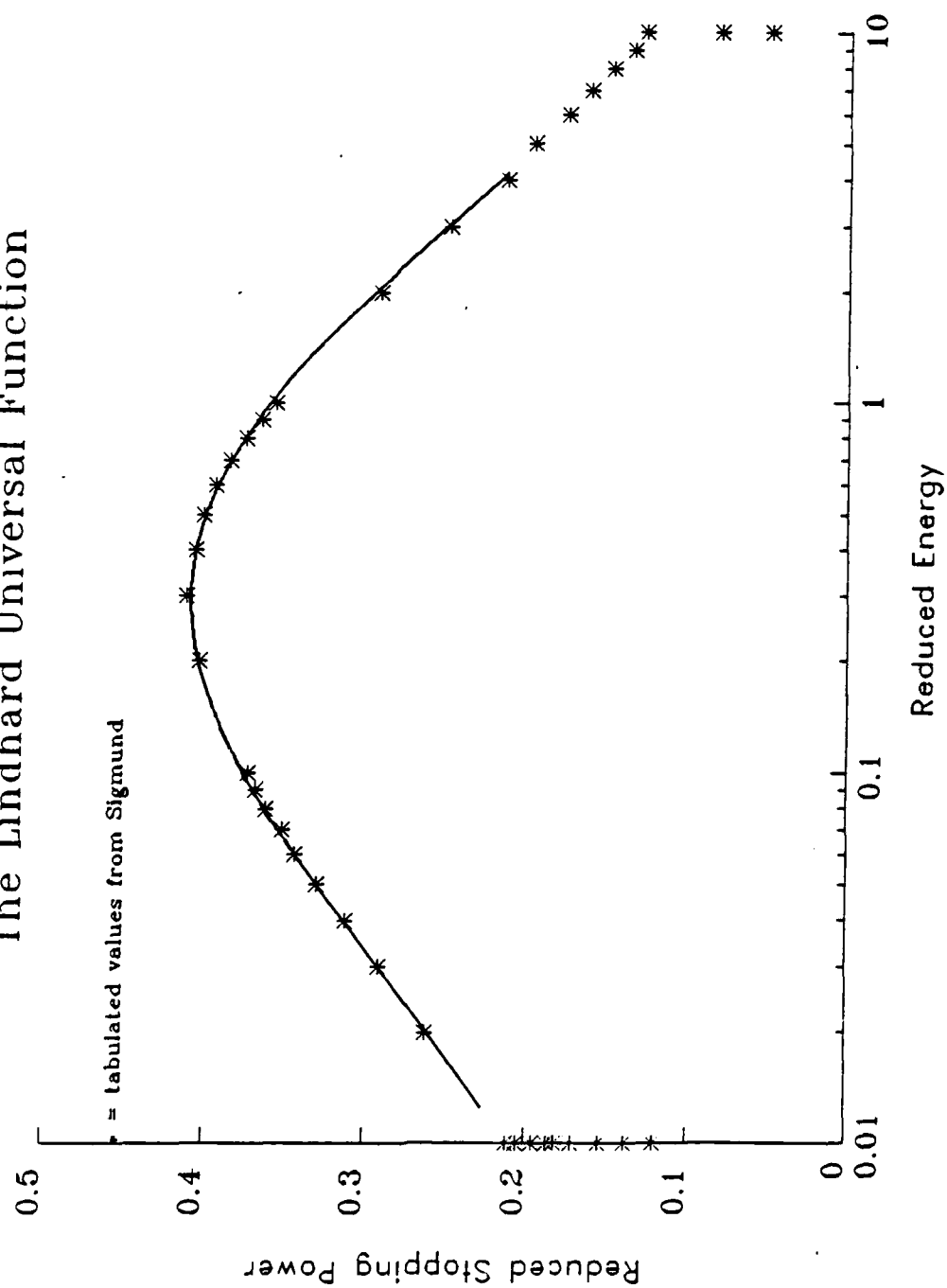


Figure 32. Lindhard's Universal Function {Ref.27}

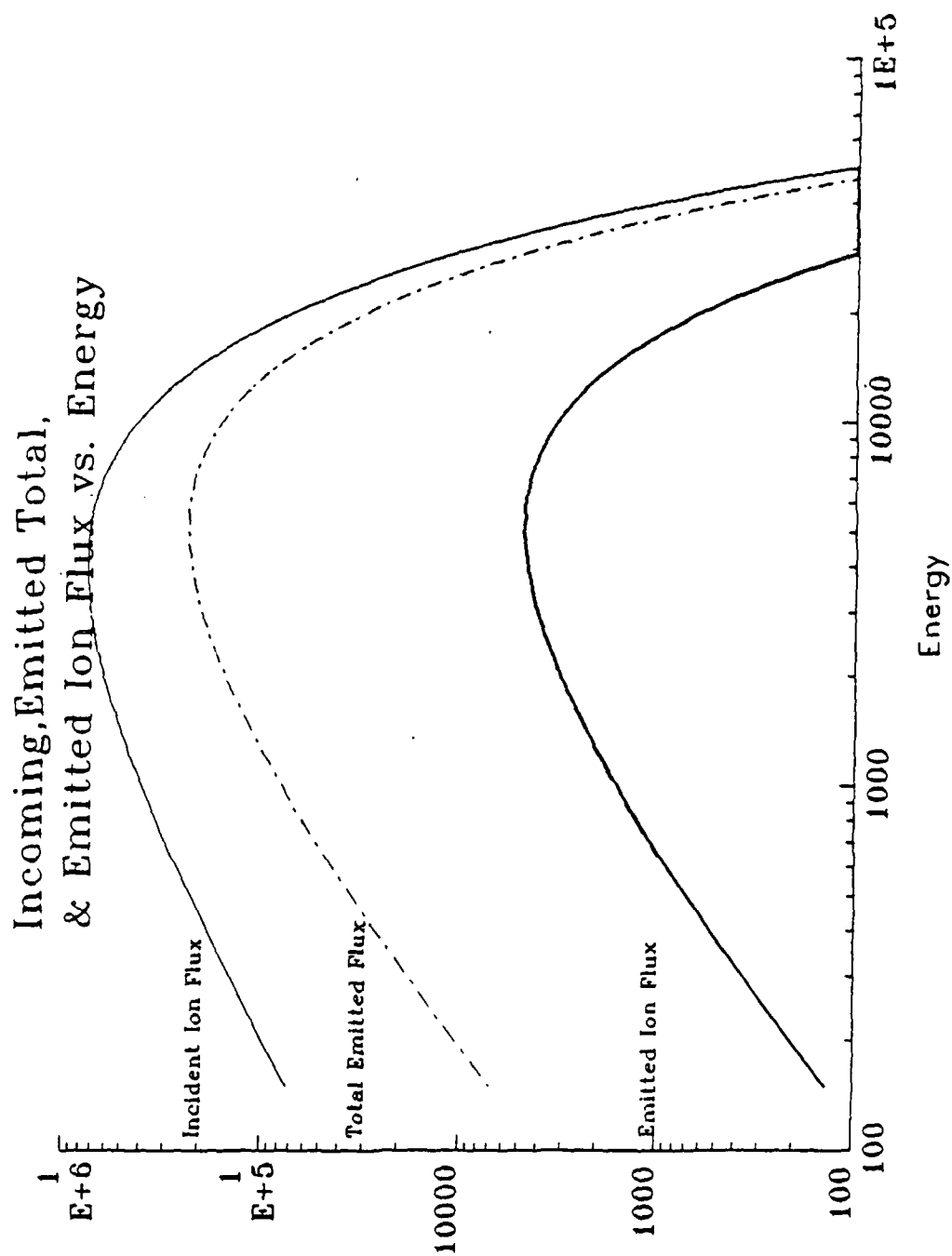


Figure 33. Incident, Emitted, and Ion Fluxes
Day 86 of 1979

Thus there is a net accumulation of positive charge on the spacecraft due to the ambient ion current.

Figures 34 and 35 are displays of the countrate as a function of energy channel for a constant (35 eV) differential charge, for days 86 and 200 for oxygen induced emission. We see that the countrate is high in 3-4 of the energy channels. The data indicates that it in fact should be concentrated in only one channel. However, the above equations assume that the detector surface is a flat plate, and that all particles reaching that plate are counted. This is in fact not true. The detector viewing cone is probably not completely filled, as noted previously, and we are seeing the error due to treating the factor $\delta\Omega$ as a constant in eqn. (3-3). This factor will serve to reduce the countrate overall, and since particles at the edges of the viewing cone (with different energies from the cone center) will be reduced, the peak will most likely become narrower. The response for a specific channel and varying differential charges is quite similar. That is, a given channel will only respond for a certain narrow range of differential charge. Similar calculations for the ambient hydrogen population on the same days indicate that it can also generate a significant flux at the detectors, simply due to the large amount present. The relative contributions of these two ambient plasma components vary widely, depending on the temperature and density of their

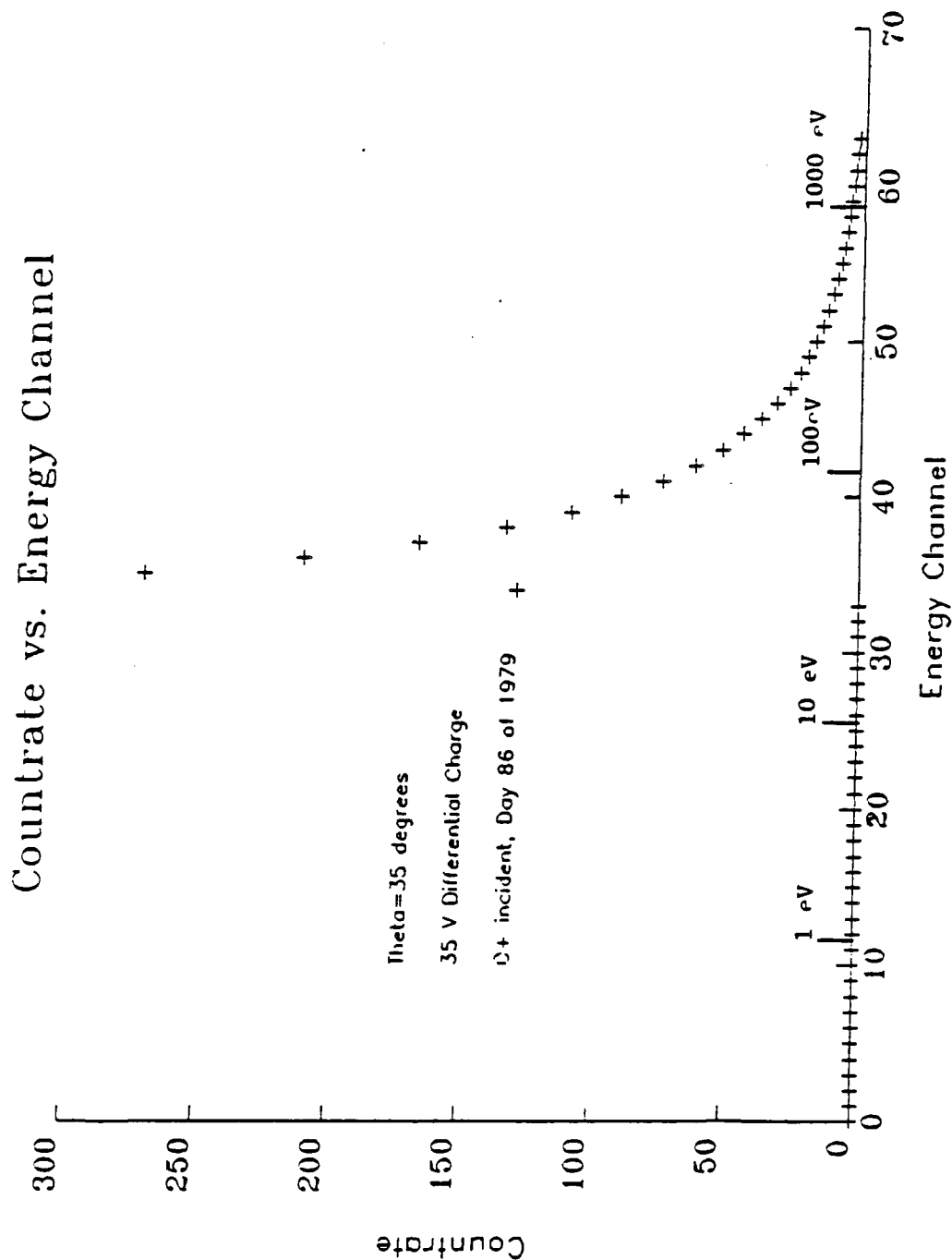


Figure 34. Channel Response for a 35 V Differential Charge
O+ Incident, Day 86, 1979

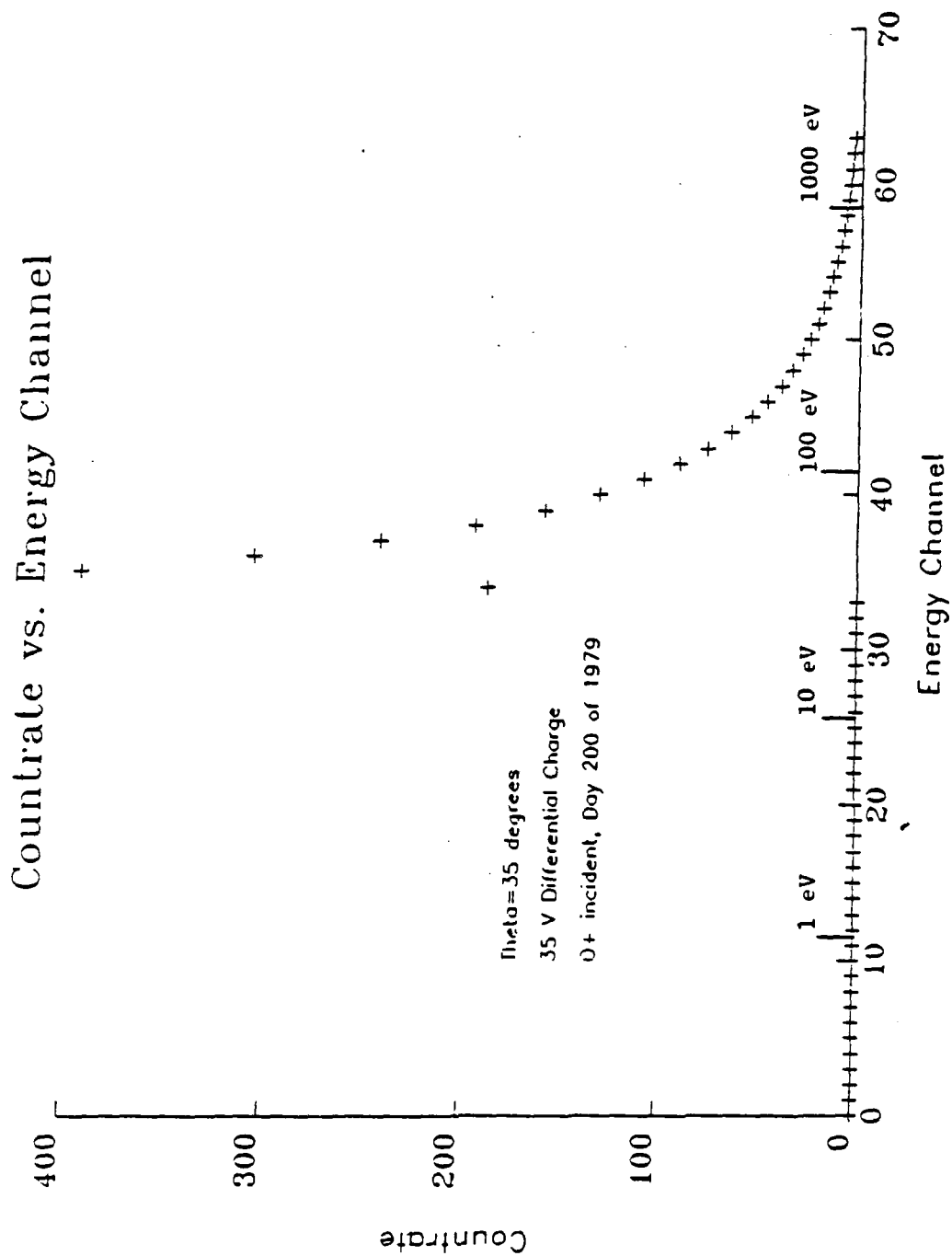


Figure 35. Channel Responses for a 35 V Differential Charge
 O+ Incident, Day 200, 1979

respective distributions. In general, the oxygen contribution is dominant.

The countrates from the detectors are available for the above three days. On day 83 of 1981, the measured countrates varied from 29 - 800 counts per second, with the average at 360. For day 86, the range was 24 - 1080, with the average at 300. Day 200 was much lower, between 25 and 213, with an average value of 120. The available mass spectrometer data was averaged over one hour periods, so we will generally calculate only one representative number for the charging time frame. The calculated countrates were 380, 325, and 400 for days 83, 86, and 200, respectively. Considering the approximate nature of the calculations, the theoretical responses compare favorably with the measured data, with the exception of day 200. However, it has already been noted that this data from the Hi detector indicated a sputtering source different from those seen on the Lo detector. This further supports that observation, as the sputtering yield for this event is clearly much lower.

As the assumptions in this calculation tend to minimize the number of detected particles, it seems reasonable to conclude that sputtering from a differentially charged surface is sufficient to account for the narrow triangle peaks. These discrete responses will serve to explain the triangle and shadow peaks. This leaves the diffuse background. We require a broad response, with the particles

scattered equally across the energy channels. Figure 36 gives the log distribution function as a function of energy for an emission angle of 0 degrees. The distribution function has its maximum in the low energy channels, and numerically compares favorably with Figures 21 and 24. The broad spectrum may then be described as the returning emissions from non-differentially charged surfaces.

We must now explain the shadow peaks. These appear to be a combination of two occurrences, acceleration from a differentially charged surface to a motionless detector, or acceleration from a differentially charged surface to a detector scanning laterally across the emitted beam, as opposed to vertically. See Figure 31 for a view of the geometry. Since this is then a variation of the triangle peaks, the source and results would be the same.

The trajectories to the detectors can be recreated by the NASCAP program. Figure 37 displays the particle trajectories for the observed angles and energies at the Lo detector on day 86. From top to bottom, the lines are as follows; a) 84 eV, 145 degrees, or 12.5 degrees above the spacecraft plane, b) 70 eV, 152 degrees, c) 60 eV, 175 degrees, d) and 53 eV, 188 degrees. One can see that the particles track back to the spacecraft surface to different points. These points are all located in the solar array portion of the spacecraft surface. These results are as expected. The solar array has charged differentially, and

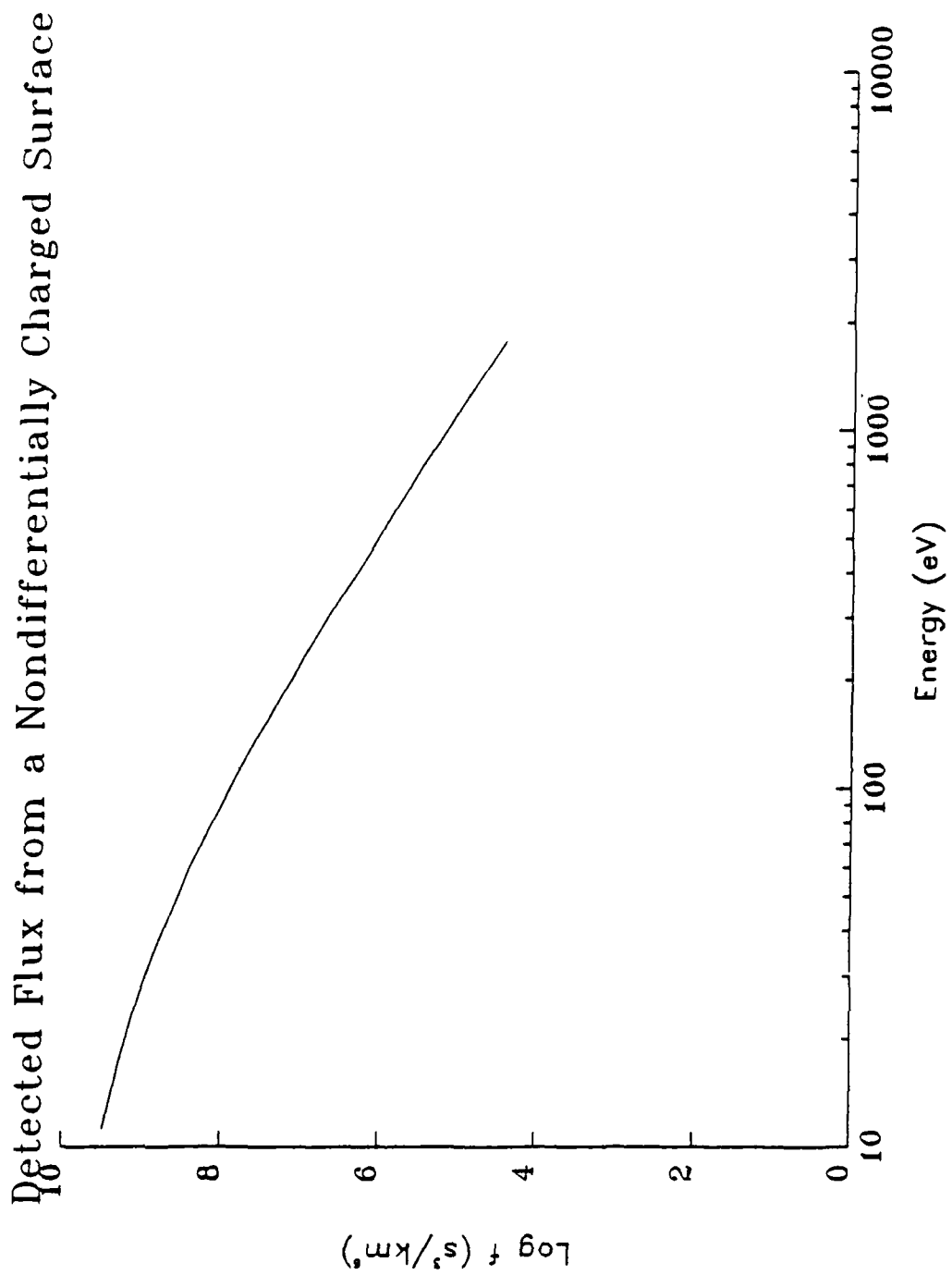


Figure 36. Channel Response for a Zero V Differential Charge

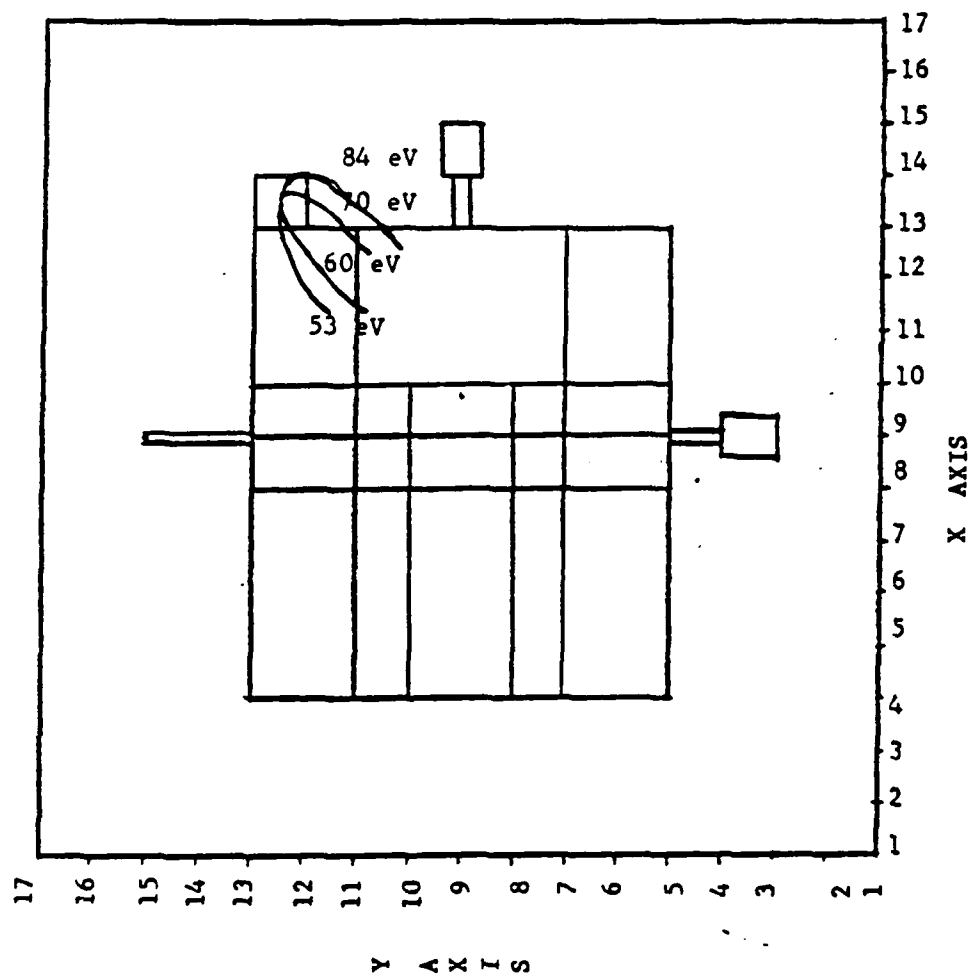


Figure 37. NASCAP Trajectories, Day 86 of 1979

the sputtered particles follow specific trajectories in the electric fields. The limited view cone of the detector only picks up specific energies.

NASCAP was also run for the potentials observed on day 94. The code was run to simulate the responses of the Lo, Hi, and Fix detectors to a range of incoming particle energies. The energies ranged from 2.0 to 90.1 eV. As noted above in the observations, the spacecraft was charged to -60 V, and peaks were noted at various lower energies on the detectors. The Hi detector was parked at 67 degrees, and the Lo at 91 degrees. Thus, Hi and Lo detectors were sampling approximately the same region of space.

Figures 38 and 39 depict the Lo detector trajectories in two different planes. The first shows the top of the spacecraft surface. Particles at energies less than 43 eV are returned to the spacecraft. The trajectories corresponding to observed particles are marked with an asterisk. The second figure is a complementing view from the left side of the first figure. These two figures indicate that the actually observed particles are emitted from the satellite's forward end. Additionally, there are gaps from which no particles are seen at the detector. An explanation for this is the existence of patches of different nonconducting material on the forward surface for use in the Satellite Surface Potential Monitor (SSPM). When these patches (kapton, silvered teflon, and quartz) charge

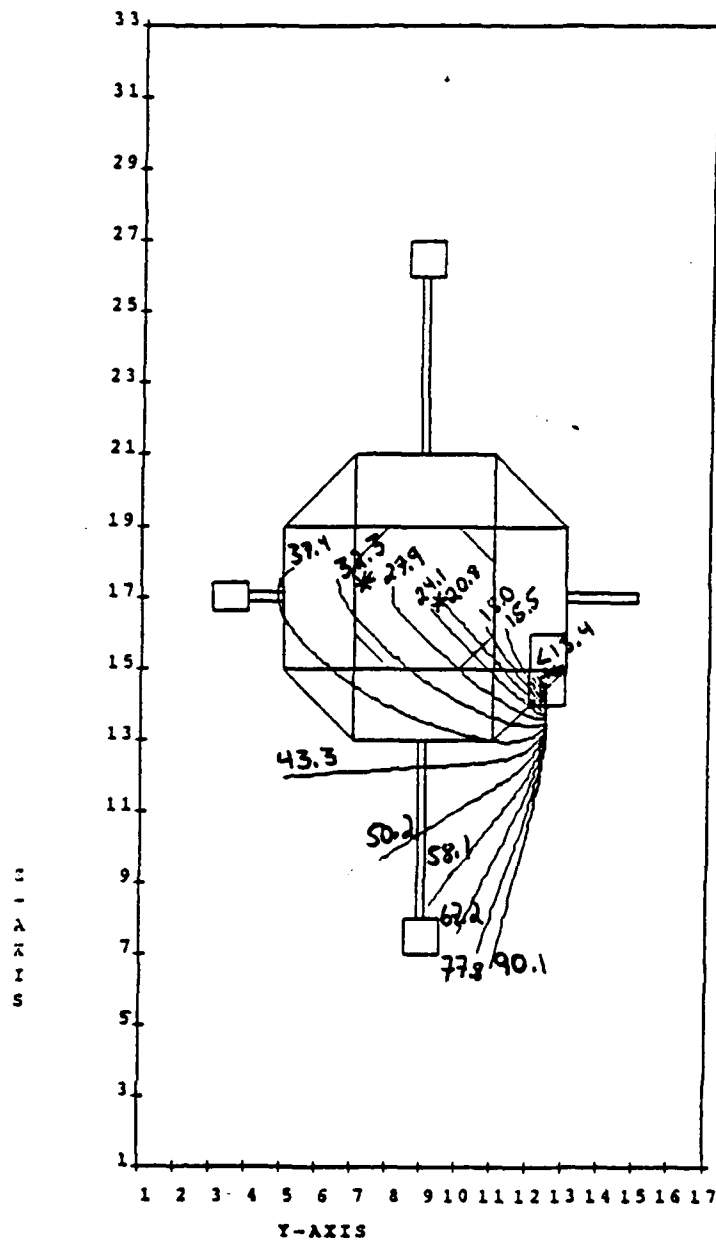


Figure 38. NASCAP Trajectory, Day 94, Lo Detector

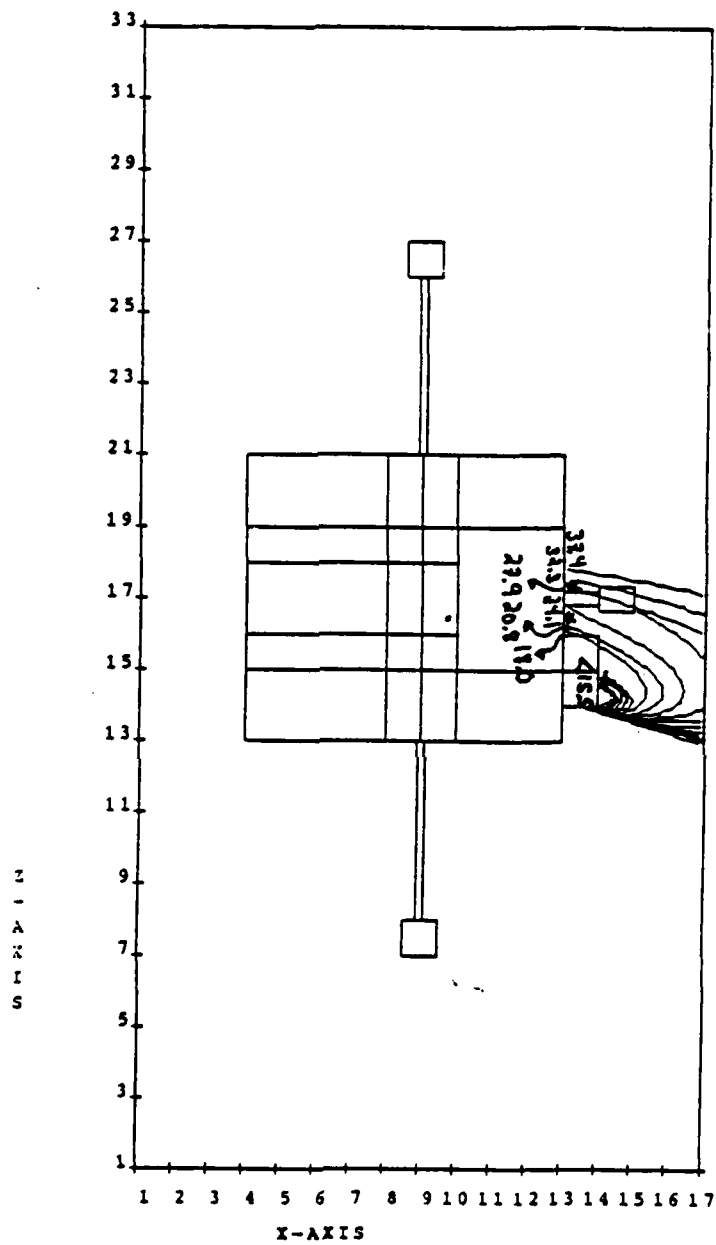


Figure 39. NASCAP Trajectory, Day 94, Lo Detector

differentially, the particles reaching the detector from each will follow different trajectories, and have different energies. Additionally, the S-band antenna mast on the forward end is nonconducting, and may be a particle source.

Figures 40 and 41 are similar views for a model of the Hi detector trajectories. We see that the origin of the particles is also on the upper surface, and the data shows the same striations. Again, the only nonconducting surfaces on the forward end are the SSPM and the antenna. The detail on NASCAP is not sufficient to study the extremely strong local electric fields expected in this region. If the satellite potential is 100 V, then the field due to the sheath is approximately 1 V/m. In the forward surface vicinity, with a differential potential of 30 V, the fields will be on the order of 30-60 V/m, and will significantly distort the local trajectories of particles. Thus, the NASCAP trajectory plotting routine is somewhat unreliable in this region. Looking at both figures, however, the origins for the two detectors are reasonably close, and allowing for the local fields, may possibly come from the same surface. As a working hypothesis, we will assume that the SSPM is the source of the emitted particles.

Figures 42 and 43 model the fixed detector. The views are similar to those above. We see that the particles viewed by the fix detector come from completely different regions of the spacecraft. All the obviously reattracted

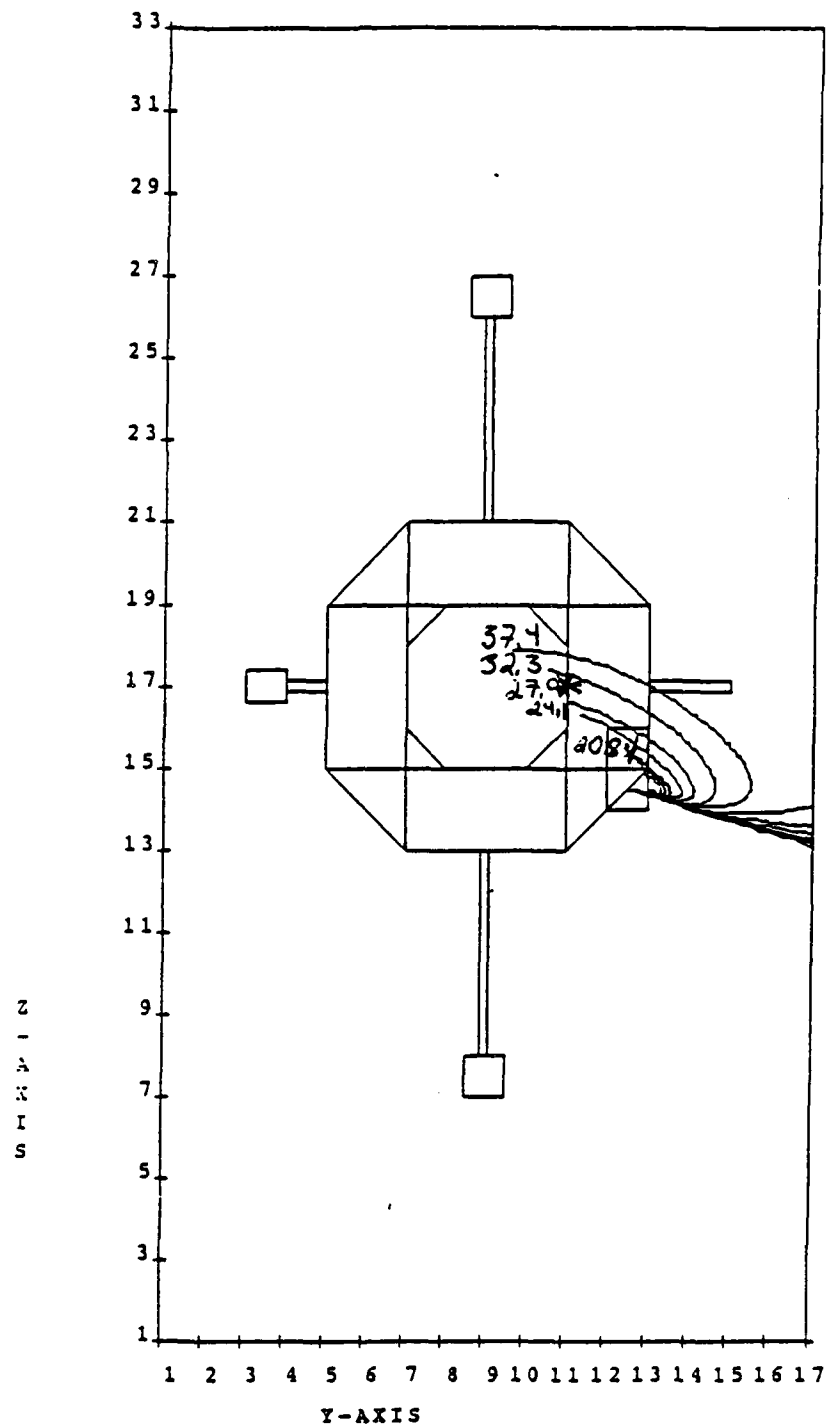


Figure 40. NASCAP Trajectory, Day 94, Hi Detector

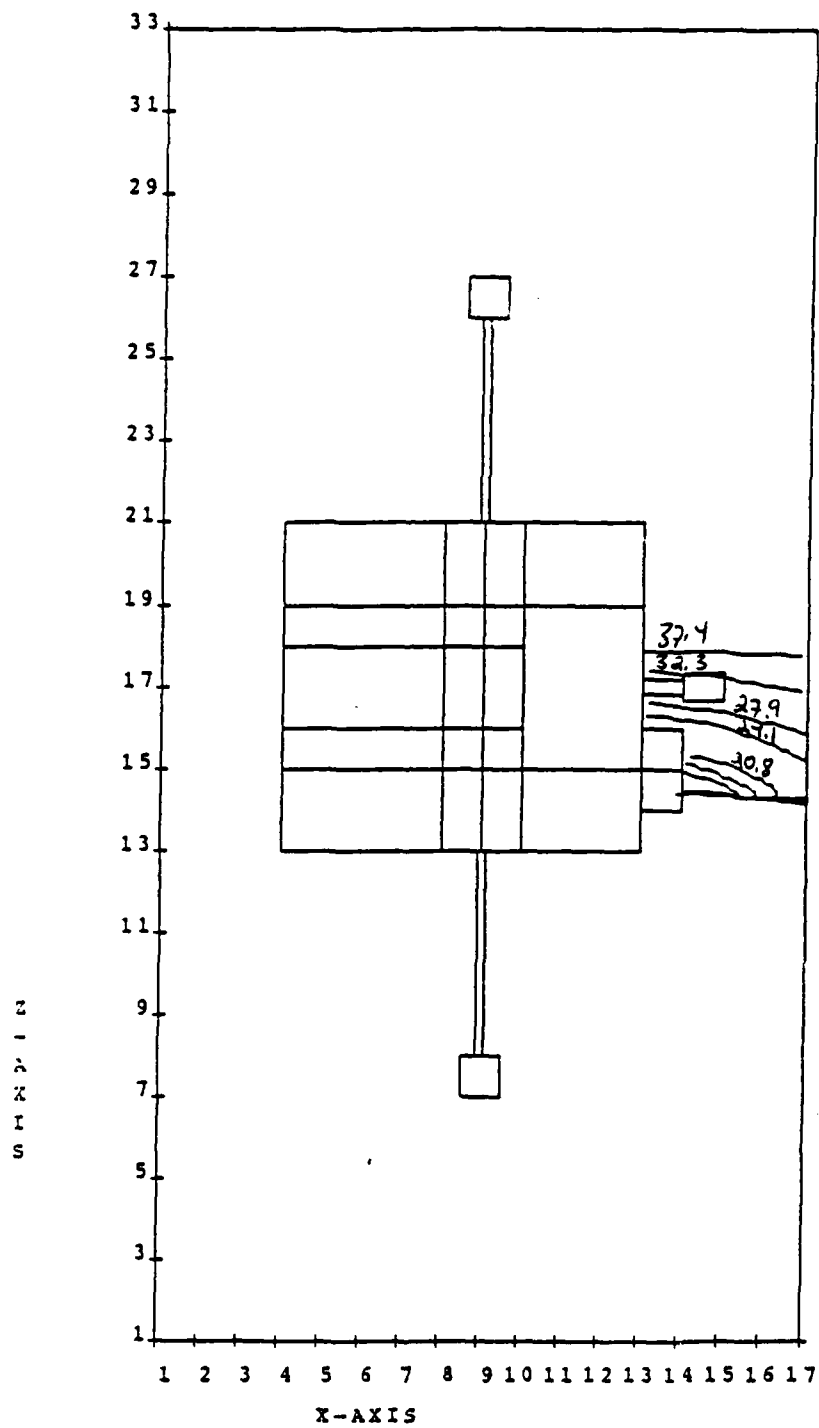


Figure 41. NASCAP Trajectory, Day 94, Hi Detector



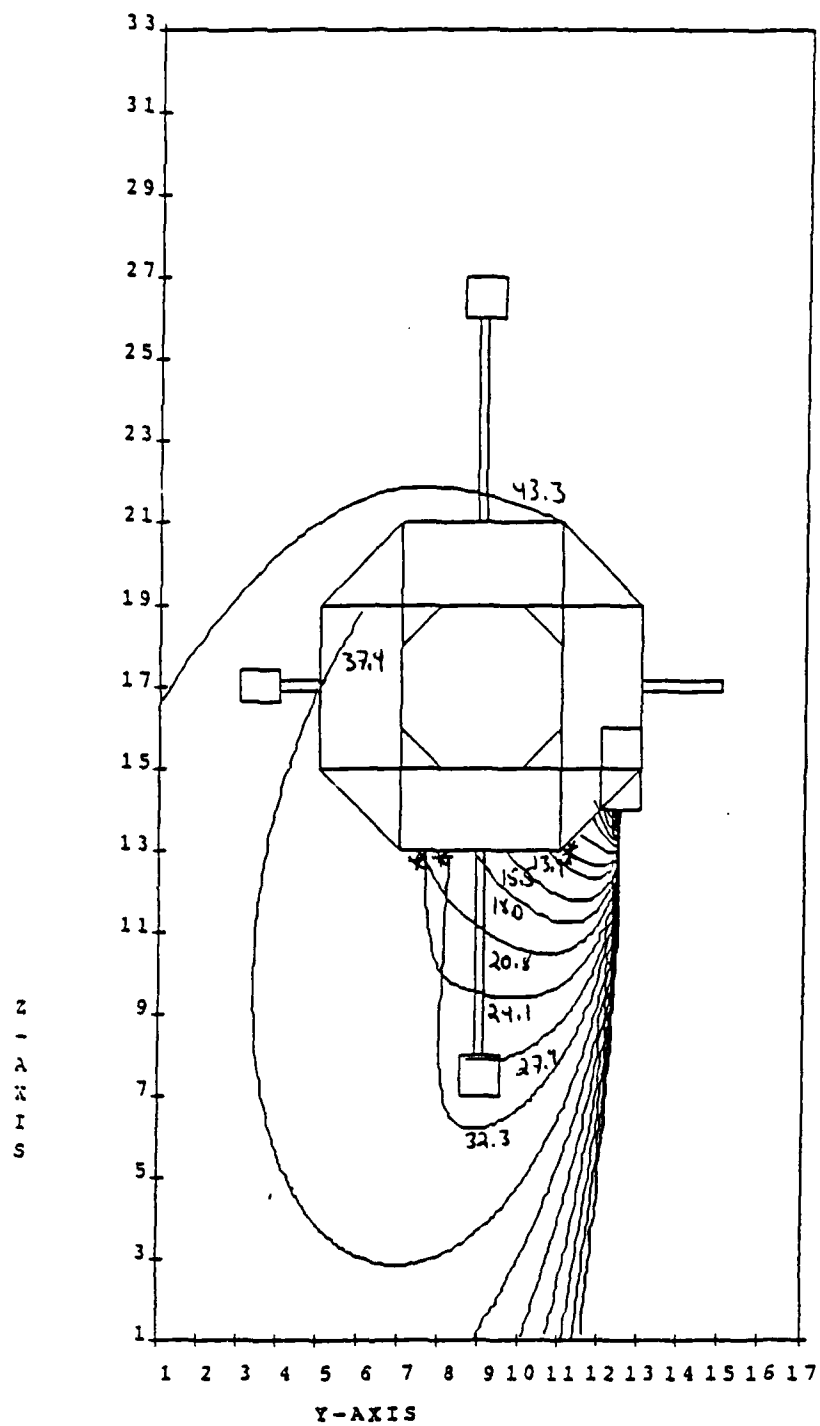


Figure 43. NASCAP Trajectory, Day 94, Fix Detector

particles have energies of less than 43 eV, as did the other two detectors. We can see that the trajectories of the particles skip over the bellyband region. This is reasonable, as the bellyband would be expected to be at the satellite mainframe potential, and thus particles emitted would not be accelerated by a differential charge. The trajectory calculations for the Fix detector also support the theory of sputtering from differentially charged surfaces.

IV. CONCLUSIONS

It is reasonable to conclude that sputtering is a likely source of the observed phenomena. It can satisfactorily explain the flux and structure of the triangle and shadow peaks. It also can account for the observed broad spectrum of ions. These fluxes are large enough to be measured by the detectors, but are they large enough to cause substantial damage to the spacecraft surface?

For this data set, the sputtering yield was less than the incident flux, so that the net result was particle accretion on the surface. Coincidentally, the data in this thesis were taken from relatively low energy days. On higher energy days, the sputtering yield increases, and the net result is surface depletion. However, the surface damage caused by this process appears to be minor. Assuming a higher energy day, with emission on the order of twice the incident flux, one atomic layer will be removed from a silicon dioxide surface every 8 years. Since the solar cells are covered by the glass shields, they will be impervious to the surface sputtering.

Another facet of this is the damage to surface conducting coatings on spacecraft. These coatings are only several atoms thick and may be expected to sputter from the surface within several months of the satellite launch. This

may account for the observed charging on the ISEE-1 satellite.

Since the energy spectrum of the sputtered particles dies off quite rapidly, and the observed differential charges are usually not large, it is not likely that any great contamination of the charging peak results. The sputtering in general will probably be uniform over a given material. Surfaces will be worn down over large areas as opposed to experiencing significant localized damage. Therefore, it appears that no short term damage will result from sputtering on spacecraft.

Further work is required to accurately calculate the sputtering yields from various surfaces to prove or disprove these conclusions. At this point, given the current state of the sputtering field, it is not possible to state with any certainty whether extensive damage will result from ambient ion bombardment. There appears to be no work in progress anywhere to determine experimentally the sputtering yields for most ion-target combinations. Since the Sigmund Theory is so limited, these results are necessary for any actual calculations of the effect of the ambient heavy ion bombardment on space vehicles.

This thesis demonstrates that sputtering is the probable cause of the observed low energy ion fluxes. Additional work is required to refine the NASCAP trajectory information and couple it with the theory developed here to model the

detector response accurately. It is recommended that this work be continued when and if further applicable sputtering data become available.

APPENDIX

TABLE 1

MAGNETOSPHERIC IONS AND THEIR SOURCES {Ref. 7}

<u>Origin</u>	<u>Source</u>	<u>Ions</u>
Sun	Solar Wind	H^+, He^{++}, O^{6+}
Earth	Ionosphere	H^+, He^+, O^+
Earth	High Altitude Thermal Plasma, Plasmasphere	$H^+, He^+, He^{++}, O^+, O^{++}, O^{3+}$

TABLE 2

STORM TIME RING CURRENT COMPOSITION {Ref. 8}

Date	07 July 1977	26 Nov 1977	09 Mar 1978	30 May 1978
H ⁺ Flux 10 ⁷ cm ⁻² s ⁻¹	1.26	4.20	13.0	6.0
Density 10 ⁻² cm ⁻³				
H ⁺	11	44	143	58
He ⁺	.72	4.3	10.9	6.6
O ⁺	8.3	91	228	107
Mean Energy keV				
H ⁺	8.3	5.7	5.1	6.4
He ⁺	4.5	4.3	5.4	2.7
O ⁺	4.9	3.8	5.3	4.4

TABLE 3

STORM TIME MAGNETOSPHERE COMPOSITION {Ref. 8}

Date	04 May 1977	29 July 1977	29 Jan 1978	02 June 1978
H ⁺ Flux 10 ⁷ cm ⁻² s ⁻¹	3.3	2.4	10	2.8
Density 10 ⁻² cm ⁻³				
H ⁺	26	20	10	27
He ⁺⁺	1.5	.16	9.3	.37
He ⁺	1.8	.9	.3	.79
O ⁺	3.0	13	4.9	60
Mean Energy keV				
H ⁺	9.6	8.5	4.2	6.8
He ⁺⁺	20.3	15.9	8.6	14.9
He ⁺	4.8	3.9	6.4	4.8
O ⁺	4.5	4.7	5.4	4.1

TABLE 4

VALUES OF THE REDUCED STOPPING POWER {Ref.27}

$S_p(\epsilon)$	ϵ	$S_p(\epsilon)$	ϵ
0.120	0.002	0.403	0.20
0.154	0.004	0.405	0.40
0.211	0.01	0.356	1.00
0.261	0.02	0.291	2.00
0.311	0.04	0.214	4.00
0.372	0.10	0.128	10.0
0.393	0.15	0.0813	20.0
		0.0493	40.0

TABLE 5

CALCULATED AND MEASURED SPUTTERING YIELDS FOR VARIOUS
MATERIALS {Ref. 23}
THE NUMBERS IN PARENTHESES ARE THE YIELDS CALCULATED
FROM THE SIGMUND THEORY

TARGET MATERIAL	U ₀ (eV)	Z _e	<u>Sputtering Ratio (atoms/ion)</u>			
			Ne ⁺	Ar ⁺	Kr ⁺	Xe ⁺
Pb	2.01	82	3.6	10.5 (29.7)	24.0 (44.0)	44.5 (74.6)
Ag	2.94	47	4.5	10.8 (12.7)	23.5 (20.1)	36.2 (24.0)
Sn	3.11	50	1.8	4.3 (12.5)	8.5 (19.5)	11.8 (4.9)
Cu	3.46	29	3.2 (3.7)	6.8 (6.7)	11.8 (11.9)	19.0 (15.5)
Au	3.79	79	3.6	10.2 (16.1)	24.5 (23.9)	39.0 (27.8)
Pd	3.87	46	2.5	5.3 (9.24)	10.5 (14.1)	14.4 (18.1)
Fe	4.29	26	1.3	2.3 (5.15)	4.0 (8.92)	4.9 (11.7)
Ni	4.43	28	1.4	3.5 (5.35)	5.6 (9.01)	7.6 (11.8)
V	5.3	23	0.3	1.0 (3.85)	1.7 (6.21)	1.9 (8.9)
Pt	5.82	78	1.9	5.3 (9.35)	11.3 (15.3)	16.0 (19.2)
Mo	6.82	42	0.6	1.5 (5.14)	2.7 (7.70)	3.8 (10.1)
Ta	8.06	73	0.7	1.6 (6.62)	3.1 (10.0)	4.0 (12.3)
W	8.70	74	1.0	2.3 (5.07)	4.7 (9.31)	6.4 (11.9)

TABLE 6

CALCULATED SPUTTERING YIELDS USING A
MODIFIED BINDING ENERGY.

TARGET MATERIAL	1.7 U _e	<u>Sputtering Ratio (Atoms/Ion)</u>		
		Ar ⁺	Kr ⁺	Xe ⁺
Pb	3.42	17.5	25.9	43.9
Ag	5.00	7.47	11.8	14.1
Sn	5.29	7.35	11.5	14.7
Cu	5.88	3.94	7.00	9.12
Au	6.44	9.47	14.1	16.35
Pd	6.58	5.44	8.3	10.7
Fe	7.29	3.03	5.25	6.9
Ni	7.53	3.15	5.3	6.94
V	9.01	2.26	3.65	5.24
Pt	9.89	5.50	9.00	11.24
Mo	11.59	3.02	4.53	5.94
Ta	13.7	3.89	5.88	7.24
W	14.79	2.98	5.48	7.00

TABLE 7

RATIO OF SPUTTERING YIELD PER ATOM FOR MOLECULAR
AND ATOMIC ION BOMBARDMENT {REF. 31}

Projectiles	Si	Ag	Au
Cl-Cl ₂	...	1.09	...
Se-Se ₂	1.15	1.44	1.44
Te-Te ₂	1.30	1.67	2.15

TABLE 8

SCATHA PARTICLE DETECTOR ENERGY CHANNELS {Ref. 4}

Lo Detector

Step	Energy(eV)	Step	Energy(eV)
0	-0.334	32	26.26
1	-0.29	33	30.10
2	-0.23	34	34.57
3	-0.16	35	39.70
4	-0.08	36	45.55
5	0.00	37	52.22
6	0.09	38	60.00
7	0.22	39	68.77
8	0.34	40	78.55
9	0.50	41	90.10
10	0.67	42	103.32
11	0.87	43	118.32
12	1.10	44	135.65
13	1.36	45	155.43
14	1.66	46	178.09
15	2.00	47	203.98
16	2.39	48	233.42
17	2.83	49	267.20
18	3.34	50	306.30
19	3.94	51	350.74
20	4.60	52	401.96
21	5.37	53	457.73
22	6.25	54	525.50
23	7.25	55	601.05
24	8.40	56	687.71
25	9.72	57	787.70
26	11.23	58	902.13
27	12.96	59	1033.23
28	14.96	60	1184.33
29	17.23	61	1355.42
30	19.83	62	1529.85
31	22.80	63	1777.60

TABLE 8

CONTINUED

Hi Detector

Step	Energy (eV)	Step	Energy (eV)
0	-4.68	32	1205.49
1	-2.35	33	1383.30
2	0.32	34	1586.90
3	3.38	35	1820.02
4	6.88	36	2086.94
5	10.89	37	2392.57
6	15.49	38	2742.51
7	20.75	39	3143.19
8	26.77	40	3601.97
9	33.66	41	4127.28
10	41.56	42	4728.76
11	50.60	43	5417.45
12	60.95	44	6206.00
13	72.80	45	7108.89
14	86.37	46	8142.70
15	101.91	47	9326.41
16	119.71	48	10681.76
17	140.08	49	12233.63
18	163.41	50	14010.53
19	190.12	51	16045.08
20	220.70	52	18374.64
21	255.72	53	21041.98
22	295.81	54	24096.09
23	341.72	55	27593.05
24	394.29	56	31597.06
25	454.45	57	36181.66
26	523.39	58	41431.02
27	602.30	59	47441.54
28	692.65	60	54323.58
29	796.11	61	62203.53
30	914.56	62	71226.06
31	1050.19	63	81556.86

TABLE 9

THE SPUTTERING YIELDS OF 10 keV ION BEAMS ON
SILICON AND SILICON DIOXIDE {Ref. 36}

Target	Incident Ion Beam	
	Ar ⁺	O ₂ ⁺
Si	0.94	0.20
SiO ₂	0.69	0.48

TABLE 10

AMBIENT PLASMA VALUES FOR DAYS 83, 86, AND 200 OF 1979.
DATA FROM THE LOCKHEED ION MASS SPECTROMETER.

Day	Particle	Number Density (m^{-3})	Energy(keV)
83/ 1979	H ⁺	$3.845 * 10^3$	8.852
	H ₂ ⁺	$2.487 * 10^3$	120.778
	He	$2.865 * 10^3$	33.992
	O ⁺	$3.188 * 10^3$	4.217
86/ 1979	H ⁺	$2.606 * 10^3$	5.889
	H ₂ ⁺	$2.850 * 10^3$	43.728
	He	$2.410 * 10^3$	3.662
	O ⁺	$1.635 * 10^3$	4.035
200/ 1979	H ⁺	$9.064 * 10^3$	5.271
	H ₂ ⁺	$4.209 * 10^4$	7.279
	He	$2.169 * 10^3$	0.420
	O ⁺	$4.093 * 10^3$	1.957

LIST OF REFERENCES

1. DeForest, S.E., "Spacecraft Charging at Synchronous Orbit", Journal of Geophysical Research, V77, pp.651-659, 1972
2. Olsen, R.C., C. McIlwain, and E. Whipple, "Observations of Differential Charging Effects on ATS-6", Journal of Geophysical Research, V 86, 6809, 1981
3. DeForest, S.E., "Electrostatic Potentials Developed by ATS-5", Photon and Particle Interactions with Surfaces in Space, ed. R.J.L. Grard, pp. 263-276, D.Reidel, Dordrecht, Holland, 1973
4. DeForest, S. E., etal, Handbook for UCSD SC9 SCATHA Auroral Particles Experiment, University of California at San Diego, Revised Edition, 1980
5. Olsen, R.C., T. Aggson, and B. Ledley, "Observations of Electric Fields near the Plasmopause at Midnight", Journal of Geophysical Research, V 91, 12017, 1986
6. Tascione, T.F., Introduction to the Space Environment, Orbit Book Co., Malabar, FL, 1988, pp.33-57
7. Balsiger, H., "Composition of Hot Ions ($0.1-16\text{keV/e}$) as Observed by the GEOS and ISEE Mass Spectrometer and Inferences for the Origin and Circulation of Magnetospheric Plasmas", Advances in Space Research, V 1, 289, 1981
8. Balsiger, H., P. Eberhardt, J. Geiss, and D. Young, "Magnetic Storm Injection of 0.9 to 16 keV/e Solar and Terrestrial Ions into the High Altitude Magnetosphere", Journal of Geophysical Research, V85, 1645, 1980
9. Masek, T.D., and H. Cohen, "Satellite Positive-Ion-Beam System", Journal of Spacecraft, V 15, 27, 1978
10. Olsen, R.C., and E. Whipple, "An Unusual Charging Event on ISEE-1", unpublished paper, (Journal of Geophysical Research), submitted, 1987

11. Garrett, H.B., "Spacecraft Charging: A Review", Space Systems and Their Interactions with Earth's Space Environment, ed. H.B. Garrett and C.P. Pike, AIAA, New York, 1980
12. Grard, R, K. Knott, and A. Pederson, "Spacecraft Charging Effects", Space Science Reviews, V 34, 289, 1983
13. Whipple, E., "Potentials of Surfaces in Space", Reports on Progress in Physics, V 44, 1197, 1981
14. Li, W.W., and E. Whipple, "A Study of SCATHA Eclipse Charging", unpublished paper, (Journal of Geophysical Research), Submitted, 1987
15. Gussenhoven, M.S., and E.G. Mullen, "Geosynchronous Environment for Severe Spacecraft Charging", Journal of Spacecraft and Rockets, V 20, 26, 1983
16. Mullen, G., et al., "SCATHA Survey of High Level Spacecraft Charging in Sunlight", Journal of Geophysical Research, V 91, 1474, 1986
17. Koons, H.C., "Summary of Environmentally Induced Electrical Discharges on the P78-2(SCATHA) Satellite", Journal of Spacecraft, V 20, 425, 1983
18. Adamo, R.C., and J.R. Matarrese, "Transient Pulse Monitor Data from the P78-2(SCATHA) Spacecraft", Journal of Spacecraft, V 20, 432, 1983
19. Olsen, R.C., "Modification of Spacecraft Potentials by Thermal Electron Emission on ATS-5", Journal of Spacecraft and Rockets, V 18, 527, 1981
20. Olsen, R.C., "Modification of Spacecraft Potentials by Plasma Emission", Journal of Spacecraft and Rockets, V 18, 462, 1981
21. Townsend, P.D., J.C. Kelly, and N.E.W. Hartley, Ion Implantation, Sputtering, and their Applications, Academic Press, London, 1976, pp.111-145
22. McCracken, G.M., "The Behavior of Surfaces Under Ion Bombardment", Reports on Progress in Physics, V 38, 241, 1975
23. Winters, H.F., "Physical Sputtering", Radiation Effects on Solid Surfaces, ed. M.Kaminsky, American Chemical Society, Washington, D.C., 1976

24. Sigmund, P., "Theory of Sputtering.I.", Physical Review, V 184, No. 2, 383, 1969
25. Thompson, M.W., "II. The Energy Spectrum of Atoms during the High Energy Sputtering of Gold", Philosophical Magazine, V 18, 377, 1968
26. Lindhard, J., M. Scharff, and H.E. Schiott, "Range Concepts and Heavy Ion Ranges", Mat. Fys. Medd. Dan. Vid. Selsk., V 33, No. 14, 1963
27. Lindhard, J., V. Nielsen, and M. Scharff, "Approximation Method in Classical Scatterin By Screened Coulomb Fields", Mat. Fys. Medd. Dan. Vid. Selsk., V 36, No. 10, 1968
28. Garrison, B.J., et al., "Energy Cost to Sputter an Atom from a Surface in keV Ion Bombardment Processes", Surface Science Letters, V 180, L129, 1987
29. Interview between D.E. Harrison, Jr. Professor, Department of Physics, Naval Postgraduate School, Monterey, CA, and the author, January 1988
30. Matsunami, N., et al., Energy Dependence of the Yields of Ion-Induced Sputtering of Monatomic Solids, IPPJ-AM-32, Institute of Plasma Physics, Nagoya University, Chikusa-ku, Nagoya 464, Japan, September 1983
31. Anderson, H.H., and Bay, H.L., "Heavy-ion Sputtering Yields of Gold: Further Evidence of Non-Linear Effects", Journal of Applied Physics, V 46, 2416, 1975
32. Cauffman, D.P., Ionization and Attraction of Neutral Molecules to a Charged Spacecraft, AEROSPACE REPORT NO. TR-0074(9260-09)-1, AIR FORCE REPORT NO. SAMSO-TR-73-263, The Aerospace Corporation, 09 AUG 73
33. Scialdone, J.J., "An Estimate of the Outgassing of Space Payloads and Its Gaseous Influence on the Environment", Journal of Spacecraft, V 23, 373, 1986
34. Carre, D.J., and D.F. Hall, "Contamination Measurements During Operation of Hydrazine Thrusters on the P78-2 (SCATHA) Satellite", Journal of Spacecraft, V 20, 444, 1983

35. Werner, P.W., Ion Gun Operations at High Altitudes, M.S. Thesis, Naval Postgraduate School, Monterey, CA, June 1988
36. Okajima, Y., " Measurement of Sputtering Rate for 10 keV O_2^+ Ions with Ion Microanalyzer", Japanese Journal of Applied Physics, V 20, 2313, 1981
37. Weast, R.C., ed., CRC Handbook of Chemistry and Physics, 58th edition, CRC Press Inc., Cleveland, 1978

INITIAL DISTRIBUTION LIST

	No. Copies
1. Defense Technical Information Center Cameron Station Alexandria, VA 22304-6145	2
2. Library, Code 0142 Naval Postgraduate School Monterey, CA 93943-5002	2
3. Department Chairman, Code 61 Department of Physics Naval Postgraduate School Monterey, CA 93943-5000	2
4. Dr. R.C. Olsen, Code 610S Department of Physics Naval Postgraduate School Monterey, CA 93943-5000	20
5. Dr. S. Gnanalingam, Code 61GM Department of Physics Naval Postgraduate School Monterey, CA 93943-5000	1
6. Dr. J. Quinn Dept. 91-20, Bldg. 255 Lockheed Palo Alto Research Laboratories 3251 Hanover St. Palo Alto, CA 94304	1
7. Dr. Richard Johnson Packard Foundation 521 Hawthorne Ave. Los Altos, CA 94022	1
8. Mr. P. Klumpar Dept. 91-20, Bldg. 255 Lockheed Palo Alto Research Laboratories 3251 Hanover St. Palo Alto, CA 94304	1

- | | |
|---|---|
| 9. Dr. W. Peterson
Dept. 91-20, Bldg. 255
Lockheed Palo Alto Research Laboratories
3251 Hanover St.
Palo Alto, CA 94304 | 1 |
| 10. Mr. E. Shelley
Dept. 91-20, Bldg. 255
Lockheed Palo Alto Research Laboratories
3251 Hanover St.
Palo Alto, CA 94304 | 1 |
| 11. Ms. D.E. Donatelli
Space Physics Division
Air Force Geophysics Laboratory/PH
Hanscom AFB, MA 01731 | 1 |
| 12. Dr. R. Sagalyn
Space Physics Division
Air Force Geophysics Laboratory/PH
Hanscom AFB, MA 01731 | 1 |
| 13. Mr. G. Mullen
Space Physics Division
Air Force Geophysics Laboratory/PH
Hanscom AFB, MA 01731 | 1 |
| 14. Dr. S. Lai
Space Physics Division
Air Force Geophysics Laboratory/PH
Hanscom AFB, MA 01731 | 1 |
| 15. Dr. B. Burke
Space Physics Division
Air Force Geophysics Laboratory/PH
Hanscom AFB, MA 01731 | 1 |
| 16. Dr. N. Maynard
Space Physics Division
Air Force Geophysics Laboratory/PH
Hanscom AFB, MA 01731 | 1 |
| 17. Mr. R. Gracen Joiner
Office of Naval Research, Code 1114
800 North Quincy St.
Arlington, VA 22217-5000 | 1 |

18. Dr. H.C. Koons 3
Space Sciences Laboratory
The Aerospace Corporation, M2/260
P.O. Box 92957
Los Angeles, CA 90009
19. Dr. J. Roeder 2
Space Sciences Laboratory
The Aerospace Corporation, M2/260
P.O. Box 92957
Los Angeles, CA 90009
20. Dr. E.C. Whipple 1
Center for Astrophysics and Space Science
University of California at San Diego
La Jolla, CA 92093
21. Dr. C.E. McIlwain 1
Center for Astrophysics and Space Science
University of California at San Diego
La Jolla, CA 92093
22. Ms. W.W. Lei 1
Center for Astrophysics and Space Science
University of California at San Diego
La Jolla, CA 92093
23. Dr. S. Shawhan 1
NASA Headquarters/E
Washington, DC 20546
24. Dr. C.K. Purvis 1
MC 302-1
NASA Lewis Research Center
21000 Brookpark Rd.
Cleveland, OH 44135
25. Mr. M. Patterson 1
Low Thrust Propulsion Branch
NASA Lewis Research Center
21000 Brookpark Rd.
Cleveland, OH 44135
26. Mr. J. Kolecki 1
MC302-1
NASA Lewis Research Center
21000 Brookpark Rd.
Cleveland, OH 44135

27. Dr. C.R. Chappell 1
NASA Marshall Space Flight Center
Huntsville, AL 35812
28. Dr. T.E. Moore, ES53 1
NASA Marshall Space Flight Center
Huntsville, AL 35812
29. Dr. J.H. Waite 1
Southwest Research Institute
P.O. Drawer 28510
San Antonio, TX 78284
30. Capt. D. Allred 1
HQ, DNA/RAEV
6801 Telegraph Rd.
Alexandria, VA 22310
31. Dr. D. Hastings 1
Department of Aeronautics and Astronautics
Massachusetts Institute of Technology
Cambridge, MA 02139
32. Dr. I. Katz 1
S - Cubed
P.O. Box 1620
La Jolla, CA 92038-1620
33. Dr. M. Mandell 1
S - Cubed
P.O. Box 1620
La Jolla, CA 92038-1620
34. Dr. V. Davis 1
S - Cubed
P.O. Box 1620
La Jolla, CA 92038-1620
35. Dr. J. Raitt 1
CASS
Utah State University
Logan, UT 84322
36. Professor Nobuki Kawashima 1
Institute of Space and Astronautical Science
Komaba 4 - chome
Meguro - ku
Tokyo, Japan, 153

37. Professor W. Riedler 1
Institute für Weltraumforschung Oesterreichische
Akademieder Wissenschaften
Inffeldgasse 12
A - 8810 Graz, Austria
38. Dr. K. Torkar 1
Institute für Weltraumforschung Oesterreichische
Akademieder Wissenschaften
Inffeldgasse 12
A - 8810 Graz, Austria
39. Dr. R. Schmidt 1
Space Science Department
ESA/ESTEC
Noordwijk, The Netherlands
40. Dr. A. Pedersen 1
Space Science Department
ESA/ESTEC
Noordwijk, The Netherlands
41. Dr. W.F. Denig 1
Space Physics Division
Air Force Geophysics Laboratory/PHG
Hanscom AFB, MA 01731
42. Lt. C.W. Norwood 1
1524 St. James Pl.
Roslyn, PA 19001